

Smart release of corrosion inhibitors by a novel encapsulation method

MASTER OF SCIENCE THESIS

For the degree of Master of Science in Material Science and Engineering
at Delft University of Technology

Zhaoying Ding

July 11, 2016

Faculty of Mechanical, Maritime and Materials Engineering (3mE) · Delft University of
Technology



Copyright ©
All rights reserved.

Abstract

The objective of this project is to explore the feasibility of atomic layer deposition (ALD) and molecular layer deposition (MLD) as methods for the encapsulation of corrosion inhibitor. It is desirable to encapsulate the inhibitors before incorporation into the coating in order to provide a smart release only at specific conditions (acidic and alkaline pH in this case). ALD and MLD are processes to deposit conformal thin films with atomic and molecular level control, which leads to excellent step coverage and conformal deposition on complex micro- and nano-encapsulate structures.

In this project, ALD and MLD process in different conditions were applied to three environmentally friendly inhibitors, namely 2-mercaptobenzothiazole (2-MBT), $\text{Ce}(\text{NO}_3)_3$ and Li_2CO_3 , which present high protection performance against corrosion of aluminum alloys. After MLD and ALD, coverage of the coatings were characterized by scanning electron microscopy (SEM), coupled with energy dispersive x-ray spectroscopy (EDS) and Fourier transform infrared spectroscopy (FTIR). Leaching of coated inhibitors in solutions was studied by inductively coupled plasma-optical emission spectroscopy (ICP-OES) and ultraviolet-visible spectroscopy (UV-vis). Finally, the encapsulated inhibitors were incorporated into epoxy coating and applied on Al substrate. Inhibition efficiency was studied by electrochemical impedance spectroscopy (EIS). The results demonstrate that for the lithium carbonate, alumina shell can be formed in the surface via ALD process and a reduced leaching can be observed in the case of coated Li_2CO_3 ; healing effect can be observed in the encapsulated Li_2CO_3 doped coating, indicating the feasibility of this encapsulation concept on lithium carbonate. For the cerium nitrate, the inhibitor was coated with organic coating via MLD process but not well coated via ALD process; reduced leaching was not observed in this case and healing effect was not observed, neither. Organic shell can be well formed in the surface of 2-MBT, but the coating was not stable enough in solution to reduce leaching of the inhibitor; inhibition efficiency was not increased by doping the encapsulated 2-MBT into epoxy coating, possibly due to the reaction between shell material and epoxy coating.

Table of Contents

Acknowledgements	xi
1 Introduction	1
1-1 General metallic corrosion	1
1-2 Protection methods	1
1-3 Corrosion Inhibitors	2
1-3-1 Chromate inhibitor	3
1-3-2 Aluminium alloys and chromate free inhibitors	3
1-4 Self-healing anticorrosion coatings	6
1-4-1 Introduction of self-healing anticorrosion coatings	6
1-4-2 Controlled release of corrosion inhibitors	6
1-5 Strategies of controlled release of inhibitors from pretreatment or primer	8
1-5-1 Directly incorporation in the coating	8
1-5-2 Nano/micro-containers of corrosion inhibitors	9
1-5-3 Limitation of the current encapsulation method	14
1-6 ALD/MLD and Core-shell structures	15
1-6-1 Atomic layer deposition (ALD) and Molecular layer deposition (MLD)	15
1-6-2 Core-shell particles encapsulated by ALD and MLD	17
1-6-3 Advantages of ALD and MLD	20
2 Material and Methods	23
2-1 Inhibitors	23
2-2 Encapsulation methods	23
2-2-1 Pre-treatment of ALD and MLD	23
2-2-2 Molecular layer deposition (MLD)	24
2-2-3 Atomic layer deposition (ALD)	26
2-3 Characterization of the encapsulations	27

2-3-1	SEM and EDS	27
2-3-2	Fourier transform infrared spectroscopy (FTIR)	28
2-3-3	UV-vis spectra	28
2-3-4	ICP-OES	28
2-4	Characterization of the anticorrosion performance	29
2-5	Flow diagram of the experimented approach	30
3	Results and Discussion	31
3-1	Characterization of the encapsulation	31
3-1-1	Encapsulations of lithium carbonate	31
3-1-2	Encapsulations of cerium nitrate	43
3-1-3	Encapsulations of 2-mercaptobenzothiazole (2-MBT)	55
3-2	Characterization of the anti-corrosion performance	62
3-2-1	EIS results of encapsulated lithium carbonate doped coating	62
3-2-2	EIS results of encapsulated cerium nitrate doped coating	64
3-2-3	EIS results of encapsulated 2-MBT doped coating	65
3-3	Overall discussion	68
4	Conclusions and recommendations	71
4-1	Conclusions	71
4-2	Recommendations	73
A	ALD and MLD process	75
A-1	Appendix I: Mass spectrum in MLD process	75
A-2	Appendix II: Results of fluidization test	77
B	Database of EDS and ICP-OES	79
B-1	Appendix III: EDS data	79
B-2	Appendix IV: ICP-OES results	87
	Bibliography	89
	Glossary	95
	List of Acronyms	95

List of Figures

1-1	Illustration of the coating system in aerospace industry.	2
1-2	Tautomeric forms of 2-MBT.	4
1-3	TEM image of a hybrid sol-gel film containing zirconia-based nano-reservoirs[1]. .	10
1-4	Schematic view of particle with double-layered films on corrosion inhibitors[2]. . .	10
1-5	A) Schematic illustration of the procedure for benzotriazole loading for SiO ₂ nano-particulate containers, B) halloysite G nanotubes, and C) polyelectrolyte capsules[3].	12
1-6	Scheme of the controllable release of the inhibitor from the nano-containers and the 'smart self-healing' process[4].	13
1-7	Schematic representation of ALD using self-limiting surface chemistry and an AB binary reaction sequence[5].	15
1-8	Polymer film growth by MLD using PMDA and DDE[6].	16
1-9	TEM image of HCV grade BN coated with Al ₂ O ₃ ALD in a fluidized bed reactor[7].	17
1-10	TEM images of the alumina film on TiO ₂ nanoparticles for a dosing sequence of 3.5-10-2.5-10 min after (a) 4 ALD cycles; (b) 7 ALD cycles; and (c) 15 ALD cycles. (d) Distribution of the growth per cycle from the TEM pictures after 4 ALD cycles; (e) after 7 ALD cycles; and (f) after 15 ALD cycles. The mean growth per cycle and the standard deviation values are given in each histogram[8].	18
1-11	Thickness of the alumina film, determined from TEM images, for the different number of cycles for a dosing sequence of 3.5-10-2.5-10 min. The error bars represent the 10% error assumed in the image analysis[8].	18
1-12	Ellipsometry data for Al ₂ O ₃ ALD films grown using 300 reaction cycles on Si(100) substrates. The refractive index, growth rate, and density (calculated using ellipsometry and QCM data) are plotted versus growth temperatures from 33 to 177°C.[9].	19
1-13	An illustration of the reactions involved in the MLD process[10].	20
2-1	MLD setup used in the experiment.	24
2-2	An illustration of the reactions involved in the MLD process[10].	25
2-3	ALD setup used in the experiment.	26

2-4	Flow diagram of the experiment process.	30
3-1	SEM images of blank lithium carbonate after grinding in (a) x1000 and (b) x10000. 32	
3-2	(a) Backscattered electron image of blank lithium carbonate. (b) Image of blank lithium carbonate with EDS measurement points indicated.	33
3-3	Illustration of the reactions in (a) ALD and (b) MALD process[11] on lithium carbonate.	34
3-4	SEM images of lithium carbonate after 10 cycles' ALD coating in (a) x230 and (b) x5000.	35
3-5	EDS results of lithium carbonate particle after 10 cycles' ALD coating with (a) x2700 SEM-SEI image of a single particle used in the EDS measurement, (b) image with position of points measurements indicated, (c) oxygen elemental mapping and (d) aluminum elemental mapping.	36
3-6	FTIR spectrum of lithium carbonate after 4, 7 and 10 cycles' ALD coating and the blank lithium carbonate.	37
3-7	FTIR spectrum of lithium carbonate after 4, 7 and 10 cycles' MALD coating and the blank lithium carbonate.	37
3-8	Calculated thickness of alumina film on lithium carbonate with 4, 7 and 10 cycles' ALD coating and MALD coating, respectively.	39
3-9	Reactions in MALD process with TMA and ethanol as precursors.	39
3-10	(a) Backscattered electron image of the edge of cross sectional lithium carbonate ALD 10 sample. (b) Image of cross sectional lithium carbonate ALD 10 sample with EDS measurement points indicated.	40
3-11	ICP-OES results in the leaching test of coated lithium carbonate including samples with 4, 7 and 10 cycles' of ALD and MALD coating dissolving in HCl, water and NaOH solutions.	41
3-12	Second repetition ICP-OES results in the leaching test of ALD4, ALD10 and blank lithium carbonate dissolved in HCl, water and NaOH solution.	42
3-13	Pourbaix diagram of Al.	42
3-14	SEM images of blank cerium nitrate powder after grinding in magnifications of (a) x65 and (b) x300.	44
3-15	(a) Backscattered electron image of blank cerium nitrate. (b) Image of blank cerium nitrate with EDS measurement points indicated.	44
3-16	SEM images of cerium nitrate powder after 10 cycles' ALD process with (a) overview of the morphology, (b) comparison of the two morphologies of cerium nitrate after 10 cycles' ALD coating, (c) agglomeration of alumina in cerium nitrate with magnification of x500 and (d) agglomeration of alumina in cerium nitrate with magnification of x2000. magnification.	46
3-17	Image with EDS measurement points indicated correspond to (a) the single particles with smooth surface after ALD 10 coating (b) the agglomerations with rough surface after ALD 10 coating.	47
3-18	FTIR spectrum of cerium nitrate after 4, 7 and 10 cycles' of ALD coating.	49
3-19	Calculated thickness of alumina film on cerium nitrate with 4, 7 and 10 cycles' ALD coating and MALD coating, respectively. precursors.	50
3-20	Illustration of the expected reaction in MLD process on cerium nitrate.	50
3-21	SEM images of the morphology of cerium nitrate after 20 cycles' MLD coating in (a) x60 and (b) 200.	51

3-22	EDS point measurement on the spherical particles of $\text{Ce}(\text{NO}_3)_3$ after 20 cycles' MLD coating.	51
3-23	ICP-OES results in the leaching test of 4, 7 and 10 cycles' ALD, MALD and 5, 10 and 20 cycles' MLD coated cerium nitrate dissolved in HCl and neutral solution.	53
3-24	ICP-OES results in the leaching test of 4, 7 and 10 cycles' ALD, MALD and 5, 10 and 20 cycles' MLD coated cerium nitrate by redissolving the precipitate of $\text{Ce}(\text{OH})_3$	53
3-25	Second repetition ICP-OES result in the leaching test of ALD 4, ALD 10 and blank cerium nitrate samples.	54
3-26	SEM image of the precipitate in the $\text{Ce}(\text{NO}_3)_3$ ALD samples in neutral solution.	55
3-27	SEM images of the morphology of blank 2-MBT in (a) $\times 250$ and (b) $\times 2000$	56
3-28	EDS point measurements on the blank 2-MBT powder with position of the points indicated.	56
3-29	Illustration of the expected reactions in MLD process on 2-MBT.	57
3-30	SEM images of the morphology of 2-MBT after 20 cycles' MLD in (a) $\times 160$ and (b) $\times 950$	58
3-31	EDS point measurements on the MLD 20 2-MBT samples with position of the points indicated.	58
3-32	FTIR spectrum of blank 2-MBT.	59
3-33	FTIR spectrum of 2-MBT after 5, 10 and 20 cycle' MLD coating.	60
3-34	UV-vis absorption spectra of 2-MBT (a) in acid solution (b) in neutral solution and (c) in alkali solution.	61
3-35	Optical microscopy images of the scribed coating after 4 days' immersion in 0.05 M NaCl solution.	63
3-36	Bode plot from EIS measurement of the defect coated lithium carbonate system after (a) 3 hours (b) 1 day and (c) 4 days immersion.	63
3-37	Optical microscopy images of the scribed coating after 4 days' immersion in 0.05 M NaCl solution.	64
3-38	Bode plot from EIS measurement of the defect coated cerium nitrate system after (a) 3 hours (b) 1 day and (c) 4 days immersion.	65
3-39	Optical microscopy images of the scribed coating after 4 days' immersion in 0.05 M NaCl solution.	66
3-40	Bode plot from EIS measurement of the defect coated 2-MBT system after (a) 3 hours (b) 1 day and (c) 4 days immersion.	67
A-1	Mass spectrum during 20 cycles' MLD process on 2-MBT.	75
A-2	Mass spectrum of one of the half cycle during 20 cycles' MLD process on 2-MBT.	76
A-3	Results of fluidization test.	77
B-1	Image with measurement points indicated on blank lithium carbonate.	79
B-2	Image with measurement points indicated on ALD 10 lithium carbonate.	80
B-3	Image with measurement points indicated on ALD 10 lithium carbonate.	81
B-4	Image with measurement points indicated on MLD 20 cerium nitrate.	82
B-5	Image with measurement points indicated on MLD 20 cerium nitrate.	82
B-6	Image with measurement points indicated on MLD 20 cerium nitrate.	83

B-7	Image with measurement points indicated on ALD 10 cerium nitrate.	84
B-8	Image with measurement points indicated on ALD 10 cerium nitrate.	84
B-9	Image with measurement points indicated on blank 2-MBT without coating. . . .	85
B-10	Image with measurement points indicated on MLD 20 2-MBT.	86
B-11	Image with measurement points indicated on MLD 20 2-MBT.	86

List of Tables

2-1	List of the inhibitor encapsulated.	23
2-2	Composition of the epoxy.	29
3-1	Overview of the characterization of the encapsulation.	31
3-2	EDS elemental concentration measurements results of blank lithium carbonate correspond to points indicated in Figure3-2(b).	32
3-3	EDS elemental concentration measurements results of lithium carbonate after 10 cycles' ALD process correspond to points indicated in Figure3-5(b).	35
3-4	EDS elemental concentration measurements results of the cross sectional lithium carbonate ALD 10 samples from image in Figure3-10(b).	40
3-5	EDS elemental concentration measurements results of blank cerium nitrate correspond to the points indicated in Figure 3-15(b)	45
3-6	EDS elemental concentration measurements results correspond to the smooth surface ALD 10 particles with position of points indicated in Figure3-17(a)	47
3-7	EDS elemental concentration measurements results correspond to the rough surface ALD 10 particles with position of points indicated in Figure3-17(b)	48
3-8	EDS elemental concentration measurements results correspond to the position of points in the MLD 20 cerium nitrate spherical particles in Figure 3-22.	52
3-9	EDS elemental concentration measurements results correspond to the precipitate in the solution of $Ce(NO_3)_3$ ALD samples in neutral solution.	55
3-10	EDS elemental concentration measurements results of the blank 2-MBT powder correspond to the position of points indicated in Figure 3-28.	56
3-11	EDS elemental concentration measurements results of the 20 cycles' MLD 2-MBT correspond to the position of points indicated in Figure 3-31.	58
3-12	Absorptivity of 2-MBT in acidic and alkaline medium.	60
B-1	EDS elemental concentration measurements results of blank lithium carbonate.	80
B-2	EDS elemental concentration measurements results of lithium carbonate after 10 cycles' ALD correspond to the points in Figure B-2.	81
B-3	EDS elemental concentration measurements results of lithium carbonate after 10 cycles' ALD correspond to the points in Figure B-3	81

B-4	EDS elemental concentration measurements results of cerium nitrate after 20 cycles' MLD correspond to the points in Figure B-4	82
B-5	EDS elemental concentration measurements results of cerium nitrate after 20 cycles' MLD correspond to the points in Figure B-5	83
B-6	EDS elemental concentration measurements results of cerium nitrate after 20 cycles' MLD correspond to the points in Figure B-6	83
B-7	EDS elemental concentration measurements results of cerium nitrate after 10 cycles' ALD correspond to the points in Figure B-7	84
B-8	EDS elemental concentration measurements results of cerium nitrate after 10 cycles' ALD correspond to the points in Figure B-8	85
B-9	EDS elemental concentration measurements results of blank 2-MBT correspond to the points in Figure B-9	85
B-10	EDS elemental concentration measurements results of 2-MBT after 20 cycles' MLD correspond to the points in Figure B-10	86
B-11	EDS elemental concentration measurements results of 2-MBT after 20 cycles' MLD correspond to the points in Figure B-11	87
B-12	ICP-OES results and calculated thickness of alumina layer on lithium carbonate.	87
B-13	ICP-OES results and calculated thickness of alumina layer on cerium nitrate.	87

Acknowledgements

Doing a master thesis is the first to complete a scientific project independently, from which I have learned a lot including operation of all kinds of equipments, independent and critical thinking, communication skill, *etc.* This project would not have been finished without the help of many people. Here, I would like to express my heartfelt thanks for all your help and advice.

Foremost, I would like to express my sincere gratitude to my supervisors Dr. Yaiza Gonzalez-Garcia and Prof. Ruud van Ommen for providing me such an interesting topic as my graduation project. I would like to thank Yaiza for her continuous support, for her patience, motivation, enthusiasm, and immense knowledge. Her guidance helped me in all the time of research and writing this thesis. I would also like to thank Ruud for supervising me during this project and for the great and helpful discussions in the progress meetings. It was my honor to learn from them directly.

Besides my supervisor, I would like to thank the rest of my thesis committee members: Dr. Amarante Bottger and Mats Meeusen for their encouragement, insightful comments, hard questions and positive feedback. I would also like to thank Mats for guiding and helping me in the experiments and discussing the result with me.

I would also like to express my thanks to the people of the groups I had the pleasure to work in, namely Product and Process Engineering group of Chemical Engineering and Corrosion Technology and Electrochemistry group of Material Science and Engineering. I would like to thank Mojgan Talebi, Aris Goulas, Jauffrey Lescoffit, David Valdesueiro, Liang-Jun Yin, Abhay Dokania, Fabio Grillo for their help with atomic layer deposition. I would also like to thank Mats Meeusen, Majid Sababi, Umadevi Rathinavelu and Menno Sonnema for helping with the corrosion electrochemistry experiment. I would like to thank everyone who have give me help and support when I feel confused. It was a pleasure to work with you all!

Last but not the least, I would like to thank my family for supporting me spiritually throughout my life. In particular, I am grateful to my boyfriend for his patience and love.

Chapter 1

Introduction

1-1 General metallic corrosion

In our daily life, corrosion can be seen everywhere, such as the metals of our bikes, cars, the surface of our pans and pipeline, consequently damaging the material and structure. Corrosion is defined as the gradual damage of materials (usually metal) by reactions with their environment[12]. It is striking to realize that around 3.5% of the Gross National Product in the Netherlands, corresponding to 1100 euro per inhabitant per year is dedicated to corrosion problems. The amount of corrosion cost is still increasing autonomously for the process industry due to the trends of high process temperatures, aggressive chemicals and overdue maintenance, which will finally lead to the serious social problem such as plant downtime, loss of product, over-design, loss of efficiency. However, among the big cost of corrosion, 30% reduction is possible if all available knowledge and expertise is implemented.

There are mainly nine of forms of corrosion, including uniform corrosion, galvanic corrosion, crevice corrosion, pitting, hydrogen damage, intergranular corrosion, dealloying and erosion corrosion. The most common mechanism of corrosion may be the electrochemical oxidation of metals in reaction with an oxidant such as oxygen and water. This is an electrochemical process, or a chemical reaction, in which there is a transfer of electrons happening. However, the corrosion process is quite complicated due to the different properties of the material such as composition and microstructure.

1-2 Protection methods

As mentioned above, the huge economic impact of corrosion of metallic structures is a very important worldwide issue. Methods to prevent corrosion vary on the different type of corrosion. For galvanic corrosion, the best prevention is to eliminate the galvanic couple by selecting the right material. For pitting and crevice corrosion, decreasing either the aggressiveness of the environment or increasing the resistance of material is the best option. However, usually

the material and the environment condition cannot be easily changed. The application of coating is the most common and cost effective method of improving the corrosion resistance and consequently the durability of metallic structures. The main role of a coating in corrosion protection is to provide a barrier against corrosive species.

Generally, coatings for corrosion protection are applied as layered systems, where each layer has been optimized to maximize a different functionality (adhesion, corrosion protection, hydrophobicity, gloss, UV resistance). For example, an anticorrosive paint system in the aerospace industry has three main layers, as illustrated in Figure 1-1: a) a conversion coating (also called pre-treatment) of 100nm (*e.g.* chromate conversion coating) up to a few microns (*e.g.* anodizing layer) just above the metallic surface to offer good adhesion of the subsequent polymeric layer; it can also offer active corrosion protection, such as the case of sol-gel film containing corrosion inhibitors; b) a primer, which is normally an epoxy layer of around $20 - 25\mu\text{m}$ containing anticorrosion inhibitors to be leached out when damage takes place; and c) a topcoat, generally a polyurethane, which can have different thicknesses from $50 - 100\mu\text{m}$ and offer functional properties such as either colour, barrier hydrophobicity, gloss, or UV resistance[13].

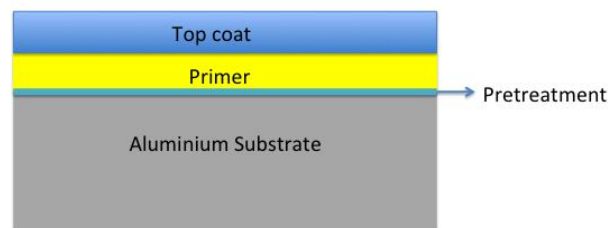


Figure 1-1: Illustration of the coating system in aerospace industry.

When defects appear in the protective coated structures, metallic surface would be exposure to the corrosive agents in the environment, and corrosion is initiated. It is in here when the corrosion inhibitors are released and acted against corrosion.

1-3 Corrosion Inhibitors

A corrosion inhibitor is a chemical compound that, when added to a liquid or gas, decreases the corrosion rate of a pure metal or an alloy[12]. A common mechanism for inhibiting corrosion involves formation of a coating, often a passivation layer, which prevents access of the corrosive substance to the metal.

Inhibitors are usually divided into three types, namely anodic inhibitors, cathodic inhibitors and mixed inhibitors[12]. Anodic inhibitors usually act by forming a protective oxide film on the surface of the metal causing a large anodic potential shift. This shift forces the metallic surface into the passivation region. They are also sometimes referred to as passivators.

Chromates, nitrates, tungstate, molybdates are some examples of anodic inhibitors. Cathodic inhibitors act by either slowing the cathodic reaction itself or selectively precipitating on cathodic areas to limit the diffusion of reducing species to the surface. The rates of the cathodic reactions can be reduced by the use of cathodic inhibitors. Mixed inhibitors work by reducing both the cathodic and anodic reactions. They are typically film-forming compounds that cause the formation of precipitates on the surface blocking both anodic and cathodic sites indirectly.

1-3-1 Chromate inhibitor

Historically, most of the inhibitor used in anti-corrosion coatings contains chromates. However, the outstanding corrosion protection provided by the leach ability and high oxidation potential of chromates is accompanied by environmental hazards and toxic risks. Inhalation, skin contact, and ingestion may allow chromates to enter the human body. The hexavalent chromium species can be responsible for DNA damage and cancer. In the Restriction of Hazardous Substance Directive (RoSH), the use of hexavalent chromium has been banned by the Europe government. The development of non-chromate environmentally friendly active corrosion protective system is, therefore, an issue of prime scientific and technological importance for various industries due to the significant gap between industrial needs and currently existing corrosion protection technologies.

1-3-2 Aluminium alloys and chromate free inhibitors

The main focus of the report would be given to the chromate free approach on the aluminium alloy. The AA2024 aluminium alloy is one of the most widely used materials in the aerospace industry due to its high strength to weight ratio. However the intermetallic particles (mainly Al_2CuMg and AlCuMn) [14], which confer superior strength to the alloy, also can form galvanic couples in contact with moisture promoting localized corrosion processes [15]. In this report, three chromate free inhibitors which show good corrosion inhibition for aluminium alloy are selected to be discussed as follow.

2-Mercaptobenzothiazole(2-MBT)

Various organic compounds with thiazole and triazole groups have been studied as corrosion inhibitors for copper and its alloy. Recently these compounds were also studied from the point of their inhibition effect for aluminium alloys and show promising results [16]. The introduction of the triazole or thiazole derivatives would lead to retardation of the corrosion processes by reducing the anodic reaction. 2-Mercaptobenzothiazole(2-MBT) has been found by research to be an effective inhibitor for long-term corrosion protection of AA2024 [17]. Zheludkevich *et al.* evaluated the performance of 1,2,4-triazole, 3-amino-1,2,4-triazole, benzotriazole and 2-mercaptobenzothiazole as corrosion inhibitors for protection of the 2024 aluminium alloy in neutral chloride solutions [15]. Conclusion was made that benzotriazole and 2-mercaptobenzothiazole offer better corrosion protection in comparison with the other two. 2-MBT exists in two tautomeric forms, namely thiol and thion form, shown in Figure 1-2. FTIR and Raman spectrum of 2-MBT has been reported by Rai *et al.* [18] and have shown

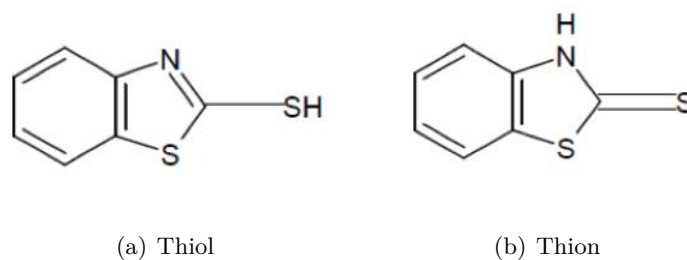


Figure 1-2: Tautomeric forms of 2-MBT.

that the thion form of 2-MBT is more stable than thiol form and dimeric conformation is more stable than monomeric conformation. Research shows that when localized corrosion occurs, 2-MBT forms Cu(I) surface films of stoichiometries Cu(MBT) on the alloy surface that confers a good corrosion protection[19]. The formation of a polymeric layer by oxidized form of 2-MBT and copper ions in the position of copper-rich intermetallics inhibits the anodic dissolution of copper, thus decreasing the anodic activity. The formation of the surface film is caused by the stable covalent Cu-S bonds[20].

Cerium nitrate

Rare earth salts are prospective candidates for inhibiting the corrosion of many metals and alloys. They demonstrate very efficient inhibitive properties, especially for aluminium alloys. They are often thought of as environmentally friendly substitute for toxic yet powerful chromate-based inhibitors. Many studies suggest that the incorporation of RE ions into sol-gel coatings offers an improvement in active corrosion protection properties. Palanivel *et al.* demonstrated the positive effects of cerium nitrate incorporation into silane films based on bis-(3-triethoxysilylpropyl)tetrasulfide, bis-(trimethoxysilylpropyl)amine and vinyltriacetoxysilane[21]. DC polarization tests demonstrated that coatings containing from 100 to 2000 ppm of cerium nitrate show enhanced corrosion protection. The tests of both undamaged and damaged specimens have also been done. A pre-scratched coated sample was held in a cell filled with corrosive electrolyte. The studied coating was around 300 nm thick and was based on a combination of bis-silanes, as described above, and contained 1000 ppm of cerium nitrate inhibitor. Several scratches having width around 100 μm were made on the coated samples. Blank AA2024 substrates were held in the electrolyte close to the scratched silane film. In such arrangement, the blank sample can be protected by the leaching inhibiting species of cerium from the damaged coating. DC polarization tests were made on the blank substrates after different testing times demonstrated a decrease of corrosion current (i_{corr}) with immersion time. This inhibiting effect was attributed to the leaching of cerium ions from the scratched area and precipitation on the blank substrates during immersion. The improvement of anticorrosion performance of Ce is based on the inhibiting effect of cerium ions in cathodic oxygen reduction processes[22]. Insoluble cerium hydroxides precipitate in the places where pH is increased as a result of cathodic activity, thus hindering the cathodic process.

Machkova *et al.* also studied the effect of the anionic part of various Ce(III) salts on the corrosion inhibition efficiency of AA2024 aluminium alloy[23]. Systematic comparative investigations, evaluating the inhibitive ability of various cerium salts in their third oxidation

state (CeCl_3 , $\text{Ce}_2(\text{SO}_4)_3$, $\text{Ce}(\text{NO}_3)_3$ and $(\text{NH}_4)_2\text{Ce}(\text{NO}_3)_5$) against the corrosion of AA2024 aluminium alloy in 0.01 M NaCl solution, has been done. In respect to the inhibitive efficiency against AA2024 corrosion, the line of the Ce(III) salts studied was given according to the variation of the impedance parameters during the entire exposure of the samples to the corrosive media (immersion in 0.01 M NaCl solution from 24 to 600 h): $\text{Ce}_2(\text{SO}_4)_3 > (\text{NH}_4)_2\text{Ce}(\text{NO}_3)_5 > \text{Ce}_2(\text{SO}_4)_3 > \text{CeCl}_3$ [23].

Lithium carbonate

Various lithium salts have also been studied as potential replacement for the chromate-containing pigments in organic coatings recently[24]. In 1993, Buchheit *et al.* proposed a new talc coating by immersion in an alkaline Li salt bath followed by a low-temperature (<100 °C.) heat treatment in air or water, and the result shows that the barrier properties was compared favorably with those of traditional inorganic corrosion-resistant coatings produced by chromate conversion[25]. The mechanism behind is given as a formation of barrier film as a continuous polycrystalline coating on Al surfaces by precipitation from alkaline solutions. It was found that lithium cations can be intercalated into aluminium hydroxide to form insoluble layered double hydroxides[26]. The protective properties provided by these lithium conversion layers are thought to originate from the formation of a lithium-aluminum hydroxide-carbonatehydrate layer with a stoichiometry as $(\text{Li}_2[\text{Al}_2(\text{OH})_6]_2 \cdot \text{CO}_3 \cdot n\text{H}_2\text{O})$, which greatly increases the corrosion resistance of various substrates, by increasing the pitting potential and reducing the corrosion current density[25]. The incorporation of lithium salts as leachable inhibitor in organic coating was proposed by Peter Visser *et al.* for the protection of aluminium alloys[27][28]. Lithium carbonate and lithium oxalate were incorporated as leachable corrosion inhibitors in model organic coatings for the protection of AA2024-T3 and the coated samples were artificially damaged with a scribe[28]. It was found that the lithium-salts are able to leach from the organic coating and form a protective layer in the scribe on AA2024-T3 under neutral salt spray conditions. Yanwen Liu *et al.* investigated the films formed in the damaged area of AA2024 aluminium alloy coated with a lithium carbonated pigmented coatings as well. It was found that films with varied morphologies in different locations were formed and protected the alloy effectively from corrosion[26].

1-4 Self-healing anticorrosion coatings

1-4-1 Introduction of self-healing anticorrosion coatings

As mentioned above, the application of coating is the most common and effective corrosion protection method. However, it is very common that coating systems present defects due to mechanical or chemical damage, or even the failures during its application, which allows direct access of corrosive agents to the metallic surface. The corrosion processes develop faster after disruption of the protective barrier. This has led the search for paint systems that can be more efficient, ensuring the protection of the substrate. Therefore, active 'self-healing' of defects in coating is necessary to provide long-term protection.

The term self-healing in materials science means self-recovery of the initial properties of the material following damage caused by the external environment or internal stresses[29]. The same definition is also applicable to functional coatings. A partial recovery of the main functionality of the material can also be considered as a self-healing ability. For the anticorrosion coating system, the hindering of corrosion activity at a defect by the coating itself, is enough to constitute self-healing.

The approach to self healing corrosion protective can be divided into two categories, namely extrinsic and intrinsic healing approaches: the extrinsic approach involves incorporation of healing agents such as binding agents and corrosion inhibitors into the coating system to enable surface protection against the corrosion activity; the intrinsic approach involves introduction of reversible chemistries that enable damage closure and sealing[30]. The strategy of incorporation of healing agents, which can improve the protective properties of the coating has been studied extensively as a promising way to achieve the self-healing anticorrosion coating.

Garcia *et al.* summarize five characteristics of healing materials used in organic coatings: self-healing in engineering material a) requires a mobile phase material stored in containers or intrinsically incorporated into the coating matrix, able to fulfill the healing process. The healing agent should only be mobile where damage occurs and when needed: local temporary release of the healing agent; b) may require externally supplied healing agents (such as moisture or oxygen) in case the restoration of the damage site requires the supply of new material to fill the initially empty damage volume; c) may require a period of reduced loading conditions (the recovery period) to allow healing to take place; d) may require the supply of a modest amount of externally applied energy (e.g. local temperature, UV, high kinetic energy in high speed impacts) to increase the local mobility involved in healing and to minimize the recovery period to acceptable time scales; e) may require detection systems to determine the occurrence of damage and activation systems to trigger the healing[13]. Doping the corrosion inhibitors into the coating is one of the most important way to achieve self-healing anticorrosion coating.

1-4-2 Controlled release of corrosion inhibitors

When corrosion activity is happening in the scratched or defect region of the coating, the inhibitors incorporated into the coating can be released triggered by the change of the environment such as pH and concentration of Cl^- . The controlled leaching of the inhibitor to the

damaged sites can passivate the underlying substrate or seal it from the surrounding corrosive media through chemical or physical interactions, fulfilling the self-healing process of the coating.

One of the first examples of a pH-controlled release of corrosion-inhibiting ions from an amorphous metallic coating where the pH change which results from the onset of corrosion was investigated by Jakab *et al.*[31][32]. In their study, a new amorphous Al-Co-Ce alloy coating was synthesised and applied on the aluminium surface. At first, such metallic coatings can be effective by providing sacrificial anode-based cathodic protection. But the fact that the coating contains cerium and cobalt makes it also able to generate corrosion inhibiting species. The Co^{2+} and Ce^{3+} cations are released during anodic dissolution of the metallic coating. Dissolved cerium and cobalt cations can diffuse to the metallic substrate surface and form insoluble hydroxide precipitates covering the cathodic zones on the aluminium alloy[31].

Moreover, the release of inhibitors can also be triggered by a redox process[33]. Galvanic reduction of 2,5-dimercapto-1,3,4-thiadiazole polymer in a conducting carbon paste releases its monomer anion. The monomer anion, in turn, exhibits very good inhibition efficiency for the cathodic oxygen reduction process. This chemistry forms the basis for a ‘smart’ self-healing material that releases an inhibitor when the material is coupled to a base metal, as in the case of a coating with a defect. No release would occur in the absence of the defect due to the lack of the reducing force of the base metal.

1-5 Strategies of controlled release of inhibitors from pretreatment or primer

Corrosion inhibitors can either be added directly to the coating formulation or immobilized/encapsulated in carriers to reduce possible interactions with the matrix and to control release of the inhibitor. The strategies of controlled release of inhibitor from primer or pre-treat layer of the coating are addressed in the following parts.

1-5-1 Directly incorporation in the coating

The easiest way to introduce a corrosion inhibitor is simply to dissolve it into the coating formulation. It has been investigated by Mascia *et al.*[34] that the improvement of corrosion protection could be achieved by doping of molybdate anions within the siloxane network of epoxy-silica hybrids, especially when the molybdate ions were added in a 'bound' form as an amine salt obtained from the reaction of the amine hardener and molybdic acid.

Khramov *et al.* have also done the research on the corrosion protection properties of hybrid films with incorporated 2-mercaptobenzothiazole and 2-mercaptobenzimidazole as corrosion inhibitors[16]. The SNAP (Self-assembled Nano-phase Particle) sol-gel coatings are well suited to incorporate organic inhibitors. Inhibitor loaded SNAP films were evaluated by current density distribution maps for Al/Cu artificial defects on AA2024. The current peak after immersion for 3 hours in NaCl solution was almost 25 times smaller in the case of the inhibited SNAP coating, showing the inhibition of the corrosion process by the mercaptobenzimidazole molecules.

However, the direct addition of a corrosion inhibitor to the coating may raise many problems. Firstly, the inhibiting species are effective only if their solubility in the corrosive environment is in the right range. A very low solubility would lead to a lack of active agent at the defect site and, consequently, to a weak self-healing ability; a very high solubility would make the inhibitor be leached out from coating rapidly and the protection would only last for a relatively short time. Secondly, the high solubility would also lead to blistering and delamination of the protective of coating due to the osmotic pressure which forces water permeation. Thirdly, the barrier properties of the coating might be weakened if the corrosion inhibitor interacts chemically with the components of the coating.

Take the rare earth inhibitor of cerium nitrate as an example: even though the presence of cerium in sol-gel coating may improve the corrosion protection performance of the sol-gel coating, the high concentration of cerium salts can significantly destabilize a sol-gel matrix because of the formation of interfaces, which can retain water[35]. The direct addition of RE salts can negatively influence the adhesion and the barrier properties of coating, and can chemically modify the sol-gel matrix and affect polymerization of the sol-gel system. An addition problem is that soluble RE salts are prone to fast release from the sol-gel coatings, thus reducing their effectiveness in corrosion protection.

Therefore, a direct dissolution of an inhibitor in the formulations of organic coating is not used in practice. Strategies of encapsulation should be taken into consideration.

1-5-2 Nano/micro-containers of corrosion inhibitors

Recent developments in surface science and technology have introduced new ways for the fabrication of self-healing coating through the integration of nano-scale containers (carriers) loaded with active inhibiting compounds within existing conventional coatings. This approach leads to a new coating systems based on 'passive' host-'active' guest structures. As a result, nano-containers are uniformly distributed in the passive matrix, keeping the active species in a 'trapped' state. This would, to a great extent, reduce the possibility of excessive inhibitor leaching and pigment induced osmotic blistering that may occur if the inhibitor salts are doped directly in to the coating. When corrosion starts at a coating defect, the local environmental changes would lead the nano-containers respond to this signal and release the immobilized active material[36][37].

The nano-containers can be classified by two ways, namely: immobilization via the inhibitor carriers and encapsulation with different types of shells. In the following part, the main approaches of inhibitor immobilization and encapsulation will be introduced in terms of their applicability on self-healing anticorrosion coatings.

Immobilisation

A simple approach to inhibitor entrapment is based on the complexation of organic molecules by cyclodextrin[16][38]. Cyclodextrins are known as complexation agents that play the role of hosts, forming inclusion complexes with various organic guest molecules that fit within the cyclodextrin cavities. Organic aromatic and heterocyclic compounds are usually the main candidates for the inclusion complexation reaction[39]. Several organic heterocyclic compounds are known inhibitors for various metallic substrates. Cyclodextrins can be effectively used for immobilisation of these species. In the research, which focused on the self-healing effect of the immobilised inhibitor by cyclodextrin[16], two organic corrosion inhibitors, 2-mercaptobenzothiazole (MBT) and 2-mercaptobenzimidazole (MBI), were added to a hybrid sol-gel used for corrosion protection of AA2024 aluminium alloy. MBT and MBI were introduced in the sol-gel formulations as inclusion host/guest complexes with β -cyclodextrin. The hybrid films doped with corrosion inhibitors provided superior corrosion protection when compared to the un-doped ones.

Another entrapment concept is based on the use of oxide nanoparticles, which play the role of nanocarriers of corrosion inhibitors adsorbed on their surface. The oxide nanoparticles by themselves are known reinforcements for the coating formulations, as their addition leads to the enhanced barrier properties. Moreover, additional active corrosion protection and a self-healing ability can be achieved when the oxide nanoparticles are doped with a corrosion inhibitor. For example, Ce^{4+} ions can be loaded on the surface of the zirconia nanoparticles during the synthesis of the sol by controlled hydrolysis of the precursors by a Ce^{4+} containing aqueous solution[1]. The resulting sol mixed with hybrid sol-gel formulation leads to nanocomposite hybrid coatings containing oxide nanocontainers of cerium ions. The high total surface area of the carriers, resulting from the small diameter of the nanoparticles ($\sim 4nm$ as shown in Figure 1-3), provides sufficient loading capacity for the inhibitor. The prolonged release of inhibitor from the surface of oxide nanoparticles permits the enhanced longterm corrosion protection of AA2024 aluminium alloy compared to the case where the inhibitor is directly added to the sol-gel matrix.

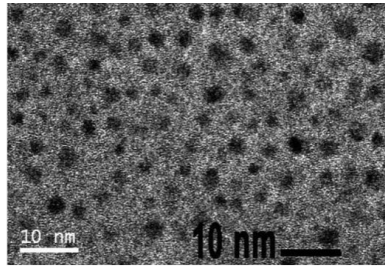


Figure 1-3: TEM image of a hybrid sol-gel film containing zirconia-based nano-reservoirs[1].

There are many ways to use the nanoparticle surface as an inhibitor carrier. For example, organic and inorganic inhibitors can be loaded by porous filling on hollow cellular structure[40]; inorganic inhibiting anions can be adsorbed onto the particle surface by ion-exchange mechanism[41]; inhibiting inorganic cations can also be incorporated as exchangeable ions associated with cation-exchange solids or anion-exchange pigments[42]. Different immobilizations have their own advantage and disadvantage: a higher loading capacity can be achieved by the hollow cellular structure; osmotic blistering can be avoided by the cation exchange pigment strategy; the harmful chlorides can be absorbed by anion exchange pigment, which is the special case that the release of inhibitor can be provoked by the aggressive corrosion chloride ions.

Encapsulation

There are also a lot of encapsulation techniques, in which a protective shell is always created around a core containing inhibitor.

One of the encapsulation way is encapsulating the inhibitor with a polymerisable healing agent. Yang and van Ooij encapsulated triazole inhibitor using plasma polymerisation to produce plasma-polymerized perfluorohexane and plasma-polymerized pyrrole layers employing RF plasma discharge[43]. Figure 1-4 shows a schematic view of the inhibitor with double-layered films. The plasma-treated triazole was used as a pigment in a water-based epoxy coating, slowly releasing the inhibitor and providing long-term corrosion protection. In both cases, the release of the inhibitor from the capsule is possible only when it is mechanically damaged. The damaged capsule releases the entire active agent very quickly in a non-controllable way.

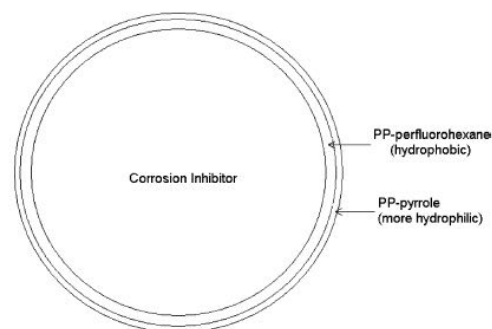


Figure 1-4: Schematic view of particle with double-layered films on corrosion inhibitors[2].

Kumar *et al.* investigated the efficacy of a self-healing corrosion protection coating system with urea formaldehyde microcapsules (50-150 μm in diameter) containing several types of film forming compounds (healants) and corrosion inhibitors mixed into commercially available organic coatings[44]. It has been shown that the core constituents of self-healing microcapsules are released when the microcapsules are ruptured by damage to the coating in which they were contained, whether from natural cracks resulting from aging or from mechanical damage to the coating. Steel substrates coated with these self-healing systems were scribed and laboratory tested according to accelerated corrosion testing based on ASTM D 5894. Undercutting at the scribe (ASTM D 1654) was reduced because of the using microcapsules containing self-healing compounds. Growth of coating damage at the scribe was arrested in self-healing coatings with all microcapsule formulations compared to control samples.

A very interesting alternative, which allows controllable leaching, triggered by corrosion related stimuli is the use of Layer-by-Layer (LbL) assembled shells. Nanocontainers with regulated storage and release of the inhibitor can be constructed with nanometer-scale precision employing the layer-by-layer deposition approach[2]. The LBL shells have two main advantages: it isolates the inhibitor, avoiding its negative effect on the integrity of the coating, and provides a smart release of the corrosion inhibitor by changing the local pH and humidity.

Shchukin and Möhwald did research on three methods of encapsulation, and two of them were based on LbL assembled nanocontainers, which were perspective in the application of self-healing anticorrosion coatings[3]. The release properties and reloading ability of polyelectrolyte-modified halloysite nanotubes, polyelectrolyte-modified SiO_2 nanoparticles, and polyelectrolyte capsules were studied. SiO_2 and halloysite G nanoparticles were chosen as nanocontainers for benzotriazole (inhibitor) because they could be easily incorporated into the silica-based sol-gel coating, which was used for aluminum protection, preserving its structure. The initial SiO_2 nanoparticles were negatively charged. Therefore, the deposition of the positive poly (ethylene imine) (PEI) was performed, in the first stage. Then, the deposition of the negative poly (styrene sulphonate) (PSS) layer was carried out. Deposition of the third inhibitor layer was accomplished in acidic media (pH3) from a 10 mg/ml solution of benzotriazole. The latter two deposition steps (PSS and benzotriazole) were repeated once to ensure a high inhibitor loading in the final LbL structure. Two PSS/benzotriazole bilayers have been identified to be the ideal number of deposited layers on the silica nanoparticles[4]. One bilayer is not sufficient for the self-healing effect of the final protective coating while three or more bilayers drastically increase aggregation of the nano-containers during assembly and coating deposition. The benzotriazole content in nano-containers is equal to 95 mg per 1 g of the initial SiO_2 particles. The assembly process of such nanocontainers with incorporated corrosion inhibitors is schematically depicted in Figure 1-5A[3].

Halloysite is an economically viable raw material that can be mined from the corresponding deposit as a raw mineral. As for most natural materials, the size of halloysite particle varies within 1-15 μm of length and 10-100 nm of inner diameter depending on the deposits. The strong surface charge on the halloysite tubules has been exploited for designing nano-organized multilayers using the layer-by-layer method[45]. To attain controlled release properties in the halloysite nanotubes, after benzotriazole embedded into the nanotubes, the surface of the nanotubes should be modified by LbL deposition of four polyelectrolyte bilayers. This is because the benzotriazole molecules have good solubility in water, and therefore, pure benzotriazole-filled halloysite cannot be directly applied in self-healing anticorrosion coatings because of the possible spontaneous leakage and uncontrolled release of the embedded benzotriazole. The

assembly process is schematically shown in Figure 1-5B[3].

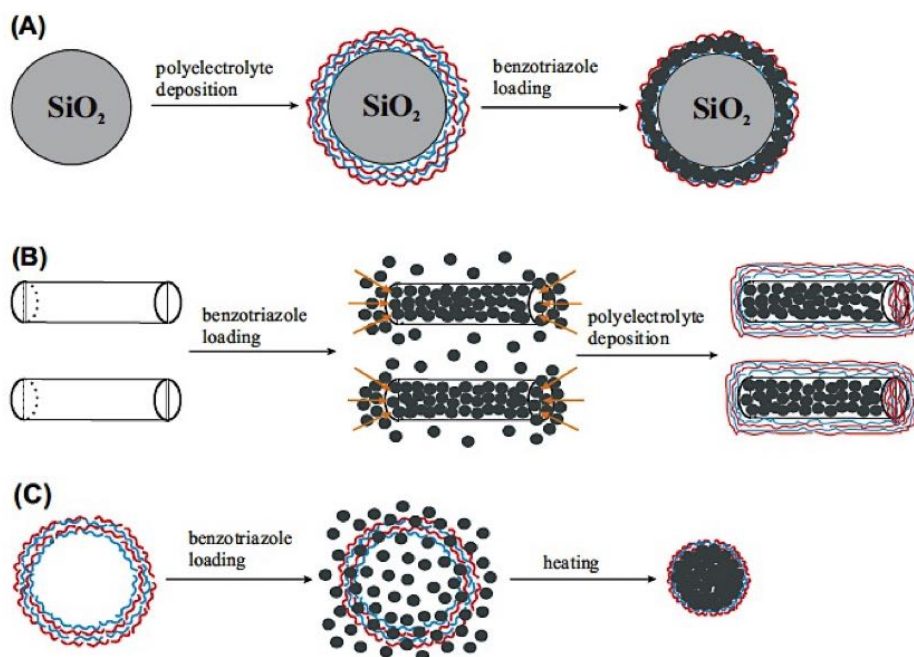


Figure 1-5: A) Schematic illustration of the procedure for benzotriazole loading for SiO₂ nanoparticulate containers, B) halloysite G nanotubes, and C) polyelectrolyte capsules[3].

Micrometer-scale polyelectrolyte capsules of different shell composition were employed as the third type of benzotriazole loaded containers. Benzotriazole was trapped in polyelectrolyte capsules by the thermal-encapsulation method, which would not be introduced here in detail. The main process is shown schematically in Figure 1-5C.

The release characteristics, as well as the reload ability characteristics, of all three nanocontainers with encapsulated benzotriazole were studied in aqueous solutions at acidic, neutral, and alkaline pH, which was adjusted by adding HCl or NaOH. The results showed that all nanocontainers reveal an increase of the benzotriazole release in aqueous solution at alkaline or acidic pH. The highest reloading efficiency (up to 80%) is observed for halloysite-based nanocontainers; however, after five reloading cycles the efficiency decreases to 20%. The application of appropriate nanocontainers depends on the demands required from feedback-active anticorrosion coatings. For coatings where the immediate release of the inhibitor is necessary, SiO₂-based or halloysite-based nanocontainers with a shell consisting of weak polyelectrolytes are preferable. When continuous, gradual release is required, halloysite-based nanocontainers with a shell consisting of one weak and one or two strong polyelectrolytes are preferable[3].

One year later, Zheludkevich *et al.* investigated a smart self-healing anticorrosion coating based on the SiO₂ nanocontainers system in which silica nanoparticles were used as a template and benzotriazole as an organic corrosion inhibitor, which is mentioned above[4]. The sol of nanocontainers containing benzotriazole was mixed with a hybrid sol-gel formulation and then applied on the surface of AA2024 aluminium alloy[4]. The samples coated with the hybrid film doped with LbL nanocontainers demonstrated significantly enhanced performance

in corrosion tests in comparison to an undoped sol-gel film or a film doped directly with free non-immobilized benzotriazole. After 2 weeks of immersion in a chloride solution, the nano-reservoir-containing film was still intact, while the sample coated with hybrid coating directly doped with benzotriazole showed extensive corrosion attack with many pits on the alloy surface. Scanning vibrating electrode technique (SVET) experiments were also performed. From the current map a 'smart' self-healing effect can be observed from active feedback between the coating and the localized corrosion processes.

The most probable mechanism of the smart release effect of LbL assembled shell is based on the local change of pH in the damaged area due to the corrosion processes. When the corrosion process is started, the pH value changes in the neighboring area, which increases the permeability of the polyelectrolyte shells of the nano-containers in a local area with the consequent release of benzotriazole. Then, the released inhibitor suppresses the corrosion activity and the pH value recovers, closing the polyelectrolyte shell of nano-containers and terminating further release of the inhibitor, as shown schematically in Figure 1-6[4].

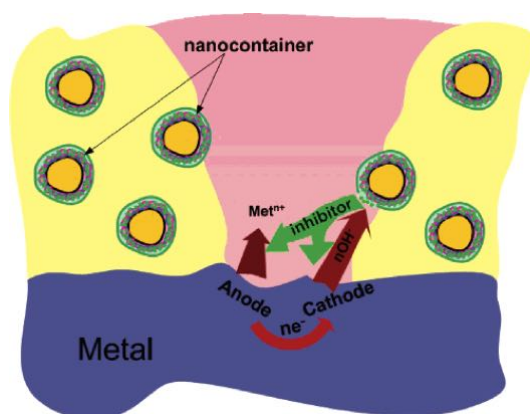


Figure 1-6: Scheme of the controllable release of the inhibitor from the nano-containers and the 'smart self-healing' process[4].

The promising results obtained on the LbL nanocontainers described above show the principal main opportunity of using this approach for intelligent self-healing coatings. However, nanocontainers with silica cores do not provide high inhibitor loading capacity. Porous cores are more promising. One of the prospective future containers may be industrially mined halloysite nanotubes as mentioned above. Shchukin *et al.* investigated an active anticorrosion coatings with halloysite nanocontainers, which are nanotubes with inner voids loaded by inhibitors (2-mercaptobenzothiazole) and outer surfaces later-by-later covered with polyelectrolyte multilayers to prevent the spontaneous leakage[46]. This nanocontainers showed very good upkeep characteristics: almost complete suppression of inhibitor release, with more than 90% of the initial loading retained inside the inner cavity. This can be explained by the geometrical restriction of the nanotubular container, which is able to release the encapsulated material only through the polyelectrolyte-blocked edges with diameters of 20-50 nm. AA2024-T3 aluminium alloy was taken as a model metal substrate. The results of long-term corrosion tests demonstrated the superior corrosion protection performance of halloysite-doped hybrid sol-gel films compared to that of undoped coatings[46].

1-5-3 Limitation of the current encapsulation method

The main encapsulation methods currently used have been introduced above. As mentioned, the interaction between the inhibitors and coating would rise the risk of weakening the adhesion and barrier properties of coating. Encapsulation method achieved by LbL assembled shells seems to be superior to the other methods since the shell isolates the inhibitor, avoiding its negative effect on the integrity of coating and providing a smart release of inhibitor triggered by local pH changing. However, the efficiency of LbL assembled shells heavily relies on the nanocontainer. To find a suitable container for the inhibitor seems to be an issue. Some of the nanocontainers, like silica cores, do not provide high inhibitor loading capacity. The size inhibitors to be loaded into the nanocontainer like halloysite nanotubes have to be controlled precisely in a right range to be embedded into the nanotube.

Therefore, a more straight forward encapsulation method like growing a stable thin layer of shell material in the inhibitor, which would neither chemically react with the coating nor increase the size of inhibitor a lot, would be a promising strategy in developing self-healing anticorrosion coatings.

1-6 ALD/MLD and Core-shell structures

1-6-1 Atomic layer deposition (ALD) and Molecular layer deposition (MLD)

Atomic layer deposition (ALD)

Atomic layer deposition (ALD) is a self-limiting technique for growing thin films that is characterized by alternately exposing the sample surface to gas-phase chemical precursors[47]. The ALD process is self-limiting because the surface reactions will automatically cease when the accessible reactive surface groups have all been removed. This self-limiting nature of the separate surface reactions has as a consequence that the same amount of material is deposited each ALD cycle and thus makes it possible to accurately control the film growth up to the atomic scale[48]. One ALD cycle consists typically of four steps, as schematically illustrated in Figure 1-7: first gas-solid reaction, *i.e.*, chemisorption reaction of the first reactant (Reactant A), typically of a metal reactant (Step 1); purge or evacuation to remove the unreacted precursor and gaseous by-products (Step 2); second gas-solid reaction, *i.e.* chemisorption reaction of the second reactant (Reactant B), typically of a non-metal reactant (Step 3); and again purge or evacuation to remove the unreacted precursor and gaseous by-products (Step 4)[5]. Most ALD processes are based on binary reaction sequences where two surface reactions occur and deposit a binary compound film. Because there are only a finite number of surface sites, the reactions can only deposit a finite number of surface species. If each of the two surface reactions is self-limiting, then the two reactions may proceed in a sequential fashion to deposit a thin film with atomic level control[48].

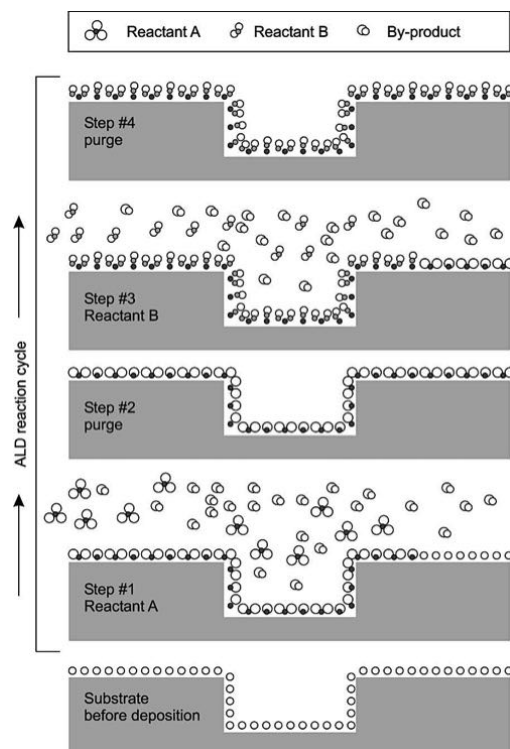


Figure 1-7: Schematic representation of ALD using self-limiting surface chemistry and an AB binary reaction sequence[5].

ALD technique has mainly three advantages: 1) it guarantees efficient use of the precursor and this point is especially true when carried out on particles, less for flat substrates (typically more bypass in the latter case); 2) it allows precise control of the size loading; 3) it can be used for low and medium loading of catalysts by high quality (low impurities level) end products[7]. ALD is only limited by the size of the reaction chamber and dominated by surface reactions. Because the surface reactions are performed sequentially, the two gaseous reactants are not in contact in the gas phase. This separation of the two reactions limits possible gas phase reactions that can form particles that could deposit on the surface to produce granular films, like can happen in chemical vapor deposition.

Molecular layer deposition (MLD)

Molecular layer deposition (MLD) is also a thin-film growth technique, by which precise and well-controlled coating can be achieved. The basic mechanism of MLD is similar to ALD. In a typical MLD process, molecular fragments of the bi-functional precursors are deposited on the surface of an active substrate. This process involves two alternating reactions. Figure 1-8 shows an example of MLD[6]: pyromellitic dianhydride (PMDA) is used as molecule A and 4,4'-diaminodiphenyl ether (DDE) as molecule B. Monomolecular layer growth is observed at the same temperature for both DDE on PMDA and PMDA on DDE. Therefore, MLD can be done without elevating substrate temperature. A 100Å thick polymer film was deposited by MLD within 15 cycles of alternate molecule supply. It is the self-limiting nature of these reactions which enables the deposition of ultra thin layers on the surface of the substrate[10].

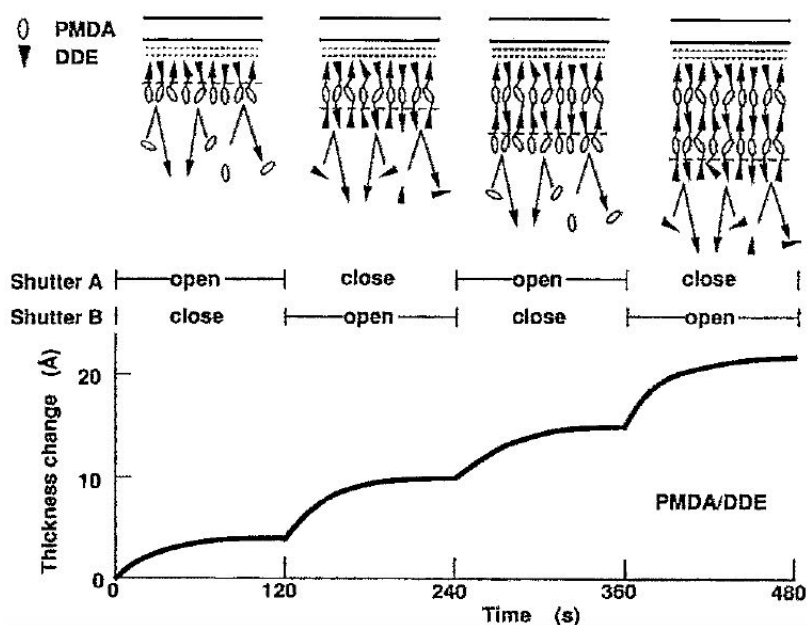


Figure 1-8: Polymer film growth by MLD using PMDA and DDE[6].

1-6-2 Core-shell particles encapsulated by ALD and MLD

Encapsulation by ALD process

There are many applications for ALD on particles. ALD can deposit protective and insulating coatings on particles to prevent oxidation or electrical conduction. The surface chemical properties of particles can be modified while retaining the bulk properties of the original particles. Such a core and shell structure is similar with the ‘passive’ host-‘active’ guest structures in the coating system, which would keep the inhibitor in a trapped state, and when corrosion happens, the inhibitor can be released triggered by the local pH changes as mentioned in the above section. Currently, fluidized bed reactors(FBR) are the first choice for particle ALD[49]. During fluidization, the upward force of the pressure drop across the particle bed equals the downward force of gravity on the particle bed. The equal forces lead to the fluidization of the particles. Although when working with particle less than 10 micrometers, particle aggregates form during fluidization, the aggregates are dynamic and the constant exchange of particles between the aggregates prevents the particles from being glued together during ALD. The vibration can also be applied to FBR, breaking the agglomerates in the reaction. Figure 1-9 shows the the TEM image of initial demonstration of ALD on particles in a fluidized bed, excellent conformal coatings of Al₂O₃ ALD can be observed on BN particles with a platelet shape[7].

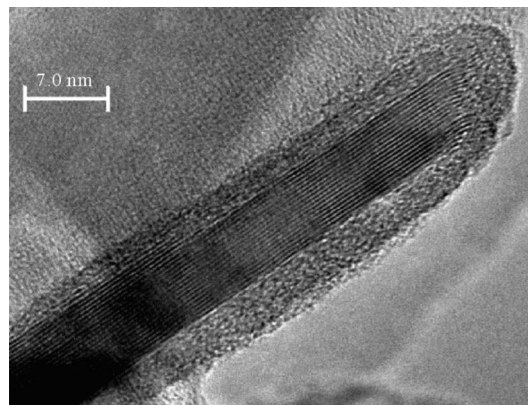


Figure 1-9: TEM image of HCV grade BN coated with Al₂O₃ ALD in a fluidized bed reactor[7].

Valdesueiro *et al.* have deposited aluminium oxide film by atomic layer deposition on titanium oxide nanoparticles in a fluidized bed reactor at room temperature and atmospheric pressure[8]. This research has made the coating of heat-sensitive material being possible and simplify the scale-up of ALD process. To characterize the deposition process, the thickness of the alumina film was determined by both TEM and elemental analysis (carried out using ICP-OES). The thickness was divided by the number of cycles to calculate the growth per cycle (GPC). ALD was performed with 4, 7, and 15 cycles by dosing a predefined amount of precursors, *i.e.*, trimethyl aluminium and water. The TEM pictures (Figure 1-10 a-c) and the distribution of the growth per cycle (Figure 1-10 d-f) for the 4, 7, 15 ALD-cycle experiments is illustrate in Figure 1-10, respectively[8].

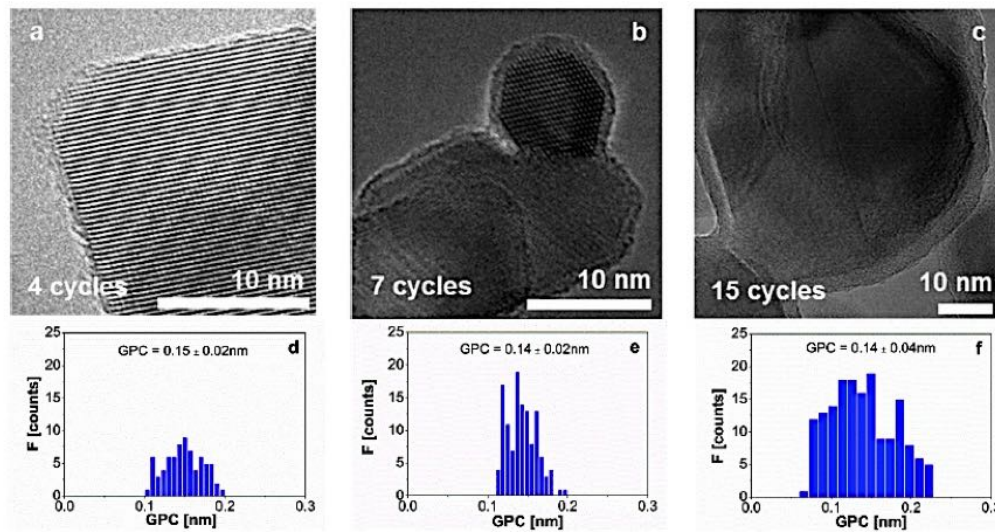


Figure 1-10: TEM images of the alumina film on TiO₂ nanoparticles for a dosing sequence of 3.5-10-2.5-10 min after (a) 4 ALD cycles; (b) 7 ALD cycles; and (c) 15 ALD cycles. (d) Distribution of the growth per cycle from the TEM pictures after 4 ALD cycles; (e) after 7 ALD cycles; and (f) after 15 ALD cycles. The mean growth per cycle and the standard deviation values are given in each histogram[8].

Although the histograms show some spread, from the TEM images it can be seen that the alumina coating on each particle is rather uniform and conformal. Figure 1-11 suggests a linear correlation between the number of cycles and the film thickness from TEM with a GPC of about 0.14-0.15 nm, although it would require more data points to draw solid conclusions about linearity[8]. To support the results from the TEM images, ICP-OES (Supplementary Information S5) on the samples was also performed to calculate the thickness of the alumina films. The values are in good agreement with those from the TEM, except for the 7-cycle experiment. The explanation for the difference of 7-cycle's result remains unsure[8].

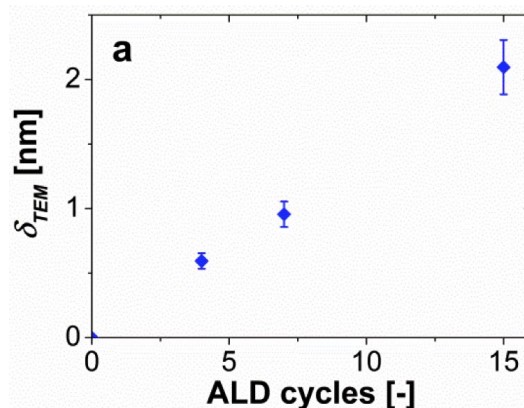


Figure 1-11: Thickness of the alumina film, determined from TEM images, for the different number of cycles for a dosing sequence of 3.5-10-2.5-10 min. The error bars represent the 10% error assumed in the image analysis[8].

However, the low thickness growth per cycles is advantageous for producing nanostructured materials, but for particles that require thicker coatings, this low growth again results in prohibitively long processing times. One solution to get a higher GPC was put forward by Garcia-Trinanes and Valdesueiro[50][8]: it was found that higher growth cycle rates can be achieved by dosing a significant excess of both precursors compared to the amount of reactive groups present at the surface at ambient conditions. The explanation was given as operation of the ALD process below the boiling point results in condensation or physisorption of reactant molecules, especially water, that can subsequently react with the other reactant during the next half-cycle, resulting in a CVD-like component of the ALD process. The mechanism is not completely understood yet. But GPC in the ALD process above boiling point indeed shows smaller values. Groner also found that in low temperature ALD process, partial CVD would occur when purging time become too short[9]. Therefore it can be expected that a longer dosing time and a shorter purge time in a relatively lower reactor temperature would result in excess of precursors and less re-evaporation of reactant thus resulting in an increase in growth per cycle.

The Al_2O_3 produced via ALD process with TMA and water as precursors is amorphous alumina[5]. Groner *et al.*[9] studied the properties of low temperature Al_2O_3 ALD films in the aspect of thicknesses, growth rates, densities, and optical properties. It was found that the densities of low-temperature alumina ALD coating are significantly lower than the 3.5-3.7 g/cm^3 value typically reported for amorphous Al_2O_3 [9]. The results are shown in Figure 1-12[9]. Although the density of the coating prepared is lower than typically reported amorphous Al_2O_3 , encapsulation with ALD Al_2O_3 still shows some good results. According to Groner's work, when low-temperature Al_2O_3 ALD films were grown on polyethylene terephthalate(PET) bottles to reduce gas diffusion, obvious lower CO_2 gas diffusion rates can be observed when comparing Al_2O_3 ALD coated PET bottles with uncoated PET bottles[9], which shows the ALD process as a promising encapsulation method.

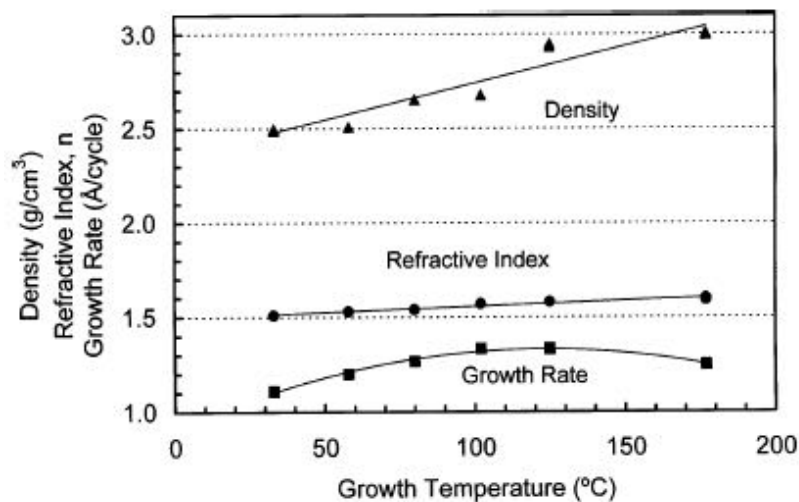


Figure 1-12: Ellipsometry data for Al_2O_3 ALD films grown using 300 reaction cycles on Si(100) substrates. The refractive index, growth rate, and density (calculated using ellipsometry and QCM data) are plotted versus growth temperatures from 33 to 177°C.[9].

Encapsulation by MLD process

Vasudevan *et al.* did research on the encapsulation of protein particles by MLD to attain a controlled release effect[10]. The protein particles were used as the substrate, and malonyl chloride and 1,2-butanediol as precursors. Figure 1-13 illustrates the reaction involved: the amine groups on the surface of the protein particles act as the active sites for reaction with the acyl chloride group of malonyl chloride during the initiating reaction (reaction 0); next, the unreacted acyl chloride group of malonyl chloride, which is now attached to the surface of the substrate, acts as the active site for the reaction with the hydroxyl group of 1,2-butanediol (reaction 1); in 1,2-butanediol, the hydroxyl group at position 1 is the most reactive (less sterically hindered) in ester formation; then the unreacted hydroxyl group of 1,2-butanediol reacts with the acyl chloride group of malonyl chloride (reaction 2). Only the first coating cycle involves reaction steps 0 and 1, while subsequent coating cycles involve reaction steps 1 and 2. After encapsulation, FTIR and dissolution experiment of coated particles are done to check the thickness of the coating and dissolution rate of the particles. It was found that with an increasing number of coating cycles of MLD, the thickness of coating increases and the dissolution rate decreases, which demonstrate that a controlled release effect is achieved by encapsulating the protein particles with MLD.

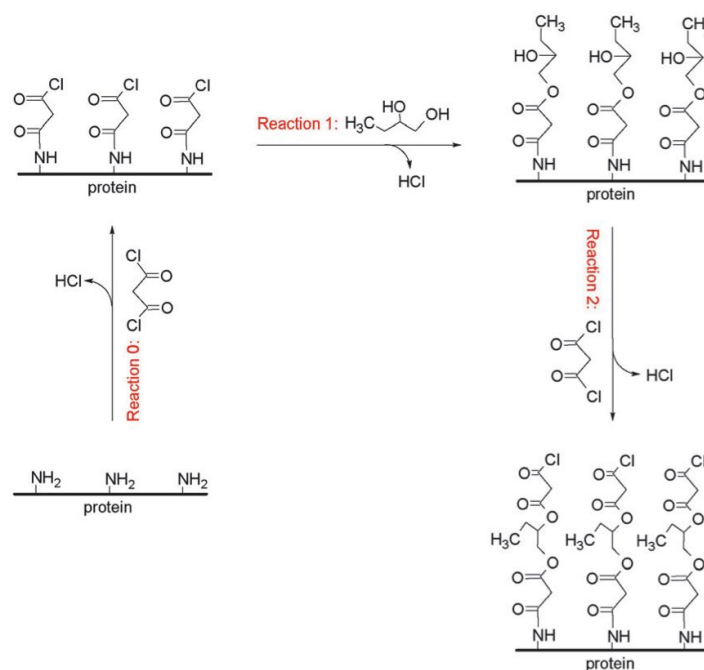


Figure 1-13: An illustration of the reactions involved in the MLD process[10].

1-6-3 Advantages of ALD and MLD

Although currently there is no research on the corrosion inhibitor encapsulating with ALD and MLD yet, numerous research has been done in the encapsulation of the solar cells via ALD and MLD. The organic solar cells undergo rapid degradation upon exposure to oxygen and water, and therefore, adequate encapsulation from ambient oxygen and water is an essential

requirement for the commercial viability of organic photovoltaic (OPV) cells[51]. In this regard, ALD is used for organic and flexible electronics as passivation layers with excellent film conformity can be grown at low temperatures. Similarly, the layer by layer Al_2O_3 film created by ALD and organic coatings by MLD, can be used as an encapsulation method to corrosion inhibitors with the same function of degradation preventing.

With ALD and MLD, smooth and conformal thin film coatings can be grown directly on the surface of single inhibitor particles without changing the property of bulk material, which would be a promising method for the inhibitor encapsulation strategy on self-healing anti-corrosion coating. With these methods, the size of the encapsulated inhibitors can be well controlled with less variation in the thickness of the coating by varying number of reaction cycles. The efficiency of getting the core-shell structure will not be limited by the loading capacity of the nano-carriers as the LbL assembled shells mentioned in the previous section any more. The stable alumina shell created in the ALD process, which can be dissolved in both acid and alkali environment, would lead to a pH triggered smart release of the inhibitors. Though stability of the organic coating created in the MLD process seems less stable than alumina according to the dissolving result[10], it can be enhanced by increasing the number of reaction cycles, thus probably creating a pH triggered leaching as well. Hybrid methods such as one cycle of ALD followed by a number of cycles of MLD process could also be possible as well as the modified ALD process preparing coating of aluminum alkoxide (alucone) by using different precursors. The hybrid methods and modified ALD methods can produce coatings with stabilities between the Al_2O_3 produced by ALD process and organic coating by MLD process thus fulfill a triggered release in a desired pH. Doping the uniform ALD/MLD encapsulated inhibitor into the coating, a homogeneous coating with evenly distributed inhibitor can be attained.

Material and Methods

2-1 Inhibitors

Three inhibitors are chosen to be coated via MLD and ALD, namely 2-mercaptobenzothiazole, cerium nitrate and lithium carbonate. The detail of the manufacturer, purity, product number are listed in Table 2-1, together with the encapsulation method used correspondingly.

Table 2-1: List of the inhibitor encapsulated.

Inhibitor	Manufacturer	Product number	Purity
2-Mercaptobenzothiazole	Sigma-Aldrich	M3302	97%
Cerium nitrate hexahydrate	Sigma-Aldrich	238538	99%
Lithium carbonate	Sigma-Aldrich	62470	99%

2-2 Encapsulation methods

In this part, the encapsulation method and process will be described in detail.

2-2-1 Pre-treatment of ALD and MLD

In order to get a better fluidization behavior during the reaction, the particles were grinded manually to reduced the size and sieved to get rid of the large particle. For the cerium nitrate, 5 g particles was grinded for 4 minutes every time, and then went through the sieve with the size of 180 μm . For the lithium carbonate, 2 g powder was grinded for 4 minutes every time, and went through the sieve in 53 μm . For the 2-MBT, 2 g of powder was grinded in a grinder for 4 minutes every time. But unfortunately, there was no sieve with suitable size for 2-MBT.

In order to improve the fluidization of 2-MBT, moisture in the powder is reduced by keeping the powder in the temperature of 100°C in the oven for 24 hours. However, the cerium nitrate cannot be dried because of the low melting point at 65°C.

Fluidization test is done to the powder in the fluidized bed reactor (FBR) to determine the minimum fluidization velocity, which is the minimum velocity required to keep the particles afloat in N₂ gas. The results of the fluidization test are attached in the Appendix II.

2-2-2 Molecular layer deposition (MLD)

Molecular layer deposition on inhibitors of 2-MBT and cerium nitrate powders were prepared. The powder are suspended in an upward gas flow of pure N₂, which is called a fluidized bed. N₂ acts as the carrier gas going through the bubblers for feeding the precursors into the fluidized bed reactor. A custom-built setup (shown in Figure 2-1) is used which is the same one as the schematic diagram of the experimental set-up done by Vasudevan *et al.* on the encapsulation of protein particles (shown in Figure 2-2).

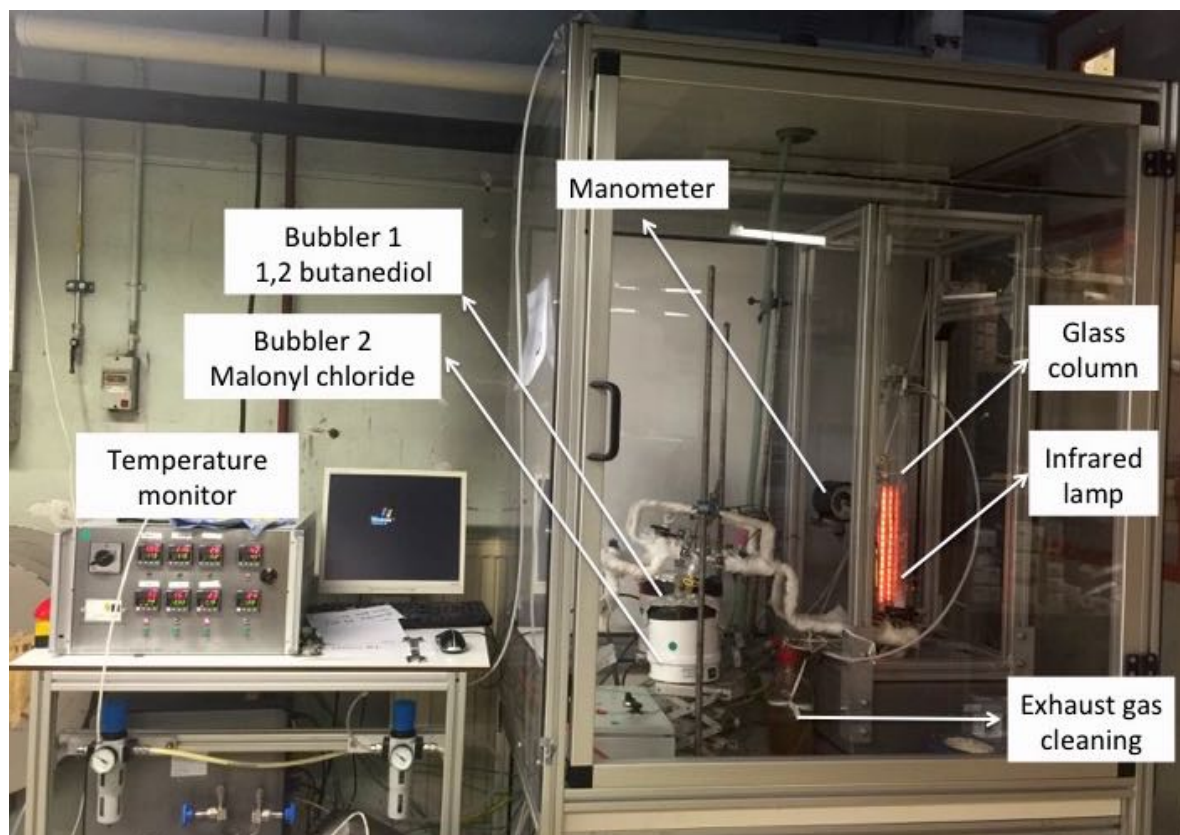


Figure 2-1: MLD setup used in the experiment.

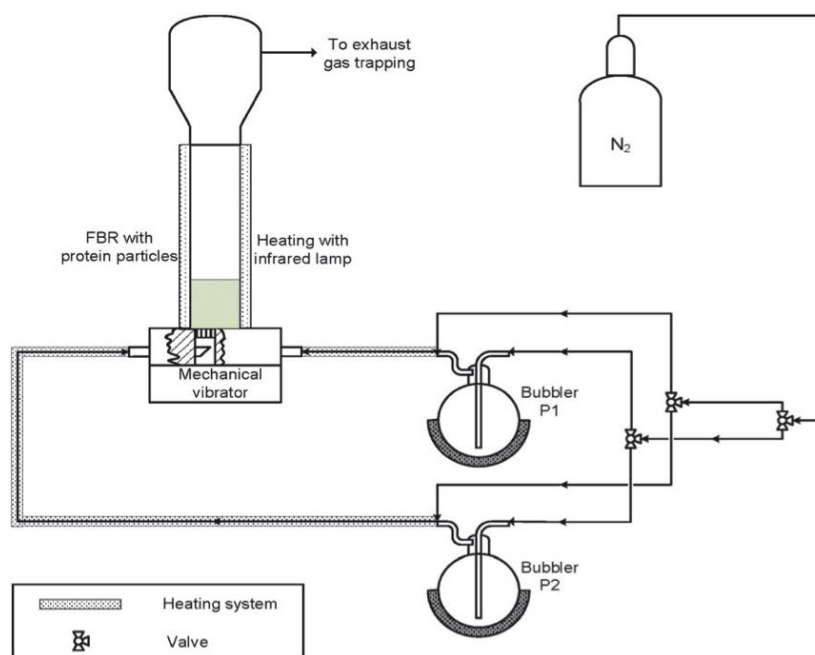


Figure 2-2: An illustration of the reactions involved in the MLD process[10].

The FBR consists of a vertical glass column with an inner diameter of 2.6 cm and a length of 50 cm with thermocouples inserted at the entrance. Distributor plates are provided at the entrance and exit of the FBR to ensure a uniform distribution of the inlet gas and avoid the powder goes out from the column with the gas flow. The FBR is kept in a certain range of temperature using a infrared lamp. There are two bubblers providing the precursors in the reaction. The unreacted precursor and by-product of the reaction is trapped using a mineral oil cold trap at the exit of the FBR. Mechanical vibration at 50 Hz is used to improve the fluidization of the particles, which is helpful to break the agglomerates formed during the coating process.

The precursors used in the MLD were malonyl chloride and 1,2-butanediol. Because of the low vapour pressures of malonyl chloride and 1,2-butanediol at room temperature, they were preheated in bubblers to 40°C and 115°C, respectively.

For the 2-MBT, 5 g powder was loaded in the column. The temperature of the FBR was maintained at around 70°C by controlling the infrared lamp. The minimum fluidization velocity was 1.88×10^{-2} m/s. Powders coated for different number of cycles were prepared, namely 5 cycles, 10 cycles and 20 cycles. One coating cycle consists of four steps: 2 min dosing of malonyl chloride; 7 min purging with pure N₂ to get rid of the unreacted precursor; 2 min dosing of butanediol and then 7 min purging with N₂. The dosing time was longer than the time required to feed the reactant. This was to ensure the adequate process of the reaction. The excess feeding of precursor is not a problem because the reaction is self-limiting. After MLD, the powder showed an increasingly intense orange color with the increasing number of cycles.

For the cerium nitrate, 5 g powder was loaded in the column. The temperature of FBR was kept at around 50°C. The minimum fluidization velocity was 1.88×10^{-2} m/s. Different from 2-MBT, in the beginning of the fluidization, cerium nitrate had the tendency to agglomerate.

Pre-treatment of purging the powder with pure dry N_2 in the FBR for about 30min was necessary to establish the stable fluidization. Dosing-purging-dosing-purging time used in coating cerium nitrate was 30s-5min-30s-5min. The powder was over exposure to the reactant to ensure the complete reaction. The purging time was long enough to clean the reactant in the column or left in the surface of the powder. Powders coated with 5 cycles, 10 cycles and 20 cycles were prepared. However, unlike 2-MBT, the color of cerium nitrate samples did not change after reaction.

Since the estimation of the dosing time in the reaction of 2-MBT was relatively long compared to cerium nitrate. Mass spectrum was used to detected the ions in the column to find the saturation point of the reaction in case of wasting the precursors. The results are shown in Appendix I.

2-2-3 Atomic layer deposition (ALD)

Atomic layer deposition on cerium nitrate and lithium carbonate was performed with the custom-built setup shown in Figure 2-3. The main principle of the ALD set up is the same with MLD.



Figure 2-3: ALD setup used in the experiment.

There were two groups of precursor used in ALD, namely trimethylaluminium (TMA, Akzo Nobel, semiconductor grade), H_2O and TMA, ethanol. The first group of precursor is a modified ALD process, which was to prepare the coating of Al_2O_3 , and the second group was to prepare the coating of aluminum alkoxide (alucone). Here, a mistake was made that the precursor used to prepare alucone should be a diol instead of ethanol[52]. However, there

is still some other alcohol impurities inside ethanol, the formation of alcane is still possible. Mechanical vibration at 50 Hz was used to improve the fluidization behavior of the particles.

For cerium nitrate, 5 g powder was loaded in the column. Temperature of FBR was kept at around 50°C due to the low melting point of cerium nitrate at 65°C. The minimum fluidization velocity was 1.88×10^{-2} m/s. Pre-treatment of purging the powder with pure N₂ in the FBR for about 30 min was still needed to take away some moisture and establish a stable fluidization. Dosing-purging-dosing-purging time used in coating cerium nitrate was 30s-5min-30s-5min. Powders coated with 4 cycles, 7 cycles and 10 cycles ALD were prepared. After ALD, the powder became much drier than before and the tendency of agglomerate disappeared, which was an indication that the crystal water was reacted in the ALD process.

For lithium carbonate, 5 g powder was loaded in the column. Temperature of FBR was kept at around 120°C since this kind of powder is not as temperature sensitive as cerium nitrate. The minimum fluidization velocity was 1.88×10^{-2} m/s. Dosing-purging-dosing-purging time was 1min-5min-1min-5min. In the beginning of the reaction, before TMA was dosed into FBR, the fluidization behavior was not good and there was no obvious rising of the fluid bed. However, after TMA was dosed, the fluid bed rose a lot ($\Delta h/h \approx 1$) and the powder started to fluidize. Powders coated with 4 cycles, 7 cycles and 10 cycles ALD were prepared.

It was originally intended to do the ALD for 2-MBT. However, after the TMA was dosed into the FBR, the fluidization of the powder became worse and worse. When the reaction was stopped and the powder was taken out from the column, smell of rotten eggs can be smelled, indicating that there was reaction between TMA and 2-MBT with H₂S to be the possible reaction product.

2-3 Characterization of the encapsulations

In this part the characterization of the coated inhibitors will be discussed.

2-3-1 SEM and EDS

Scanning Electron Microscope (SEM, Jeol JSM-6500F) was used to investigate the morphology of the particle before and after coating. Elemental mapping analysis was performed with Energy-Dispersive X-ray Spectroscopy (EDS). Powder samples were deposited on carbon tapes which can be glued on the sample holder. Carbon sputtering is used to deposit a thin film on the powder to reduce charging.

Cross sections of the ALD coated particles (ALD Ce(NO₃)₃ and Li₂CO₃) were prepared by dispersing the particle into resin by cold mounting. The cold mount resin was made by mixing 3.75 g of ClaroCit liquid and 6.25 g ClaroCit powder, both of which are from the manufacturer of Struers. The resin was cooled in the room temperature over night and then grinded in the sandpaper of 2500 and 4000. After grinding, the mounted samples were polished with the diamond and then cleaned in the ultrasonic bath with ethanol. However, the ALD Ce(NO₃)₃ reacted with the used cold mount resin, with a porous surface after cooling. The cross section of Li₂CO₃ was then observed with SEM with the aim of getting the interface of the coating and the bulk material.

2-3-2 Fourier transform infrared spectroscopy (FTIR)

Fourier transform infrared spectroscopy (FTIR) was used to detect the surface species. The spectra were acquired by a Nicolet 6700 spectrometer operated using a liquid N₂ cooled detector. The FTIR spectra of coated cerium nitrate and lithium carbonate samples were obtained in the transmission mode of the spectrometer by pressing the coated sample into KBr salts, making a transparent pellet consists of 1wt% sample and 99wt% KBr. The data were collected with a resolution of 6 cm⁻¹ averaged over 1000 scans. FTIR spectra of 2-MBT were obtained in the attenuated total reflection (ATR) mode and the data were collected with a resolution of 6 cm⁻¹ averaged over 128 scans.

2-3-3 UV-vis spectra

The leaching of the 2-MBT from the polymer coating created by MLD process was tested by UV-vis spectrophotometer. Coated 2-MBT sample were dissolved in the solutions with different pH, namely HCl solution of pH2, neutral solution of distilled H₂O and NaOH solution of pH12. The concentration was 3×10^{-4} M[53]. Blank samples without encapsulation were prepared as reference. The prepares solutions were left for couple of days before testing in order to get the complete dissolving and leaching. The characteristic absorption peaks of 2-MBT in the wavelength from 700 nm to 200 nm were detected by UV-vis spectrophotometer.

2-3-4 ICP-OES

Inductively Coupled Plasma-Optical Emission Spectroscopy (ICP-OES, PerkinElmer Optima 3000DV) was performed to obtain information on the amount of alumina present and make an estimate of alumina coating thickness. 20 mg coated sample was dissolved in a mixture of 1 ml 37% HCl and 1ml 69.5 % HNO₃ solution. After destruction, the samples were diluted to 10 ml with milli-Q water and then analyzed with ICP-OES to determine the mass fraction of aluminum in the samples. The concentration of Li and Al were calculated in the lithium carbonate samples and the concentration of Ce and Al were calculated in the cerium nitrate samples with the calibration solutions for each element.

The leaching of the coated cerium nitrate and lithium carbonate from the coating were detected by ICP-OES as well. Coated cerium nitrate and lithium carbonate were dissolved in the acid of HCl (pH2), neutral solution of distilled water and alkali solution of NaOH (pH12) in the concentration of 10⁻³ M. Blank samples without encapsulation were also prepared as reference. All the solutions were left for a couple of days before taken to ICP-OES test. The dissolved coated lithium carbonate samples were taken to the ICP-OES to detect the concentration of Li and Al ion; the coated cerium nitrate samples were taken to the ICP-OES test to detect the concentration of Ce and Al ion. After the coated cerium nitrate samples were dissolved in alkali solutions, flocculent precipitates of Ce(OH)₃ can be observed in the bottom of the solution. Approximately 10 ml clear liquid in above of the precipitate were taken out as the liquid parts of the coated cerium nitrate in NaOH solution samples, and the precipitates were dissolved with sufficient hydrochloric acid as the precipitates parts of the coated cerium nitrate in NaOH solution sample, both of which were taken to the ICP-OES to detect the Ce and Al ions in the solution.

2-4 Characterization of the anticorrosion performance

After the characterization of the epoxy coating, the coated samples are chosen to be doped into epoxy coating. And the healing and anticorrosion performance would be evaluated by electrochemical impedance spectroscopy (EIS).

The coating formulation consists of two components: bisphenol-A type epoxy resin (Epikote 828) and polyamide hardener (Ancamine 2500). Table 2-2 shows the composition and amount of the component to prepare the epoxy. The resin and hardener are stirred separately from each other before mixing together. The encapsulated inhibitor was then added to the mixture and stirred at 800 rpm for 3 minutes to ensure full dispersion of the pigments in the resin. The resulting mixture was then cast on the cleaned AA2024-T3 panels using a bar coater with a nominal thickness of 200 μm . The coated samples were dried and cured at 50°C for 15 hours yielding coatings with a dry thickness of 150-210 μm . The coated substrates were artificially damaged with a knife, leaving a 2 cm long and about 200 μm wide scratch in the plate.

Table 2-2: Composition of the epoxy.

Component	Amount
Bisphenol-A epoxy resin	
Epikote 828	9.26 g
MIBK	5.74 g
Polyamide hardener	
Xylene	2.39 g
Ancamine 2500	5.37 g
Silane	0.74 g

Electrochemical impedance spectroscopy (EIS) was performed to characterize the anticorrosion performance of the scribed coating doped with the encapsulated inhibitors. Measurements were performed in 0.05 M sodium chloride solution after 3 hours, 1 day and 4 days' immersion. The test conditions were 10 mV sinusoidal perturbation voltage in the 60 kHz-10 mHz range. A three electrode cell was used with the exposed AA2024-T3 sample as working electrode with an exposed area of 12.56 cm² (0.04 cm² effective exposed area, the scratch), a platinum counter electrode and a saturated calomel reference electrode (SCE). The testing cells were made by a cylindrical tube of 4 cm diameter, clamped to the testing samples with a rubber ring.

After the EIS measurements, the morphology of the scratch area were observed with VHX-5000 digital microscope.

2-5 Flow diagram of the experimented approach

Figure 2-4 shows the flow diagram of the experimented approach. The modified ALD process in which ethanol and TMA were used as the two precursor is abbreviated as MALD.

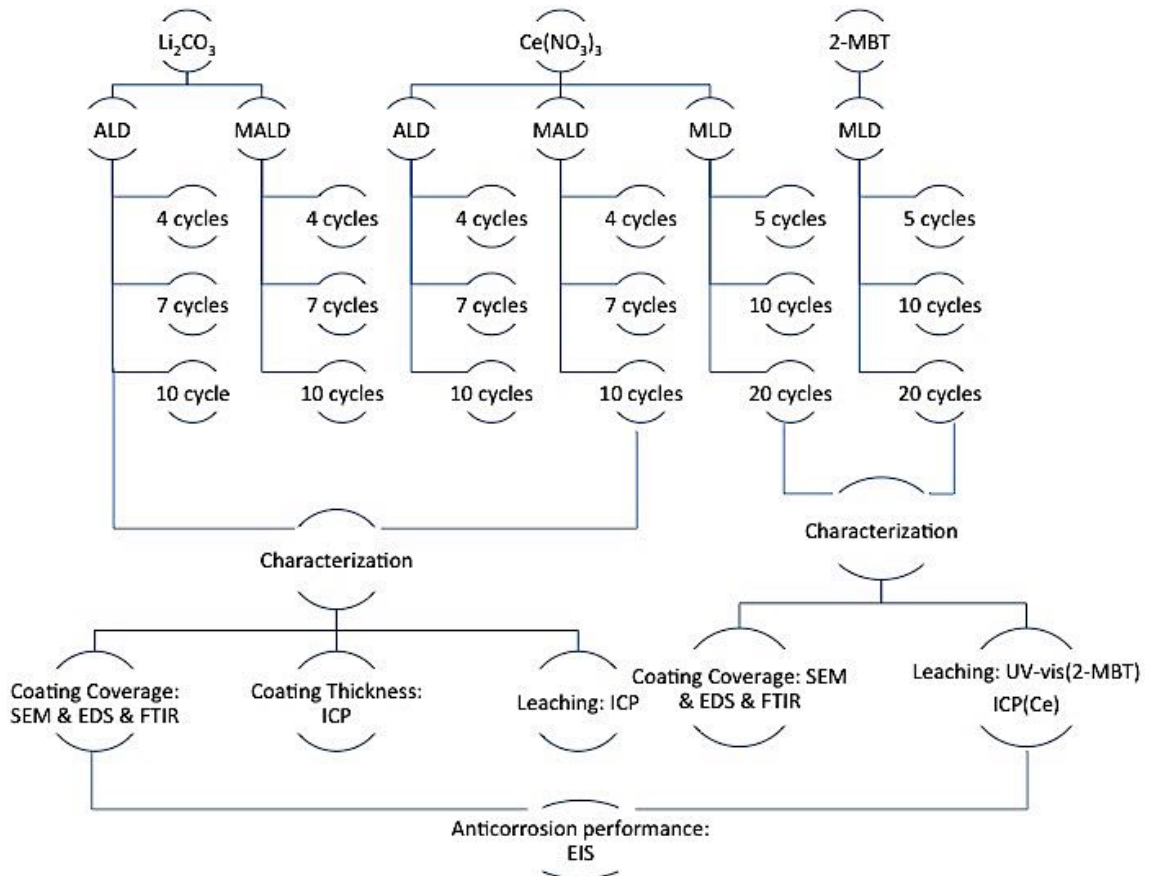


Figure 2-4: Flow diagram of the experiment process.

Results and Discussion

3-1 Characterization of the encapsulation

In this section, results of the different inhibitors after encapsulation will be presented and discussed. The chapter will start with the characterization result of different coated inhibitors, including the proof of the existence/non-existence of the coating, followed by the estimated thickness of the coating and then the leaching of the inhibitor from the coating. Table 3-1 lists the methods used correspond to different aspect of the coating.

The following abbreviations will be used in this part to address the different samples: the material after grinding without any coating will be referred as blank materials which are blank lithium carbonate, blank cerium nitrate and blank 2-MBT. The modified ALD process in which ethanol and TMA are used will be referred as MALD. The coated sample will be referred as the name of the inhibitor with the process and number of cycles (Li_2CO_3 ALD4,7,10, Li_2CO_3 MALD4,7,10 $\text{Ce}(\text{NO}_3)_3$ ALD4,7,10, $\text{Ce}(\text{NO}_3)_3$ MALD4,7,10, 2-MBT MLD5,10,20).

Table 3-1: Overview of the characterization of the encapsulation.

Sample	Coating	Thickness	Leaching
Li_2CO_3 ALD	SEM & EDS & FTIR	ICP-OES	ICP-OES
$\text{Ce}(\text{NO}_3)_3$ ALD	SEM & EDS & FTIR	ICP-OES	ICP-OES
$\text{Ce}(\text{NO}_3)_3$ MLD	SEM & EDS & FTIR	/	ICP-OES
2-mbt MLD	SEM & EDS & FTIR	/	UV-vis

3-1-1 Encapsulations of lithium carbonate

Characterization of the encapsulation of lithium carbonate will be discussed in the following part. Corrosion inhibitor of lithium carbonate was encapsulated via 4, 7 and 10 cycles' ALD

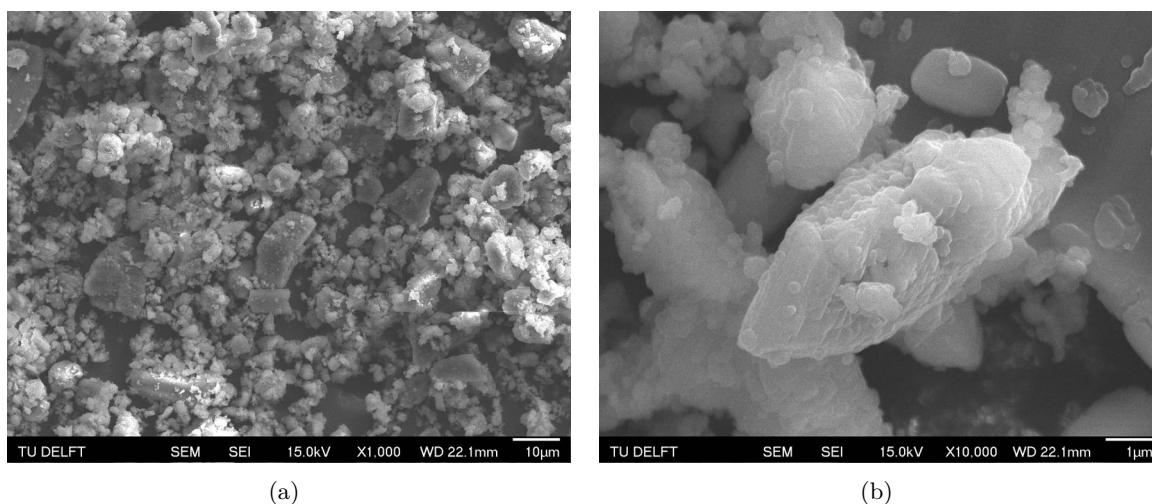


Figure 3-1: SEM images of blank lithium carbonate after grinding in (a) $\times 1000$ and (b) $\times 10000$.

and 4, 7 and 10 cycles of MALD process respectively. SEM and EDS analysis was focused on the ALD10 sample. FTIR, calculation of the coating thickness and leaching test was carried on all the samples.

Lithium carbonate after grinding

SEM and EDS analysis was performed on the blank lithium carbonate powder without alumina coating as a reference sample. The morphology of the blank lithium carbonate is shown in Figure 3-1. It can be seen from Figure 3-1 that most of the particles are far less than the size of the sieve which is $53 \mu\text{m}$. Particles are not homogeneous, some of which are even in the size of several microns. Due to the small size, the powder has the tendency of agglomeration after grinding. With a higher magnification, it can be seen that the surface of a single particle of lithium carbonate is flaky and uneven. Figure 3-2 shows the backscattered electron image used in EDS measurement with the position of the points indicated. Table 3-2 shows the results corresponding. Because the sample was coated with carbon to reduce charging, the spectrum of EDS was cut off at 300 eV to cut the peak of carbon which should be at 0.28 keV. Element of Li is too light to be detected by EDS. As a result, in the EDS spectrum of blank lithium carbonate samples only the peaks of O can be detected, as shown in Table 3-2 that the atomic percentage of O is 100%. More EDS point measurement can be referred in Appendix III.

Table 3-2: EDS elemental concentration measurements results of blank lithium carbonate correspond to points indicated in Figure 3-2(b).

Point	O atom%
1	100
2	100
3	100

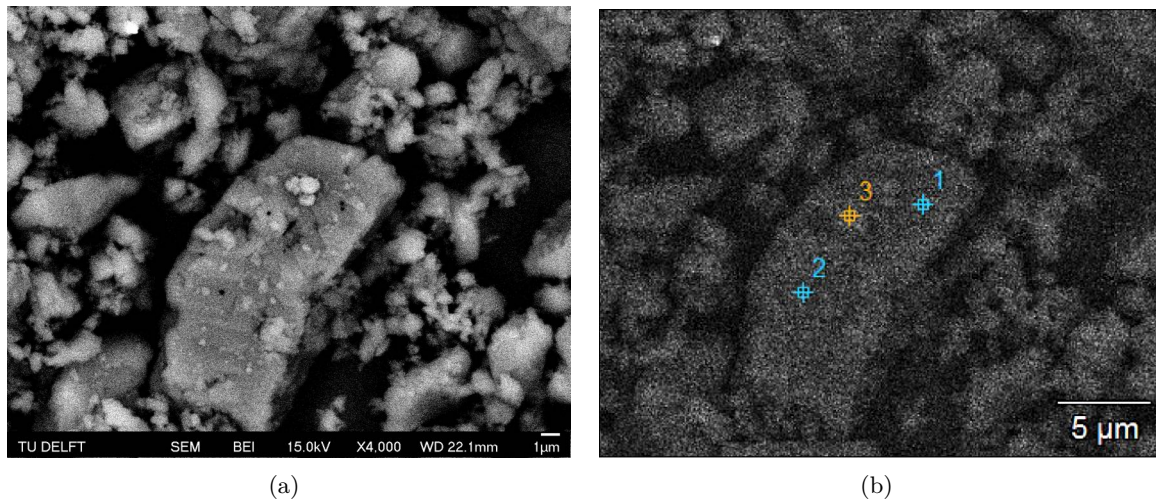


Figure 3-2: (a) Backscattered electron image of blank lithium carbonate. (b) Image of blank lithium carbonate with EDS measurement points indicated.

Lithium carbonate after ALD coating

ALD and MALD process were performed on the lithium carbonate. The hydroxyl in the surface of the particles acted as the active site where the coating was grown. Figure 3-3 shows schematically about the expected reactions in the ALD and MALD process, as well as the structure of the coating[11]. Mistake was made as mentioned in the experiment part that in MALD process ethanol was used as precursor instead of ethylene glycol. However, characterization was still performed on the mistaken MALD samples.

After encapsulation, SEM and EDS were performed on the particles coated with 10 cycles ALD to investigate the resulting morphology and coverage after coating, which are shown in Figure 3-4. It can be observed that the amount of small particles decreased dramatically and the surface of the single particle become smoother and less flaky after coating. A possible explanation for the decrease of small particles is that during fluidization these particles do not remain in the fluidized bed and instead remain suspended in the gas flow and end up in the cyclone. This often happens in fluidized beds, as a gas flow sufficient to fluidize larger particles is often able to retain smaller particles in polydisperse powders[54]. Another explanation could be that powder agglomerated in the ALD process. Small particles glued together in a common shell during the ALD, which could be reduced or prevented by increasing the frequency and amplitude of the vibration.

Points measurement of EDS results are shown in Table 3-3 correspond to the points indicated in Figure 3-5, as well as the elemental mappings detected by EDS. Small amount of aluminium was detected in every point measurement after 10 cycles' ALD, indicating that a thin layer of alumina was formed during ALD process. The variation in Al content can be explained by the fact that EDS actually measures X-rays originating from a region at and below the surface, the result of which could be influenced by the tilted or uneven surface. Another possible explanation could be that the thickness of aluminium oxide coating is not homogeneous. More EDS point measurement results can be found in Appendix III. From elemental mapping, it can be seen that element of O and Al are concentrated in the area where the particle is, which

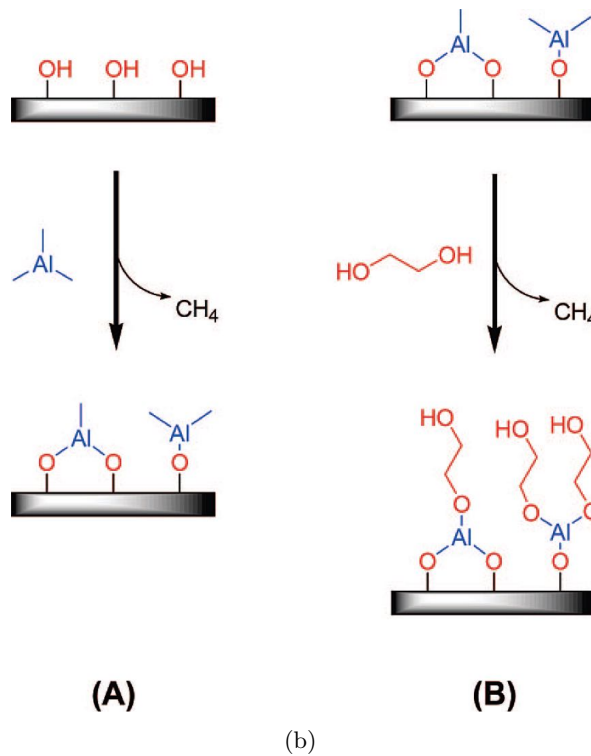
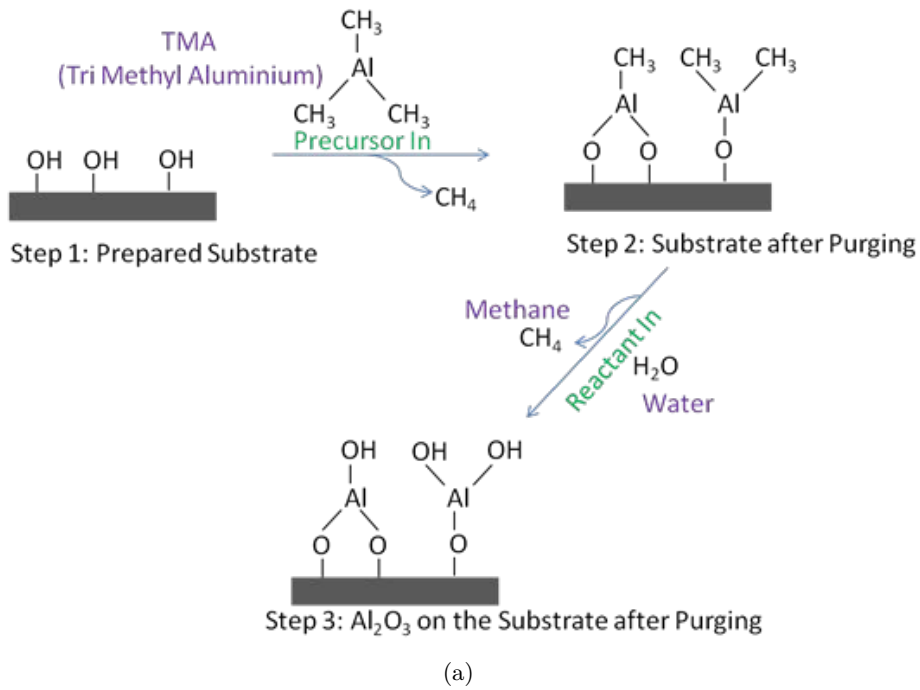


Figure 3-3: Illustration of the reactions in (a) ALD and (b) MALD process[11] on lithium carbonate.

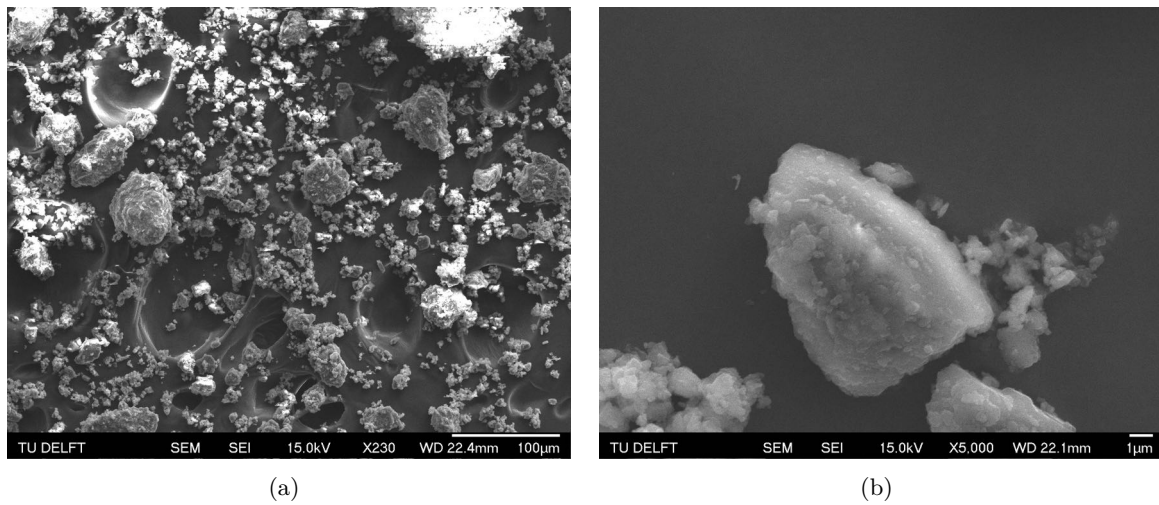


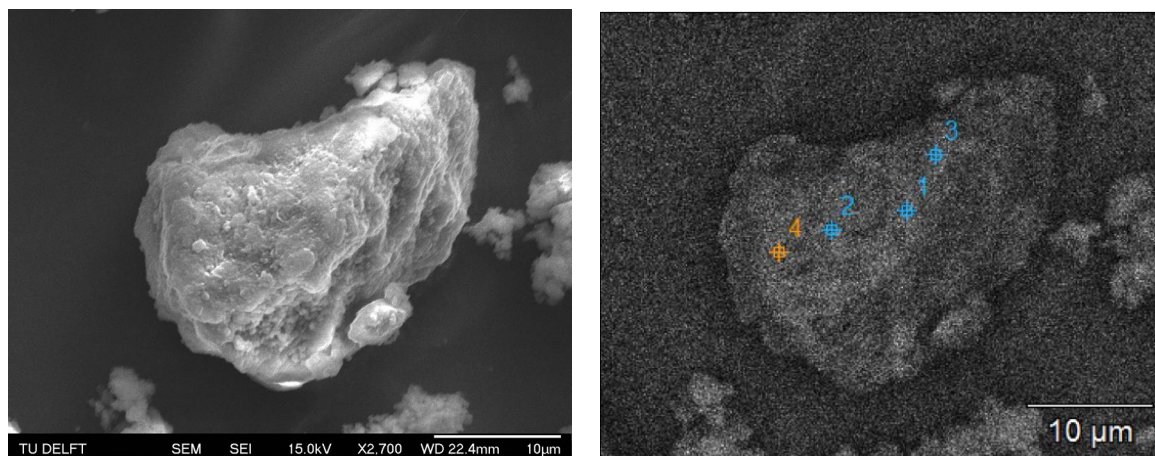
Figure 3-4: SEM images of lithium carbonate after 10 cycles' ALD coating in (a) x230 and (b) x5000.

gives a further proof that aluminium oxide layer is formed in the surface of the particle.

Table 3-3: EDS elemental concentration measurements results of lithium carbonate after 10 cycles' ALD process correspond to points indicated in Figure3-5(b).

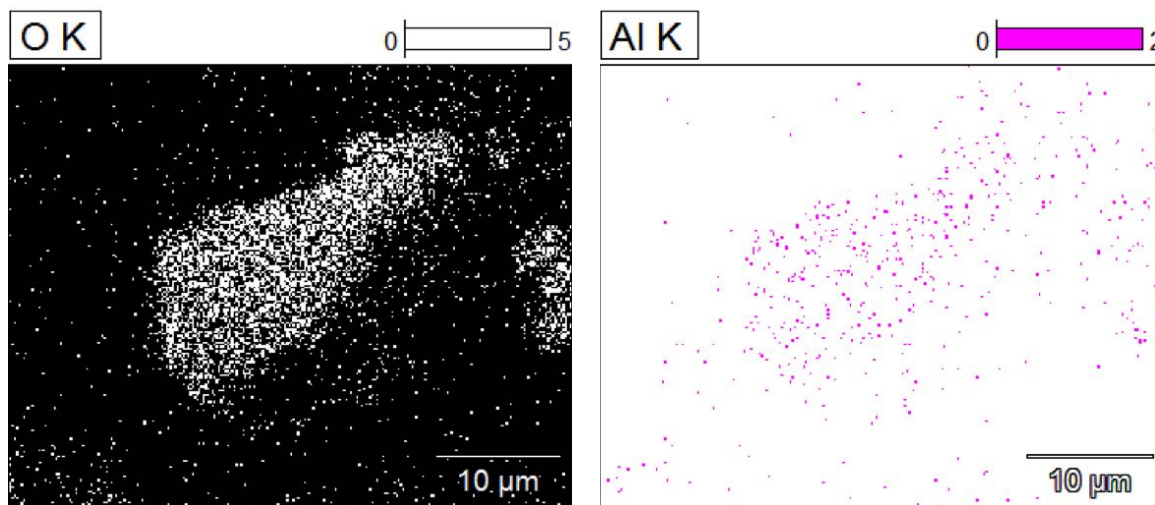
Point	O atom%	Al atom%
1	98.63	1.07
2	96.26	3.74
3	98.88	1.12
4	97.02	2.98

FTIR was performed with the aim of further confirming the Al_2O_3 coating in the surface of the sample via the peak of Al-O bond. However, the highly surface-sensitive ATR mode was tried first, but the spectrums were with large noises. So, samples were pressed into KBr salts and then tested in transmission mode to reduce the noise peaks. According to literature, Al-O bond inside the Al_2O_3 prepared by ALD process should be in the position of $900\text{-}1000\text{ cm}^{-1}$ [55][56]. Figure 3-6 shows the FTIR spectrum of the tested lithium carbonate ALD samples, with blank Li_2CO_3 as reference. It can be seen that in the spectrum, the position of the all the peaks are exactly the same between the coated samples and blank sample. The intensive double peaks in the position of 1495 and 1429 cm^{-1} comes from the C-O asymmetric and symmetric stretching mode of Li_2CO_3 ; the peak in 1088 cm^{-1} comes from the C-O bond and the peak in 864 cm^{-1} was attributed to the CO_3 group bending mode[57]. While there is another explanation that the peak in 864 cm^{-1} comes from the out of plane C-O bending vibration and the small peak in about 740 cm^{-1} is due to the in plane C-O bending vibration[58]. Anyhow, the Al-O bond from the Al_2O_3 coating created during the ALD process was not observed. The reason could be the amount of Al_2O_3 was too little to be detected or the peak of Al-O bond was buried in the noise as the background. However,



(a) SEM-SEI image of a single particle used in the EDS measurement.

(b) Image with position of points measurement indicated.



(c) Oxygen elemental mapping.

(d) Aluminum elemental mapping.

Figure 3-5: EDS results of lithium carbonate particle after 10 cycles' ALD coating with (a) $\times 2700$ SEM-SEI image of a single particle used in the EDS measurement, (b) image with position of points measurements indicated, (c) oxygen elemental mapping and (d) aluminum elemental mapping.

since the position of peaks from C-O bond also appear in the wavelength around 1000 cm^{-1} , there could also be an overlapping of the peaks of C-O bond and Al-O bond, thus peak of Al-O bond was not found. The spectrum of Li_2CO_3 MALD sample is shown in Figure 3-7, in which exactly same peaks with Li_2CO_3 ALD samples can be observed. The reason of the missing of the bonds in alucone could be the same as explained for the missing of Al-O bond in the ALD FTIR spectrum.

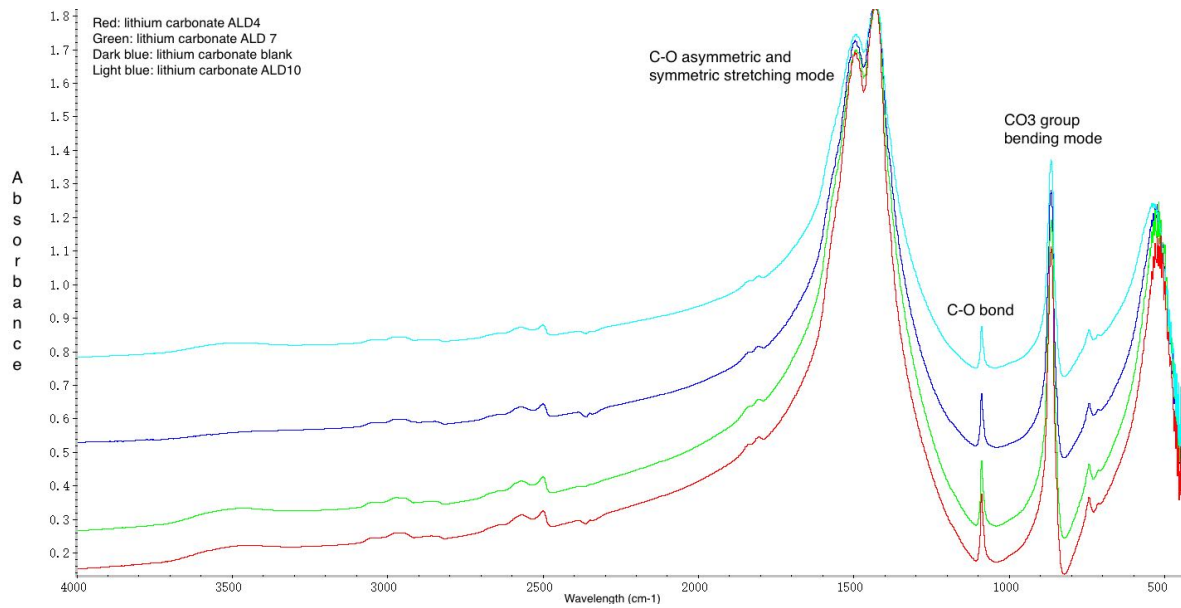


Figure 3-6: FTIR spectrum of lithium carbonate after 4, 7 and 10 cycles' ALD coating and the blank lithium carbonate.

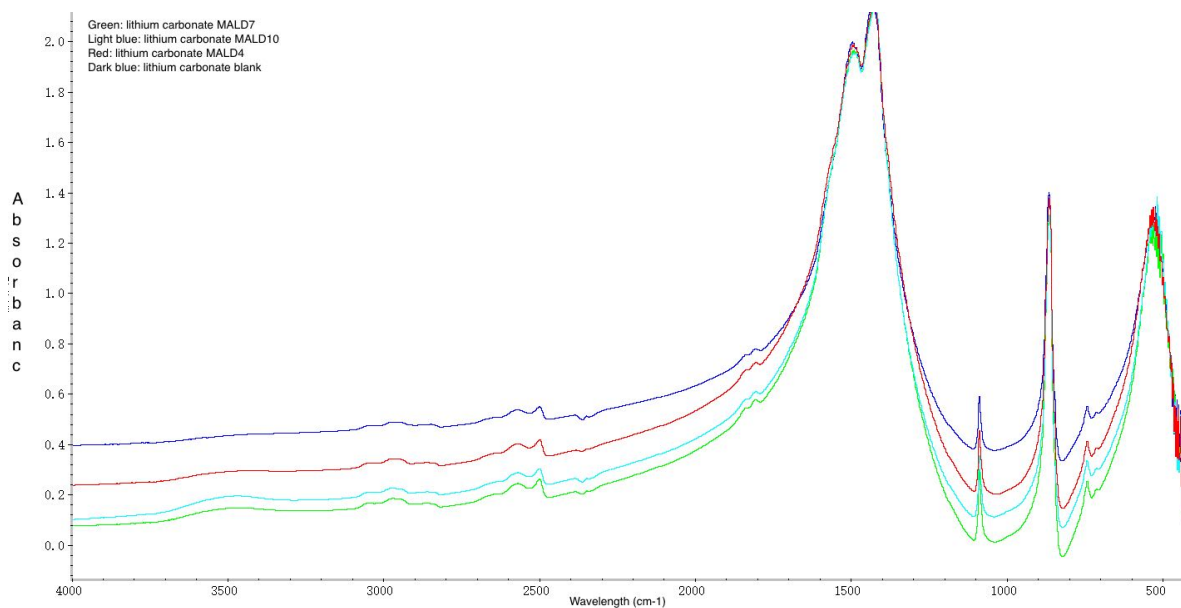


Figure 3-7: FTIR spectrum of lithium carbonate after 4, 7 and 10 cycles' MALD coating and the blank lithium carbonate.

To obtain more information about the coating, thickness of the alumina film was measured with ICP-OES. After destructing the coated particles in the mixture of strong acid, the corresponding volume of aluminium oxide in each particle $V_{Al_2O_3}^{1P}$ can be calculated with the mass fraction of aluminium in the coated sample x_{Al} using Equation 3-1[8], assuming that the lithium carbonate particles are spherical with a diameter $d_{Li_2CO_3}$ and density $\rho_{Li_2CO_3}$. Here, $26.5 \mu m$ was used as an average diameter of the powder after ALD by estimation and density of $2.11 g/m^3$ was used according to the data sheet provided by the manufacturer. $M_{Al_2O_3}$ and M_{Al} are molecular mass of alumina and aluminium. A factor of 1/2 is because there are 2 moles of Al in one mole of Al_2O_3 . The density of the film of aluminium oxide $\rho_{Al_2O_3}$, which was $2500 kg/m^3$, is found by Groner *et al.*[9] for ALD at $25^\circ C$. Then Equation 3-2[8] was used to calculate the thickness of the film δ based on the volume of alumina per particle determined with Equation 3-1.

$$V_{Al_2O_3}^{1P} = \frac{x_{Al}}{1 - \frac{M_{Al_2O_3}}{2 \cdot M_{Al}} \cdot x_{Al}} \cdot \frac{M_{Al_2O_3}}{2 \cdot M_{Al}} \cdot \frac{\rho_{TiO_2}}{\rho_{Al_2O_3}} \cdot \frac{\pi}{6} \cdot d_{3,2}^3 \quad (3-1)$$

$$\delta_{ICP} = \frac{\sqrt[3]{\frac{6}{\pi} \cdot V_{Al_2O_3}^{1P} + d_{3,2}^3} - d_{3,2}}{2} \quad (3-2)$$

Figure 3-8 shows the result of the calculated thickness of alumina films. It can be found that with the increasing number of cycles during ALD and MALD, the thickness of the coating is growing nearly linearly. The growth per cycle (GPC) is about 4.56 nm for alumina in ALD process and 3.98 nm for alucone in MALD process according to the slope of the trend line. Theoretically, in the MALD process, in which ethanol and TMA are used as the precursors, the reaction should stop after the first cycle because there is only one hydroxy in a ethanol molecular as a result the chain of alucone cannot be elongated. However, it was interesting that the alumina film is still growing in a linear way as increase of the number of cycles. This could be explained as there are several of impurities inside the ethanol used, including methanol, 2-propanol, water, *etc.* according to the data sheet provided by the manufacturer. From the GPC of alumina and alucone calculated, larger deposition rates is obtained than expected, which should be between 0.1 to 0.3 nm per cycle according to literature[8]. The large deposition rates can be explained as the presence of CVD type of growth as mentioned in Section 1-6-1. The residual CVD type of growth occurs in ALD process usually is the consequence of condensation of reactants, in particular H_2O [8]. The purging time used should be long enough to re-evaporate the precursors in the reaction, so the excess water comes from the moisture inside the powder itself and the column, which cannot be removed completely in the reaction temperature of $120^\circ C$. However, for the application of inhibitor encapsulation in which a higher coating thickness would be more helpful, the CVD component occurs at ambient conditions is desirable. CVD component can be increased by decreasing the reactor temperature and shortening the purging time.

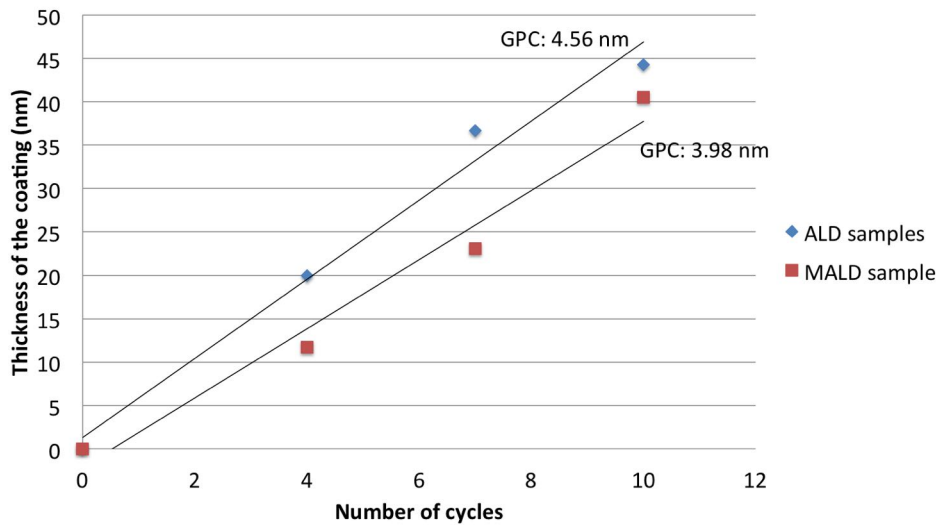


Figure 3-8: Calculated thickness of alumina film on lithium carbonate with 4, 7 and 10 cycles' ALD coating and MALD coating, respectively.

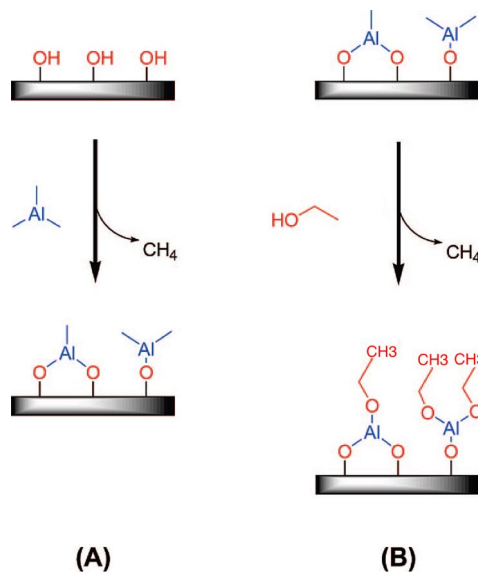


Figure 3-9: Reactions in MALD process with TMA and ethanol as precursors.

Backscattered electron image were performed with the aim of getting a layered structure varying with light and shade (a darker coating on a lighter particle in this case). Preparation of the cross section of the ALD 10 lithium carbonate particles were carried out, by loading the sample into the cold mounting resin. The agglomeration increased the difficulty of sample preparation and at the end the powder was not well embedded in the resin as there were always voids in the edges of the cross section of a single particles. A layered structure from backscattered electron image was not obvious in the edge of the cross section of the particle (as shown in Figure 3-10(a)). The reason could be the limitation of resolution of the equipment (about 5 nm) and the contrast is not enough. EDS was performed with 7kv electron beam to

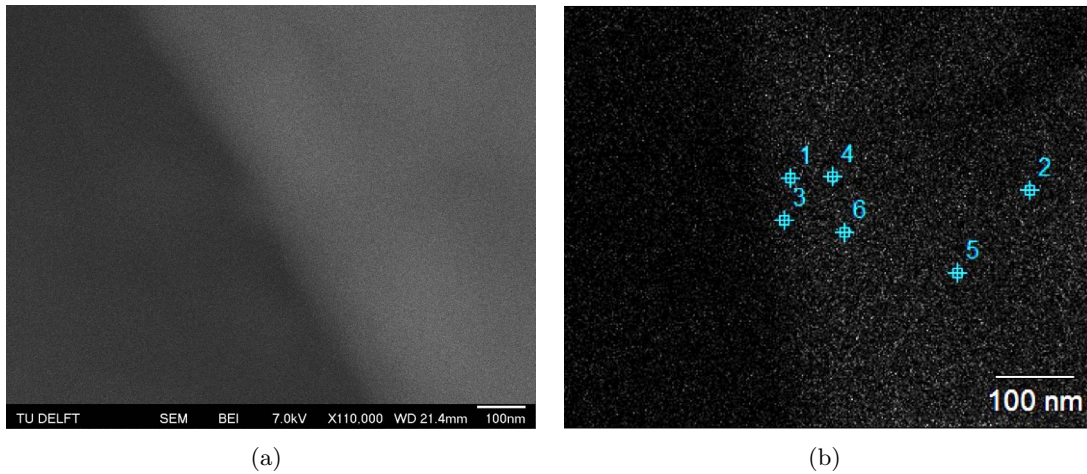


Figure 3-10: (a) Backscattered electron image of the edge of cross sectional lithium carbonate ALD 10 sample. (b) Image of cross sectional lithium carbonate ALD 10 sample with EDS measurement points indicated.

see if there is any different in the composition between edge and bulk part. Table 3-4 shows the results. In the point shooting in the edge part of the sample (point 1, 3, 4 and 6), small amount of Al can be detected, while the point shooting in the bulk part of the sample (point 2 and 5) shows the composition same as the pure lithium carbonate with 100 atom% of O detected. The position of the points containing Al is as least 100 nm away from the edge, which is thicker than the calculation based on the ICP-OES results. This could be explained as the incomplete dissolution of the coated particles in the acid before the ICP-OES test.

Table 3-4: EDS elemental concentration measurements results of the cross sectional lithium carbonate ALD 10 samples from image in Figure3-10(b).

Point	O atom%	Al atom%
1	95.95	4.08
2	100	
3	97.24	2.76
4	96.73	3.27
5	100	
6	97.43	2.57

After proving the existence of the alumina coating, the leaching of the inhibitor after coating is tested with ICP-OES as well. Figure 3-11 shows the results of the leaching test. The content of Al is too low to be detected since the solution prepared is in a low concentration of 10^{-3} M Li_2CO_3 . All the ICP-OES data in the leaching can be found in Appendix IV. The concentration of Li ion in complete leaching should be approximately 14 mg/L. As is clear from Figure 3-11, the concentration of all the blank samples exceed the expected value, indicating that the powders were overweighing when the solutions were prepared. Though

preparation of the solution were not that accurate, some trend can still be observed. It shows in the bar chart that the MALD samples in HCl has a reduced dissolution as well as the dissolution of all the ALD and MALD in the neutral solution of water. The reduced dissolution effect shows that the coating was taking effects to some extent in the leaching test. However, due to the big error in the preparation of the solution, same procedure was repeated on the blank, ALD 4 and ALD 10 samples, to get a more reliable result, which is shown in Figure 3-12. It can be seen that this time, in all the blank solutions, Li ion detected was almost about 14 mg/L (except for the one in NaOH solution), which means that relatively accurate solutions were made this time. As can be seen from the bar chart, alumina coated lithium carbonate samples indeed have a small tendency of dissolving less in water as the number of cycle increases during ALD process. While in acid and alkali solutions, the concentrations of lithium ion were more or less the same. When we look into the Pourbaix diagram of Al (shown in Figure 3-13), Al_2O_3 is stable between pH 4 and pH 8.5. While it dissolves in both acid and alkali solution. This is in agreement with the ICP-OES results.

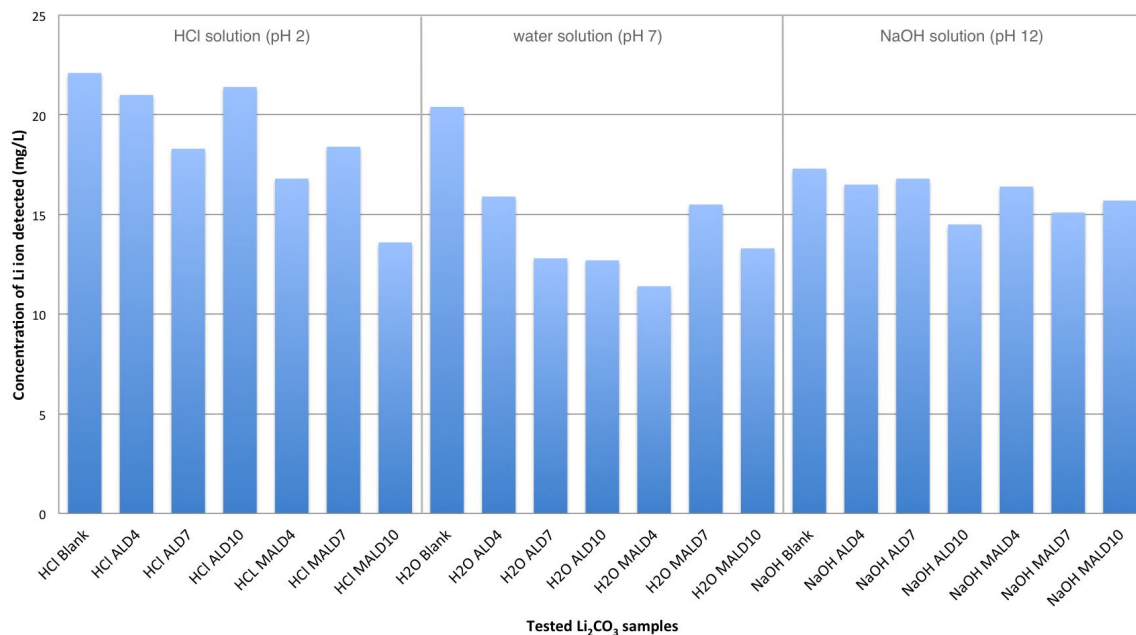


Figure 3-11: ICP-OES results in the leaching test of coated lithium carbonate including samples with 4, 7 and 10 cycles' of ALD and MALD coating dissolving in HCl, water and NaOH solutions.

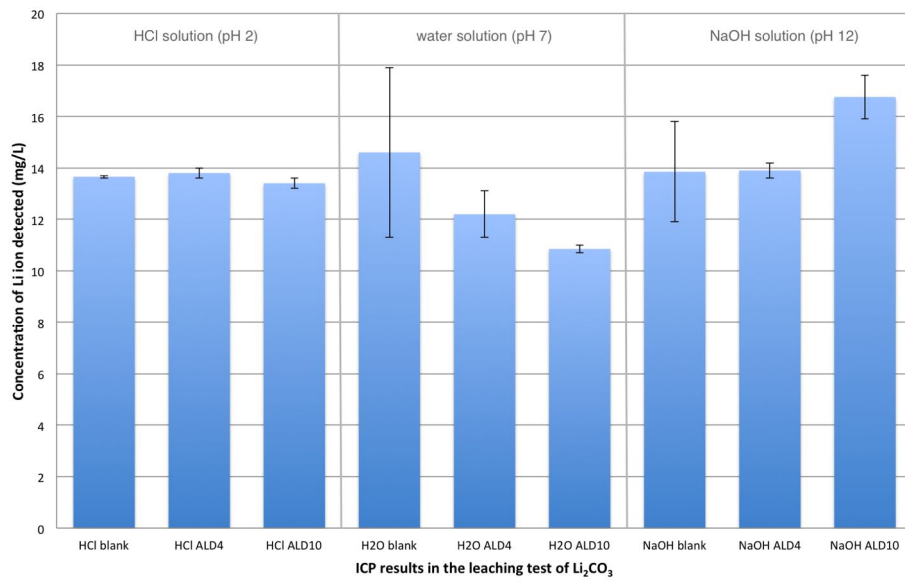


Figure 3-12: Second repetition ICP-OES results in the leaching test of ALD4, ALD10 and blank lithium carbonate dissolved in HCl, water and NaOH solution.

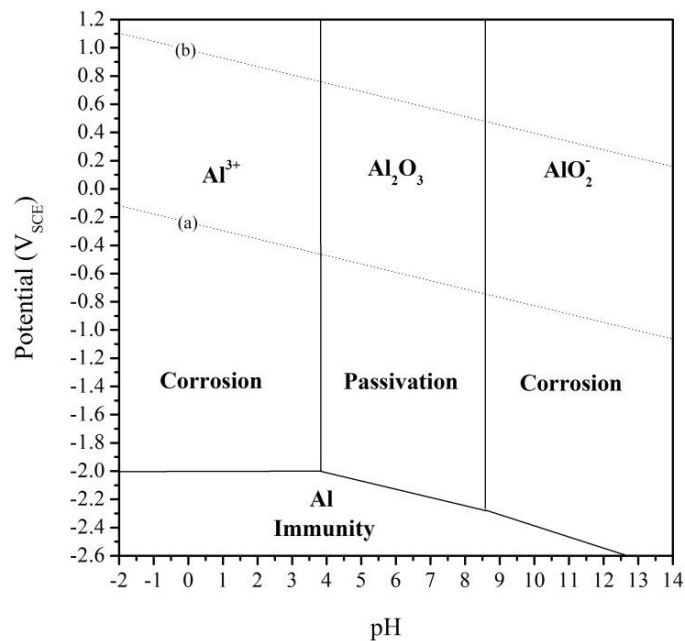


Figure 3-13: Pourbaix diagram of Al.

In the leaching test of encapsulated lithium carbonate, the tendency of reducing the dissolving of the inhibitors in the neutral solution by the coating is indeed observed, though the effect is much less than expected. After several days immersion, most of the inhibitors were leached even in the neutral solution. There are two possible explanations: the first one is the insufficient coverage of the alumina coating and the second one is the alumina coating is not

dense enough. The insufficient coverage of the coating may be caused by the lacking of active site in the surface of particle or the insufficient exposure of the precursors, both of which will lead to a formation of an island shaped coating rather than a complete coverage. It would be helpful to use a more regular and homogeneous raw material and a longer overexposure and purging time. For the second possibility, it also could be that the alumina coating is not thick and dense enough, with water gradually penetrating through the coating and then the inhibitor being dissolved. It has been mentioned in Section 1-6-1 that the density of low temperature ALD Al_2O_3 film is significantly lower than the commonly reported amorphous alumina films. From Figure 1-12, the density of ALD Al_2O_3 in the reaction temperature of 120°C is about 2.8 g/cm^3 , probably with microporosity inside, resulting the permeabilities of water. Increasing the reactor temperature and number of cycles could be the solution to this problem.

3-1-2 Encapsulations of cerium nitrate

Characterization of the encapsulation of cerium nitrate will be discussed in the following part. Cerium nitrate inhibitor was encapsulated via 4, 7 and 10 cycles' ALD, 4, 7 and 10 cycles' of MALD and 5, 10, 20 cycles' of MLD process, respectively. SEM and EDS analysis were focused on the ALD 10 and MLD 20 sample. FTIR, calculation of the coating thickness and leaching test were carried out for all the samples.

Cerium nitrate after grinding

SEM analysis was performed on the blank cerium nitrate powder without alumina coating for comparison, as shown in Figure 3-14. It can be observed in Figure 3-14(a) that even though the powder is sieved to eliminate the large particles, the size is still very polydisperse after grinding. There are some big particles in the size of about $200 \mu\text{m}$ as well as small particle in the size of 10s of μm according to the estimation with the scale bar. Figure 3-14(a) is a closer look. Elemental mapping analysis was performed on the blank cerium nitrate with EDS. Figure 3-15 shows the backscattered electron image used in EDS and the image with EDS measurement points indicated and the results are listed in Table 3-5.

As can be seen that there are some variation in all the elements, especially the content of N. This can be explained that the stacking of the particle causes an uneven distribution of the carbon coated during the carbon sputtering. The peak of N, which is close to peak of carbon, is overlapping and thus influenced by the peaks of carbon. Then the atomic percent of O and Ce is further influenced by the less accurate concentration of N since the sum of the three element should be 100%. Another reason could be that the particles are irregularly and the surface is not flat. As mentioned above that EDS actually measures X-rays originating from a region at and below the surface. An irregular and uneven surface would influence the penetration depth of the measurement thus influencing the results. It is surprisingly to find that Al is also detected in point 4. It seems like the initial salt has Al contamination or impurity, and this is further proved by the result of ICP-OES which will be discussed in the following parts.

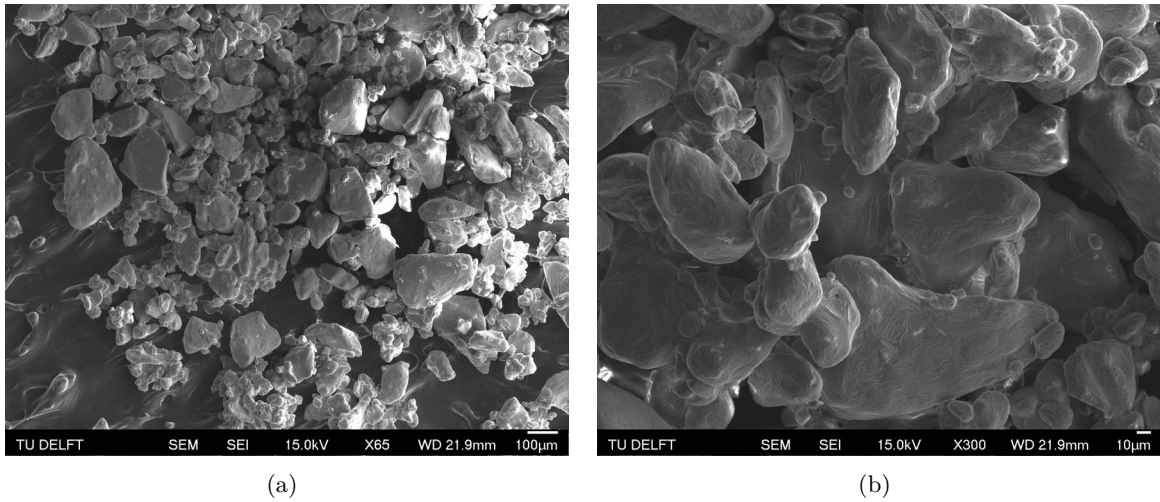


Figure 3-14: SEM images of blank cerium nitrate powder after grinding in magnifications of (a) x65 and (b) x300.

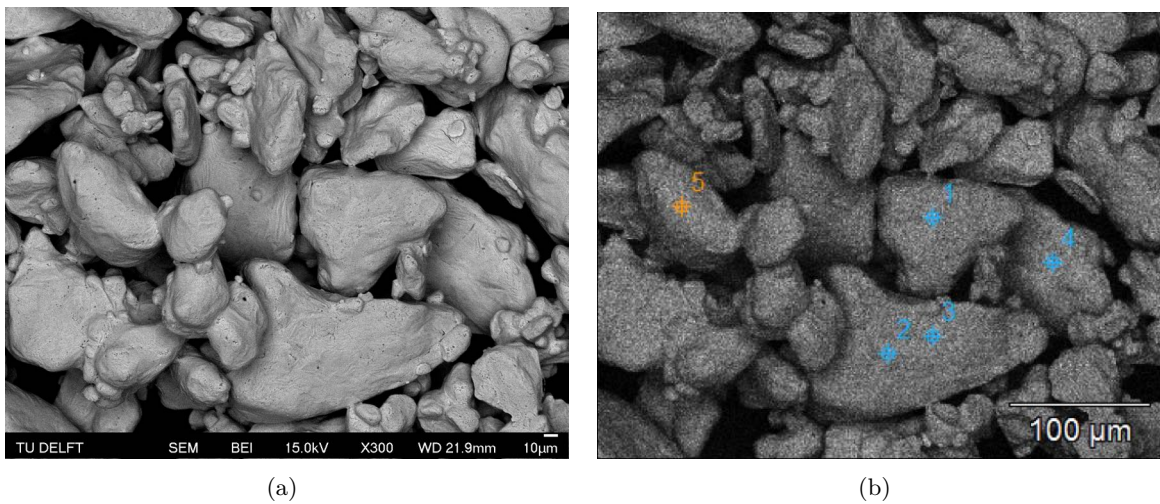


Figure 3-15: (a) Backscattered electron image of blank cerium nitrate. (b) Image of blank cerium nitrate with EDS measurement points indicated.

Table 3-5: EDS elemental concentration measurements results of blank cerium nitrate correspond to the points indicated in Figure 3-15(b)

Point	N atom%	O atom%	Al atom%	Ce atom%
1	16.01	55.78		28.21
2	9.49	61.40		29.11
3		76.3		23.7
4		65.08	2.76	32.16
5	18.45	66.38		15.17

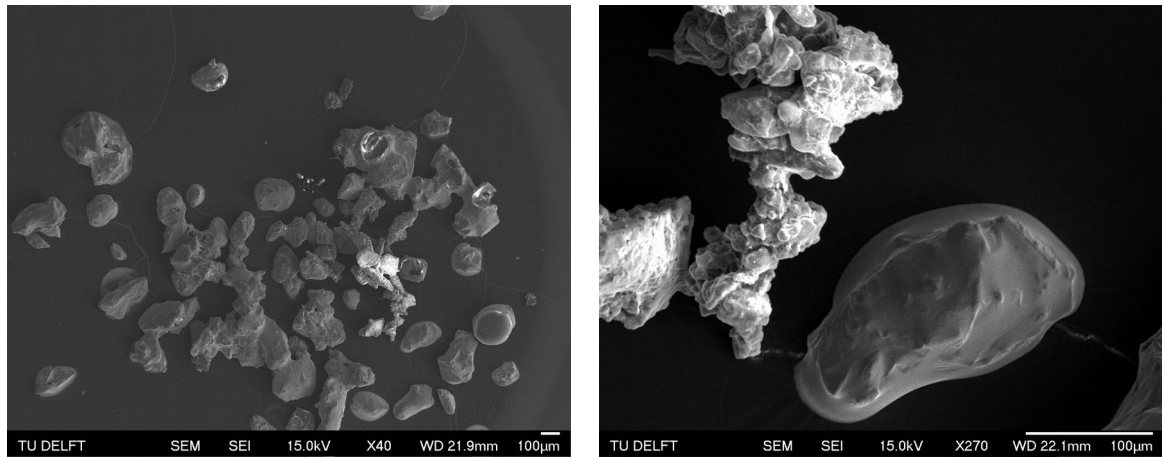
Cerium nitrate after ALD coating

ALD and MALD process was performed on the cerium nitrate. The crystal water attached to the NO_3^- and the hydroxyl ion in the surface of the particles acted as the active site where the coating was grown. The expected reaction and coating structure were the same with the reaction in the ALD and MALD process on lithium carbonate, shown in Figure 3-3(a) and 3-3(b). Same mistake was made in the experiment part that in MALD process ethanol was used as precursor instead of ethylene glycol. However, characterization was still performed on the mistaken MALD samples.

After encapsulation, SEM and EDS were performed on the particles coated with 10 cycles ALD to investigate the resulting morphology and coverage after coating, which are shown in Figure 3-16. It can be seen from the overview of the morphology (shown in Figure 3-16(a)), two morphologies can be distinguished after coating: the one with a smooth surface and the other one with a rough surface. The smooth one is not significantly different from the particle without coating (Figure 3-14). Figure 3-16(b) shows a comparison between the 'smooth' particle and the 'rough' agglomerate, in which it can be seen that the 'smooth' one is a single particle and the 'rough' one is agglomeration of small particles. Figure 3-16(c) and Figure 3-16(d) show the detail of the rough surface. The small particles in Figure 3-16(d), are about 200 nm according to the scale bar in a higher magnification. These small particles are not found in the raw material of cerium nitrate after grinding, which could be the reaction product from the ALD process. Results of EDS analysis of the two kind of particles are shown in Table 3-6 and Table 3-7. Figure 3-17 are the pictures indicating the measured points with EDS.

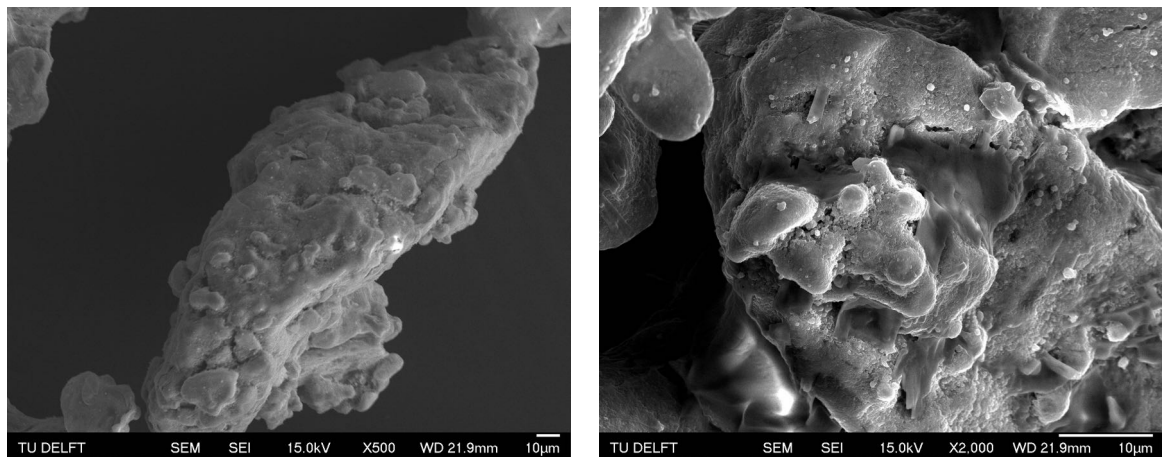
In Table 3-6, point one and two was removed because of too much noise peaks. It can be seen from Table 3-6 that most points in the particle with smooth surface after coating, the content of Al is very low (less than 1 atom%), indicating that the particle is not really covered with alumina since the content in the blank cerium nitrate can be as high as 2.76% (Table 3-5). However, the content of Ce in different position of the same particle varies significantly, the reason of which remains unknown. This could also partly be caused by the tilted or uneven surface of the particle which has been mentioned twice above. More EDS measurements results can be found in Appendix III.

Table 3-7 shows the EDS results of the elements contents in the particles with a 'rough surface'. It can be observed that the content of Al is in a high level (10 times higher concentration than



(a) Overview of the morphology of cerium nitrate after 10 cycles' ALD coating

(b) Comparison of the two morphologies of cerium nitrate after ALD.



(c) Agglomeration of alumina in ALD 10 cerium nitrate in x500.

(d) Agglomeration of alumina in ALD 10 cerium nitrate in x2000.

Figure 3-16: SEM images of cerium nitrate powder after 10 cycles' ALD process with (a) overview of the morphology, (b) comparison of the two morphologies of cerium nitrate after 10 cycles' ALD coating, (c) agglomeration of alumina in cerium nitrate with magnification of x500 and (d) agglomeration of alumina in cerium nitrate with magnification of x2000. magnification.

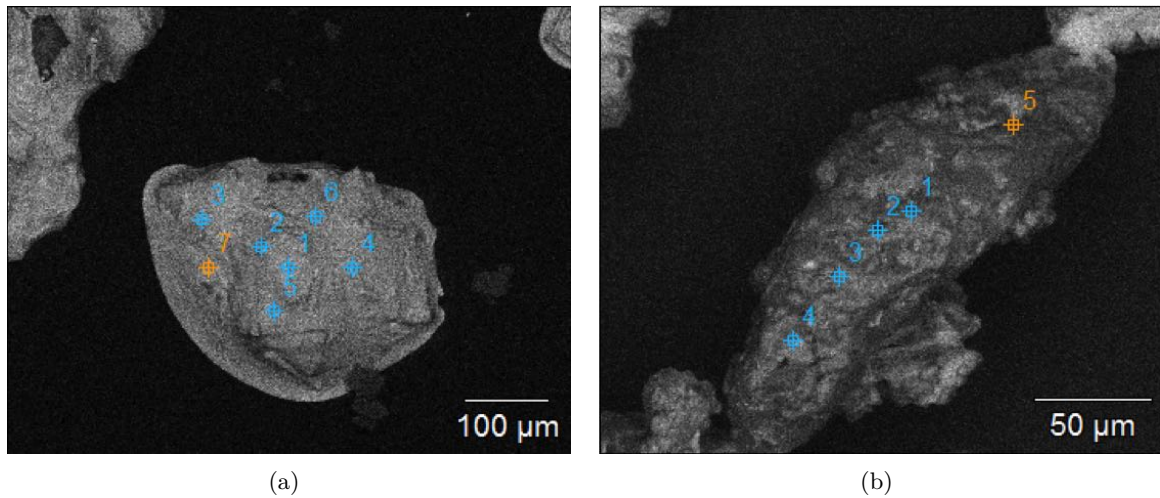


Figure 3-17: Image with EDS measurement points indicated correspond to (a) the single particles with smooth surface after ALD 10 coating (b) the agglomerations with rough surface after ALD 10 coating.

in Li_2CO_3 , Table 3-3), indicating that the agglomerates contain a high amount of alumina. Also, the content of Ce is lower than the raw material before coating (Table 3-5). Combining with the fact that alumina is not formed on the surface of single cerium nitrate particles after ALD, it can be inferred that small particles of alumina are formed agglomerating with the cerium nitrate with a relatively small size after grinding. The agglomeration is in a mixture state rather than making a shell for the cerium nitrate particles. And the single cerium nitrate particles remain almost the same before and after the ALD process.

Table 3-6: EDS elemental concentration measurement results corresponding to the smooth surface ALD 10 particles with positions of points indicated in Figure 3-17(a).

Point	O atom%	Al atom%	Ce atom%
1	/	/	/
2	/	/	/
3	76.77	0.40	22.83
4	81.72	0.27	18.00
5	44.01	0.90	55.09
6	80.89	0.76	18.34
7	44.94	4.01	51.05

Table 3-7: EDS elemental concentration measurements results correspond to the rough surface ALD 10 particles with position of points indicated in Figure3-17(b)

Point	O atom%	Al atom%	Ce atom%
1	69.45	24.92	5.62
2	66.17	27.92	5.91
3	66.47	23.39	10.14
4	43.84	42.89	13.27
5	69.47	26.14	4.39

The formation of the two kind morphology after ALD process can be explained as follow: the pretreatment on the cerium nitrate particles in the FBR reduces the moisture in the FBR to some extent and breaks the agglomeration. However, the crystal water, which can be expressed as $\text{Ce}(\text{NO}_3)_3 \cdot 6\text{H}_2\text{O}$, still exist in the powder. When TMA was dosed into FBR in the first half cycle, the bond of crystal water in the single particle with a larger size was broken first and the water moisten other particles, in the meanwhile reacts with TMA forming alumina particles. The excess dosing time of water moisten the particles again in the following cycles. It is known that $\text{Ce}(\text{NO}_3)_3$ absorb the moisture in the air, so the over-exposure makes the particle form the crystal water again. It is calculated that there are 0.07 mol crystal water in the 5 g cerium nitrate in the FBR. The dosing time was more than 10 times overexposure. The 30s dosing time in the 0.6 L/min N_2 flow provide 1.38 mol water, which is more than enough for both the recrystallization and reaction with TMA. In the end, the alumina particles formed during ALD process deposited on the $\text{Ce}(\text{NO}_3)_3$, forming the 'rough surface' agglomerations as can be seen in the SEM images shown above. With the number of cycles increases, the growth of alumina is mainly concentrated on the agglomerations, resulting in the big particle of $\text{Ce}(\text{NO}_3)_3$ remains uncoated.

The solution of this problem seems difficult because $\text{Ce}(\text{NO}_3)_3 \cdot 6\text{H}_2\text{O}$, which has a low melting point at 65°C , is quite temperature sensitive. Drying the powder to eliminate the crystal water by temperature control is not possible. Other precursors which avoid introducing water into FBR is suggested. The use of ozone could be an good substitute precursor for water. Mass spectrum is suggested to be used to monitor ion current in the FBR to further determine the behavior of reactant inside FBR.

FTIR was performed on the ALD and MALD samples of cerium nitrate. However, same situation was found with the lithium carbonate ALD/MALD samples, in which the bond from the coating cannot be observed. Figure 3-18 shows the spectrum of $\text{Ce}(\text{NO}_3)_3$ samples. The broaden peak in 3387 cm^{-1} comes from the OH stretching mode in crystal water; the peak in 1628 cm^{-1} comes from crystallization water as well; peaks in the wavelengths of 1460, 1384 and 1038 cm^{-1} are ascribed to the vibration of the NO_3^- bonds[59][60]. The position of peaks in the $\text{Ce}(\text{NO}_3)_3$ MALD samples are also exactly the same with $\text{Ce}(\text{NO}_3)_3$ ALD samples. The possible reason why the bonds in Al_2O_3 and alucone are missing can also be addressed on the shell material was too small to be detected or the overlapping of between the Al-O peak and NO_3^- vibration, which has be explained in the previous section.

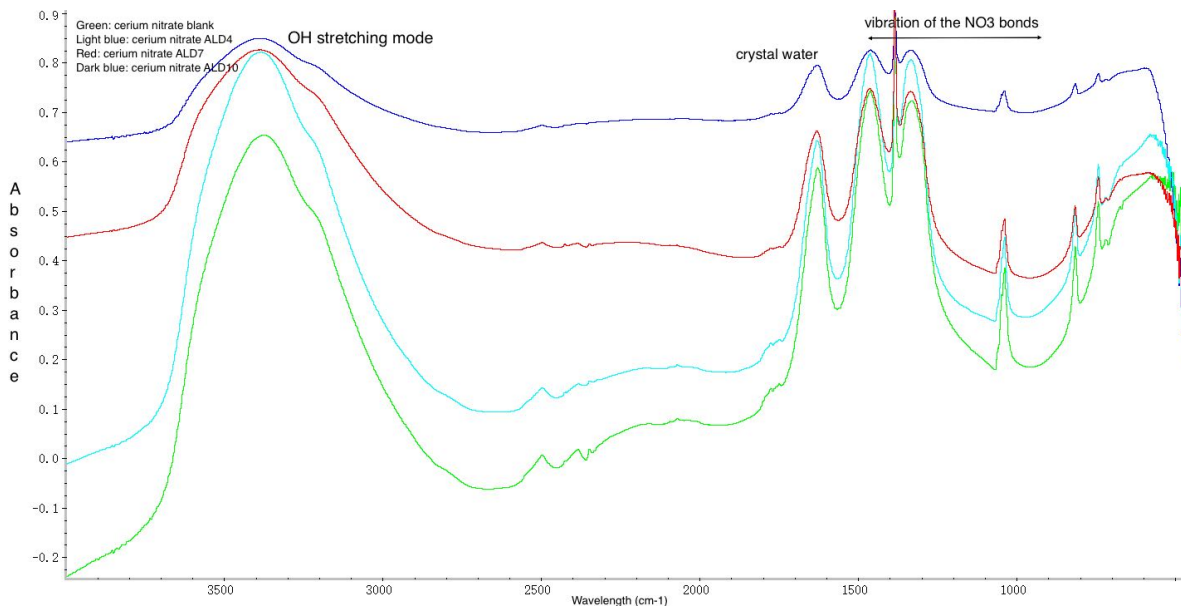


Figure 3-18: FTIR spectrum of cerium nitrate after 4, 7 and 10 cycles' of ALD coating.

The content measurement of Al is also performed on the cerium nitrate ALD and MALD samples by ICP-OES with blank cerium nitrate particles as a reference. The procedure of test and the calculation are the same with the thickness measurement of lithium carbonate ALD samples. Here, assuming all the Al detected are forming a homogeneous coating in the cerium nitrate particles with the size of $90 \mu m$. Figure 3-19 shows the result of the measurement. From the plot, a linear growth of alumina can be observed in both ALD and MALD process, the GPC of which are 95.4 nm and 107.3 nm according to the slopes of trend lines respectively. It has been mentioned that MALD process should cease theoretically with ethanol and TMA as precursors (explained with Figure 3-9). However, linear growth of the mistaken MALD process was observed as well in the case of cerium nitrate. Except for the reason of impurities inside ethanol explained in the case of lithium carbonate, the crystal water also plays a role. Crystal water also takes part in the ALD process reacting with TMA and producing Al_2O_3 . The large GPC of ALD and MALD in cerium nitrate is also interesting to be noted. As mentioned before, GPC of ALD process are usually 0.1 to 0.3 nm according to literature[8]. The large GPC is a result of CVD type of growth as mentioned in the lithium carbonate with ALD coating part, which is the consequence of condensation of water. In this case, the excess water mainly comes from the over exposure to the precursor of water. It can also be observed from the plot that there was a small amount of Al even the blank cerium nitrate after destruction, which proved the EDS result mentioned above (Table 3-5) that there were impurity or contamination contains Al on the blank cerium nitrate sample.

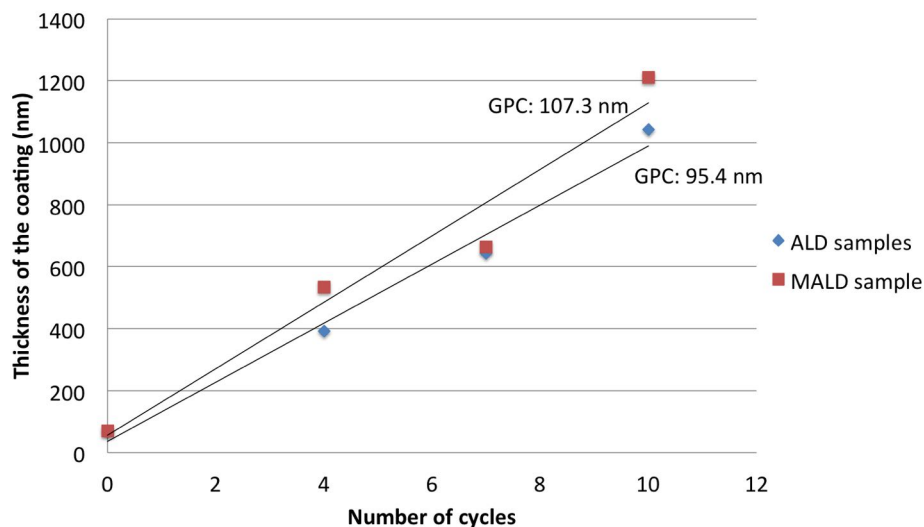


Figure 3-19: Calculated thickness of alumina film on cerium nitrate with 4, 7 and 10 cycles' ALD coating and MALD coating, respectively. precursors.

Cerium nitrate with MLD coating

MLD process was performed on the cerium nitrate for 5, 10 and 20 cycles as well, with crystal water and hydroxyl attached to the surface of the particles as active site where the coating was grown. The expected reaction and the structure of the coating are illustrated in Figure 3-20.

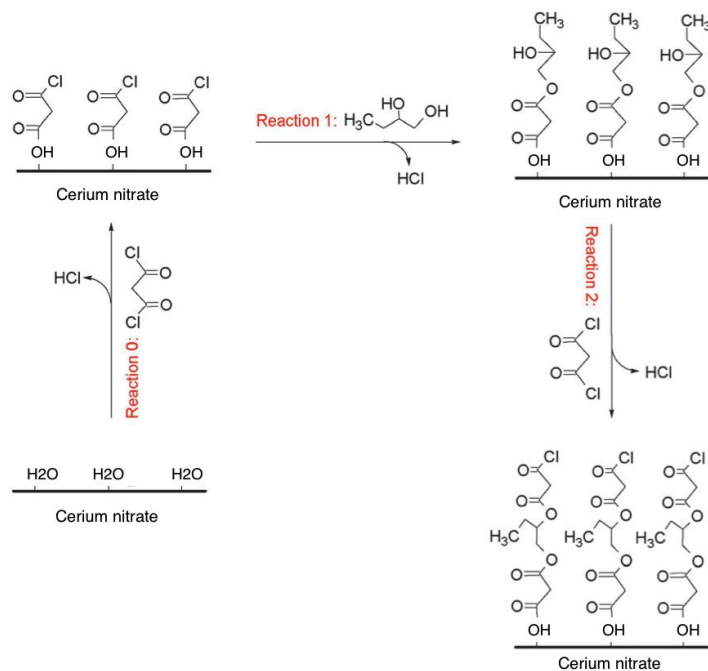


Figure 3-20: Illustration of the expected reaction in MLD process on cerium nitrate.

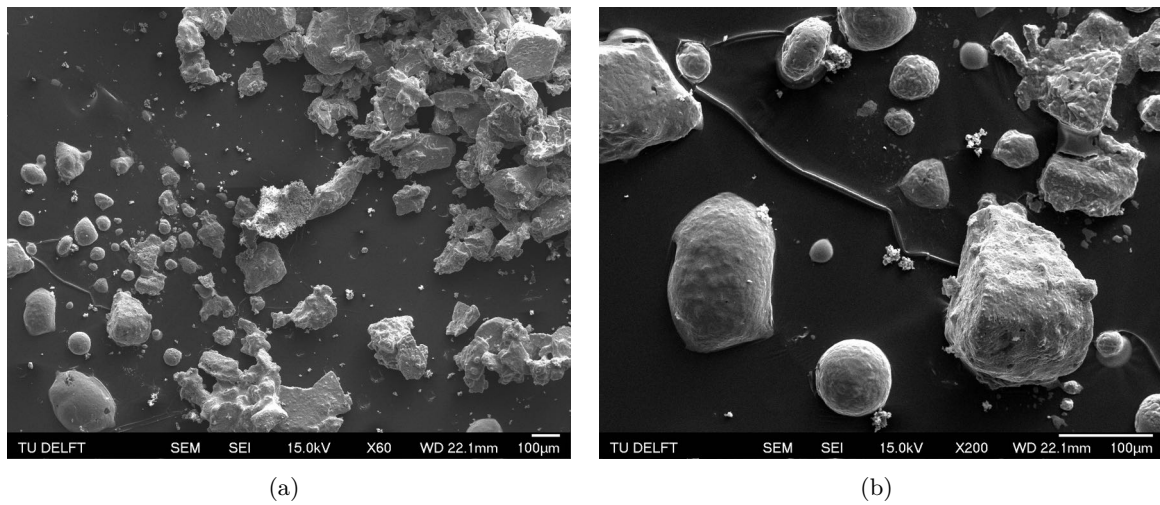


Figure 3-21: SEM images of the morphology of cerium nitrate after 20 cycles' MLD coating in (a) x60 and (b) 200.

SEM and EDS were performed with the focus on the cerium nitrate sample with 20 cycles of MLD. An example of the morphology is shown in Figure 3-21. Two morphologies can be distinguished in the cerium nitrate sample after 20 cycles' MLD process: the one with little difference compared to the $\text{Ce}(\text{NO}_3)_3$ without coating and the other one is the spherical particle. From the morphology, it can be inferred that the cerium nitrate particles are partly coated with the polymer chains which is the reaction product in the MLD process, forming a spherical shell in the raw material. Table 3-8 shows the EDS results of the elements contents in the spherical particles and the position of the points are indicated in Figure 3-22. More EDS results which shows the same trend on cerium nitrate MLD samples can be found in Appendix III. As it clearly shows, the content of Ce detected by EDS in the spherical particles, which is around 10 atom%, is less than the Ce detected in the blank cerium nitrate (Table 3-5). This could be an indication of the existence of the polymer shell.

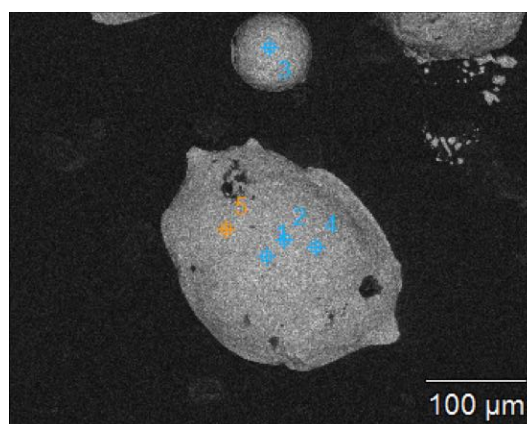


Figure 3-22: EDS point measurement on the spherical particles of $\text{Ce}(\text{NO}_3)_3$ after 20 cycles' MLD coating.

Table 3-8: EDS elemental concentration measurements results correspond to the position of points in the MLD 20 cerium nitrate spherical particles in Figure 3-22.

Point	N atom%	O atom%	Ce atom%
1	26.86	63.34	9.80
2	28.45	62.28	9.27
3	24.76	66.07	9.17
4	28.13	60.28	11.58
5	22.47	68.80	8.73

FTIR was also performed with $\text{Ce}(\text{NO}_3)_3$ MLD samples, with the peaks in the spectrum in the same position with cerium nitrate ALD samples (Figure 3-18). The bonds in the organic coating could not be observed. The reason could also be the amount of the coating was too less to be detected or the peaks from the coating are buried in the noise peaks correcting by the software in the background.

Leaching of cerium nitrate inhibitors encapsulated by ALD, MALD and MLD process were tested with ICP-OES. Figure 3-23 shows the result of ICP-OES with cerium nitrate samples dissolving in HCl and water. And Figure 3-24 shows the concentration of cerium ion from the $\text{Ce}(\text{OH})_3$ produced by dissolving the coated samples in alkali solution. The expected cerium ion concentration of complete leaching should be 140 mg/L in acid and neutral solution, 70 mg/L for the redissolving samples. It can be seen that all the concentrations of blank samples are lower than of the solution prepared. The reason could be that the dissolution was not complete since neither stirring nor increasing of temperature was performed on the solution prepared. From the two bar chart, it can be seen that though there is some variation on the detected concentration, the contents of cerium ion in the solution of encapsulated inhibitors do not show any reduced trend, indicating that leaching was not prevent by neither the alumina produced in ALD/MALD process nor the polymer shell produced in MLD process. This also further proves that the alumina shell was not really grown on the surface of cerium nitrate particle during the ALD process. As for the organic coating made by MLD, according to literature, 10 cycles' MLD coating with malonyl chloride and 1,2 butanediol as precursors, would dissolve in water in a timescale about 1000s[10]. Such an organic coating would only lead to a delayed release of the coated samples but not a non release of the bulk material. However, the leaching test done in this project is a yes or no test, in which the leaching of MLD samples is as expected. The effect of the organic shells can be tested further studying the kinetic of release via measuring concentration of Ce at different times of the dissolution.

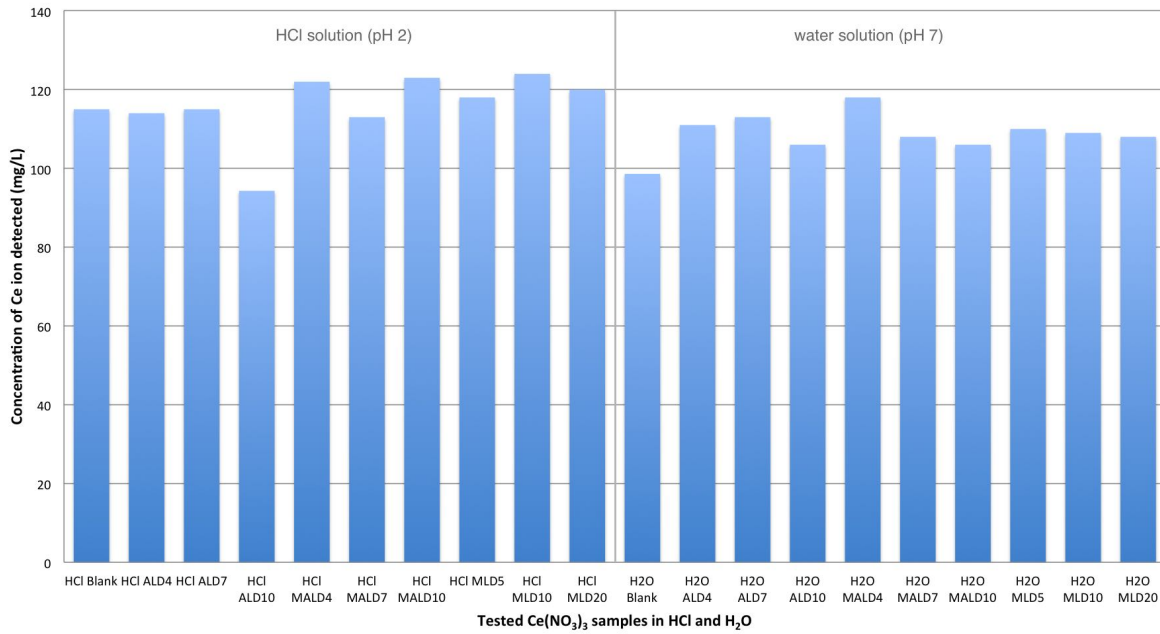


Figure 3-23: ICP-OES results in the leaching test of 4, 7 and 10 cycles' ALD, MALD and 5, 10 and 20 cycles' MLD coated cerium nitrate dissolved in HCl and neutral solution.

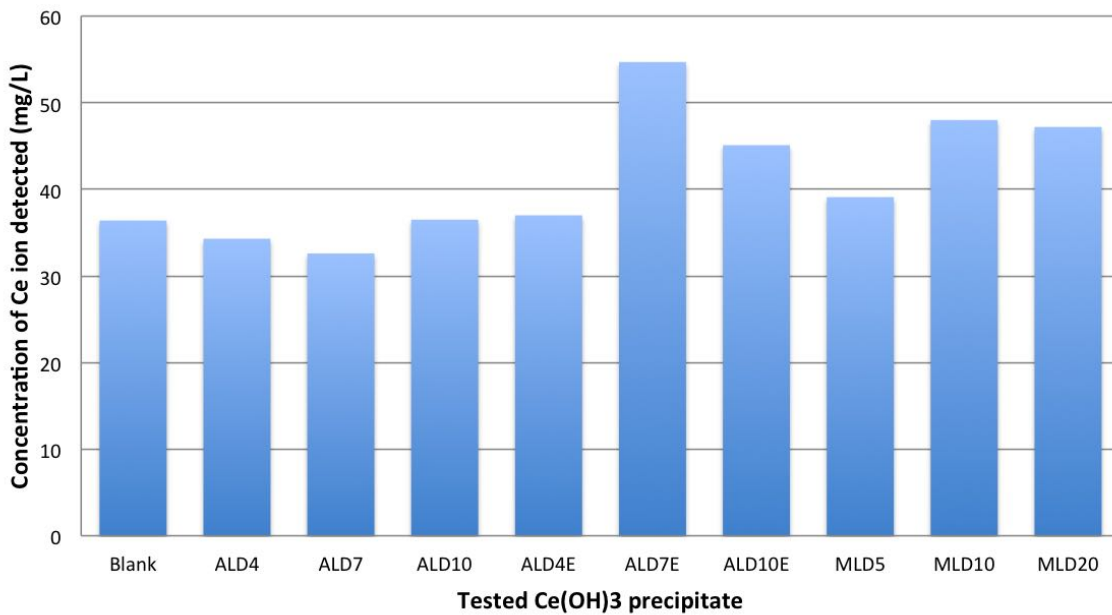
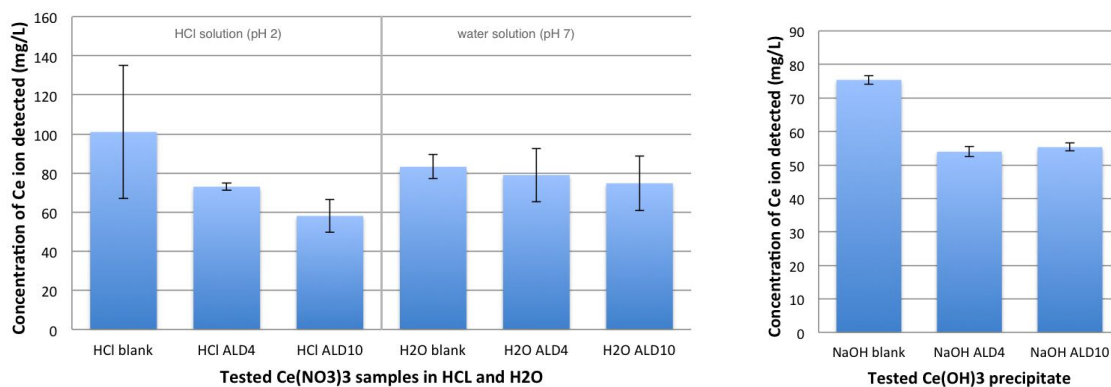


Figure 3-24: ICP-OES results in the leaching test of 4, 7 and 10 cycles' ALD, MALD and 5, 10 and 20 cycles' MLD coated cerium nitrate by redissolving the precipitate of Ce(OH)₃

To assure the reliability of the results, procedure of leaching test was repeated for the blank, ALD4 and ALD10 cerium nitrate samples, the result of which is shown in Figure 3-25. This



(a) Dissolving in acid and neutral solutions.

(b) Redissolving the precipitate of $\text{Ce}(\text{OH})_3$.

Figure 3-25: Second repetition ICP-OES result in the leaching test of ALD 4, ALD 10 and blank cerium nitrate samples.

time the immersion time for the solutions were 2 days less than the previous one. The expected cerium ion concentration of complete leaching should be 140 mg/L in acid and neutral solution, 105 mg/L for the redissolving samples. It can be seen from the bar chart that the detected cerium concentration was still lower than the expected value, which could be explained as the incomplete dissolution of the salt. Solutions were prepared without stirring or heating, as well as the less immersion time. However, focusing on the encapsulated inhibitor in neutral solutions, reduced dissolution cannot be observed still. Indeed, the leaching of cerium nitrate is not reduced by the encapsulation even in the neutral solution.

After dissolving the cerium nitrate ALD samples for several days, granular precipitate can be observed in the neutral solution. The precipitate should not come from the cerium nitrate as the solubility of cerium nitrate in water (176 g/100ml) is much larger than the concentration of the solution prepared. Then the precipitates were taken out by pipette and collected by evaporating the solution. When performing the SEM to the precipitate, small amount of hollow structure was found, the morphology of which is shown in Figure 3-26. This figure shows that there are some incomplete empty shells in the precipitates, which means that not only alumina particles mixed with small cerium nitrate particles were produced in the ALD process, but also shells for the cerium particles were made as well. EDS was also done on the empty shells, but the hollow structure trapped the electron from coming back to the detector, thus only 3 points was managed to be measured with relatively less noise peaks. The result are shown in Table 3-9. As it clearly shows, the content of Al in the shell is as high as larger than 10 atom%, which means that Al_2O_3 could be one of the ingredient of the shell. Ce is also detected as expect since the evaporation leads the precipitation of $\text{Ce}(\text{NO}_3)_3$. The incomplete coverage of the shell could be a reason for the all leaching of cerium nitrate in the leaching test. However, this kind of shell is in a small amount because in the EDS measurement on the ALD samples, most of the single cerium nitrate particles are without Al detected.

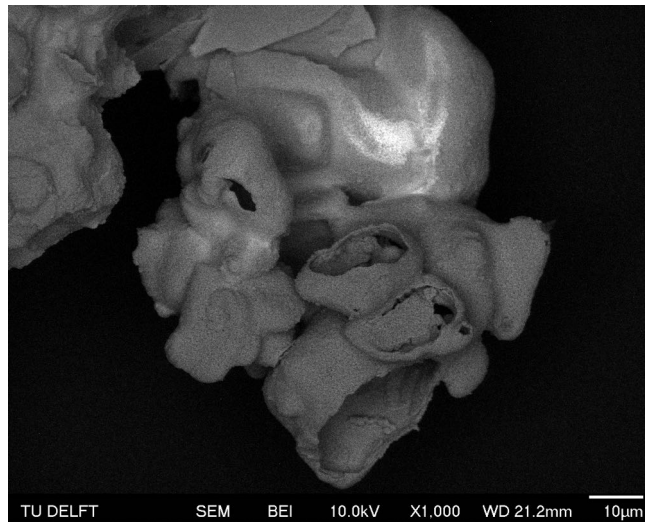


Figure 3-26: SEM image of the precipitate in the $\text{Ce}(\text{NO}_3)_3$ ALD samples in neutral solution.

Table 3-9: EDS elemental concentration measurements results correspond to the precipitate in the solution of $\text{Ce}(\text{NO}_3)_3$ ALD samples in neutral solution.

Point	C atom%	O atom%	Al atom%	Ce atom%
1	4.46	63.43	12.32	14.78
2		49.74	20.23	30.03
3	1.21	76.00	14.62	8.16

3-1-3 Encapsulations of 2-mercaptobenzothiazole (2-MBT)

Characterization of the encapsulation of 2-MBT will be discussed in the following part. Corrosion inhibitor of 2-MBT was encapsulated by 5, 10 and 20 cycles' of MLD process. SEM and EDS analysis were focused on the MLD20 sample. FTIR and leaching test were carried out on all the coated samples.

2-MBT after grinding

2-MBT was grinded manually to reduce the size. Figure 3-27 show the morphology of the raw material after grinding. As it shows, the particle size of 2-MBT after grinding varies significantly, and there are small particle attaching in the surface of big particles. The large particles after grinding can be 10s of μm and the small particles can be less than 1 μm . EDS was performed on blank 2-MBT as reference, and the position of the points are indicated in Figure 3-28 and the results are shown in Table 3-10. The concentration detected is about 50 atom% N and 50 % O with the peaks of carbon being cut off. There is a point with a very high content of S(point 3), the reason of which remains unknown. It may be a detection error.

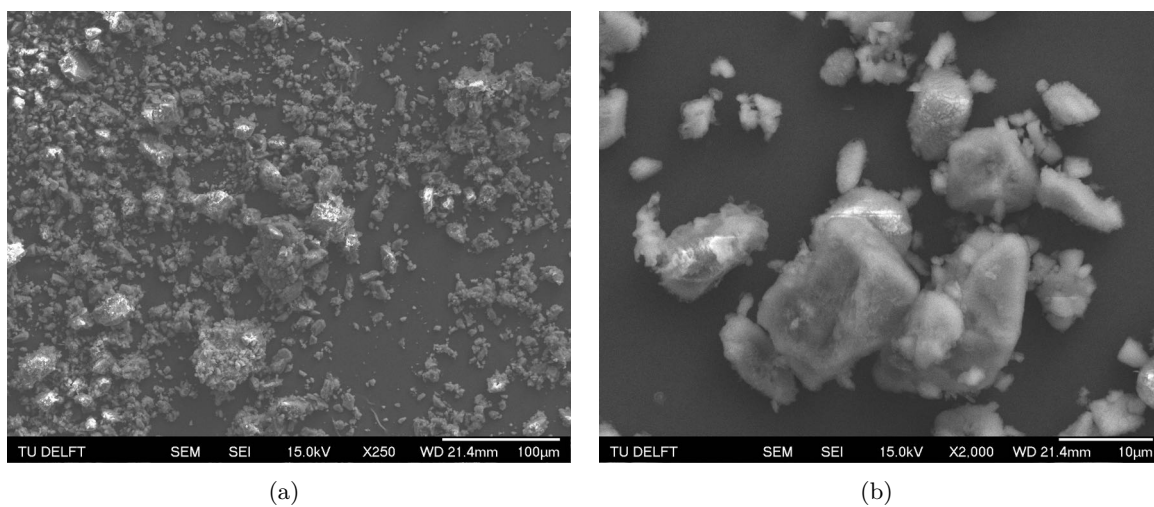


Figure 3-27: SEM images of the morphology of blank 2-MBT in (a) x250 and (b) x2000.

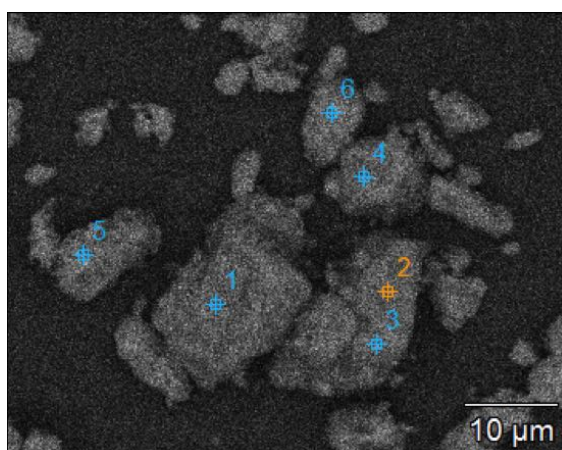


Figure 3-28: EDS point measurements on the blank 2-MBT powder with position of the points indicated.

Table 3-10: EDS elemental concentration measurements results of the blank 2-MBT powder correspond to the position of points indicated in Figure 3-28.

Point	N atom%	S atom%
1	49.42	50.58
2	43.88	56.12
3	7.33	92.67
4	42.61	57.39
5	48.28	51.72

2-MBT with MLD coating

MLD process was performed on 2-MBT. With the exocyclic sulfur being the active site for the thiol form of 2-MBT, the reactions and structure of coating are illustrate in Figure 3-29. For the thion structure, the active site could be the amine with the same reaction and structure of coating.

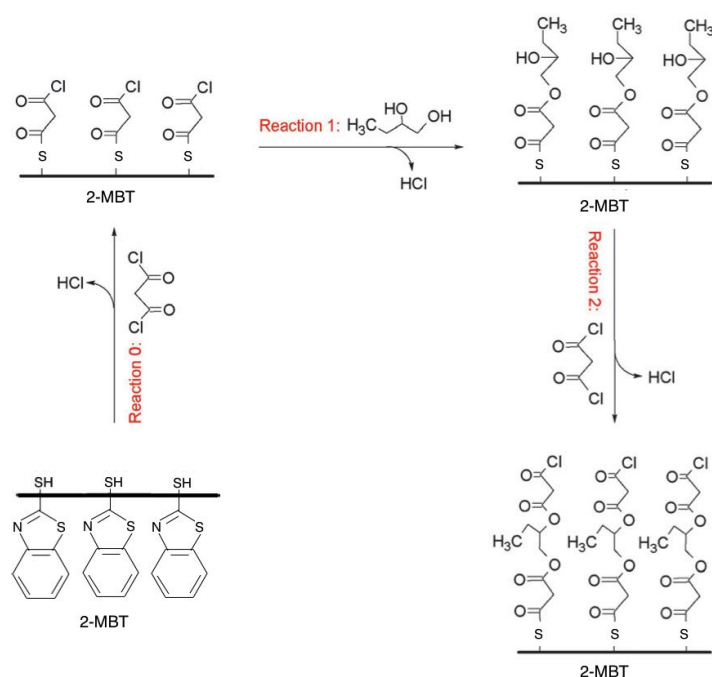


Figure 3-29: Illustration of the expected reactions in MLD process on 2-MBT.

Figure 3-30 shows the morphologies of 2-MBT sample after 20 cycles' MLD process. As shown clearly, the general particle size increased a lot and the surface of a single particle becomes smoother though still with small particles attached in the surface. This could be caused by the agglomeration during the fluidization and there are more than one particle in a shell after coating. Also, the N_2 gas flow may also take the small particle away during the MLD process, which has been mentioned before. Table 3-11 shows the result of points measurement with EDS and the position of the points are indicated in Figure 3-31. It shows clearly that element of O was detected with the amount of 10 atom% in the 2-MBT MLD20 samples, which can be a proof of the existence of the polymer shell made during the MLD process.

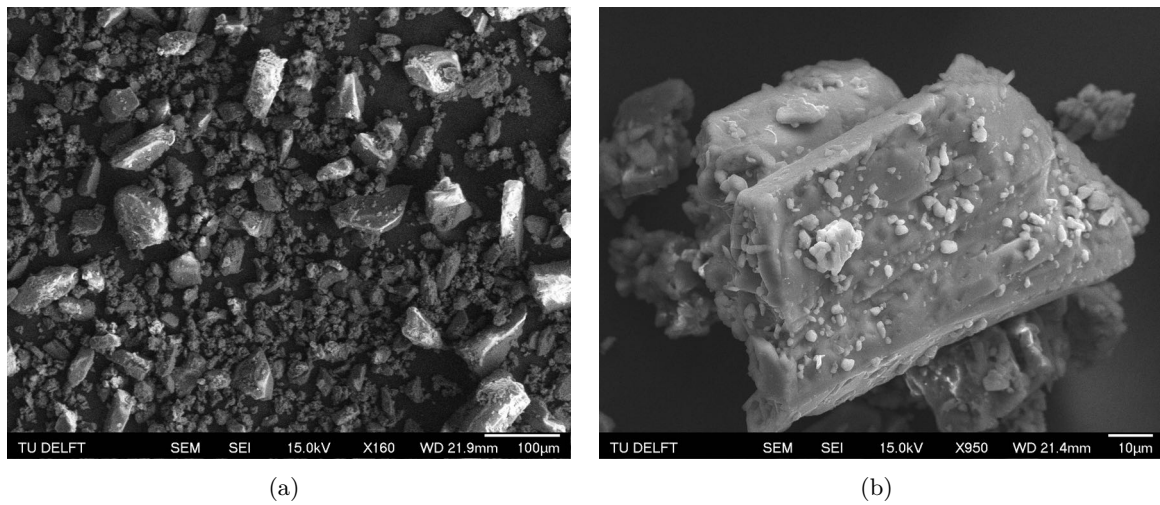


Figure 3-30: SEM images of the morphology of 2-MBT after 20 cycles' MLD in (a) x160 and (b) x950.

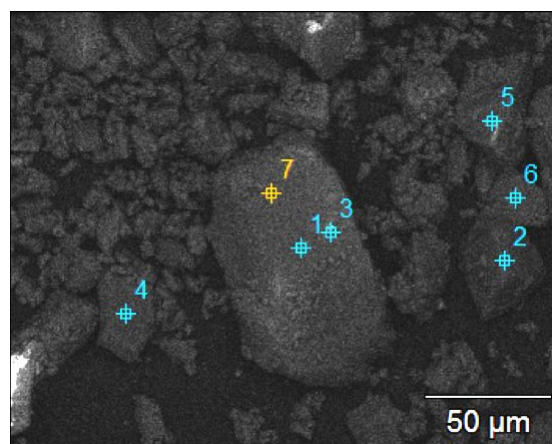


Figure 3-31: EDS point measurements on the MLD 20 2-MBT samples with position of the points indicated.

Table 3-11: EDS elemental concentration measurements results of the 20 cycles' MLD 2-MBT correspond to the position of points indicated in Figure 3-31.

Point	N atom%	O atom%	S atom%
1	42.24	9.67	48.10
2	53.43	19.27	27.29
3	49.91	12.04	38.04
4	61.71	7.76	30.54
5	34.90	16.12	48.99
6	26.22	10.63	63.15
7	48.67	9.35	41.98

ATR-FTIR was also performed to further verify the coating of the 2-MBT particles. The ATR mode is highly surface-sensitive, with which the information of the chemical bond in the coating can be observed. Figure 3-32 shows the ATR-FTIR spectrum of pure 2-MBT powder as a reference. In the spectrum, a broad band system with six medium intense bands (peaks) at 3011, 3077, 3038, 2961, 2892 and 2838 cm^{-1} , can be observed. Some literature[61][18] explained these bands due to NH stretching vibrations, which are shifted towards lower wavenumber due to hydrogen bonding in the dimer form of 2-MBT. The band observed at 1596 cm^{-1} is ascribed to C=C stretching mode[18][62]. The intense bands observed at 1496, 1425 and 1245 cm^{-1} are associated to the vibration of the C-N-H group[18]. The sharp peaks at 1283 and 1320 cm^{-1} are from the C-N vibrations and the intense band observed at 1456 cm^{-1} is attributed to CC and CN stretching and CH bending vibrations[18]. The strong bands in a group at 1076, 1034 and 1023 cm^{-1} are commonly ascribed to N-C=S group vibrations in addition to CC and CH bending vibrations[18]. The band at 750 cm^{-1} is due to the four contiguous H atoms on benzene ring outward rocking vibration. In addition, the strong band at 706 cm^{-1} is attributed to the vibration of C-S[62].

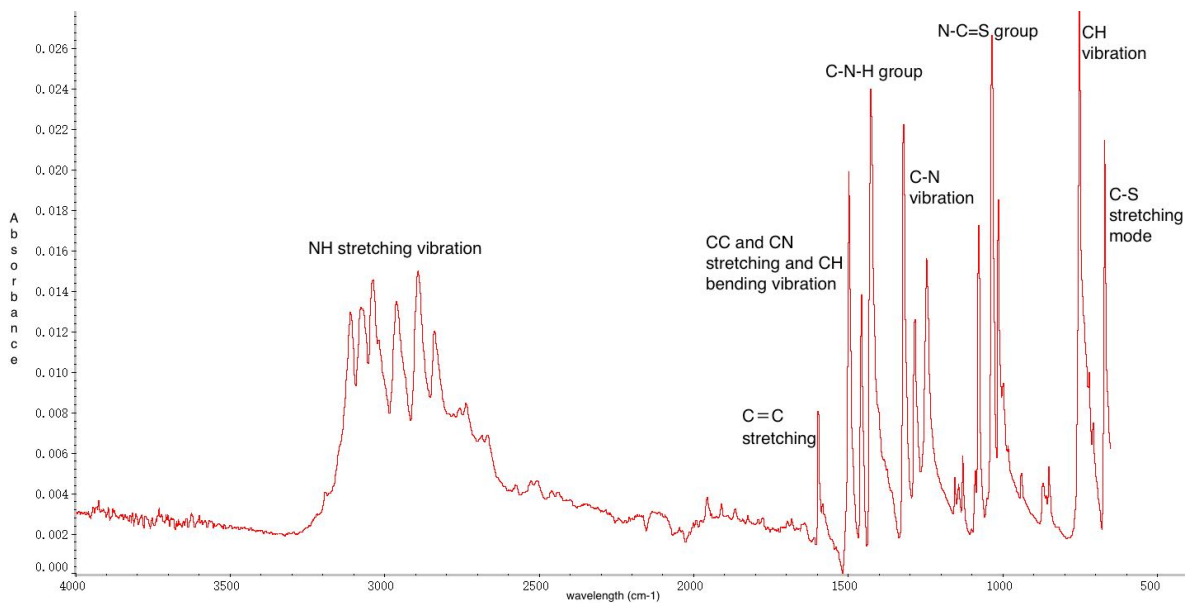


Figure 3-32: FTIR spectrum of blank 2-MBT.

Figure 3-33 shows the ATR-FTIR spectrum of coated 2-MBT samples with 5, 10 and 20 cycles' MLD. A distinct peak can be observed in the position of 1713 cm^{-1} , which does not appear in the blank 2-MBT sample. This peak corresponds to the stretching of [-COO-] group. Increase in the absorbance peak gives an indication of the increase in the coating thickness with the number of cycles. It can be seen that peaks from 2-MBT still exist in the coated samples, which should be because of the light went through the coating and penetrate into the bulk material.

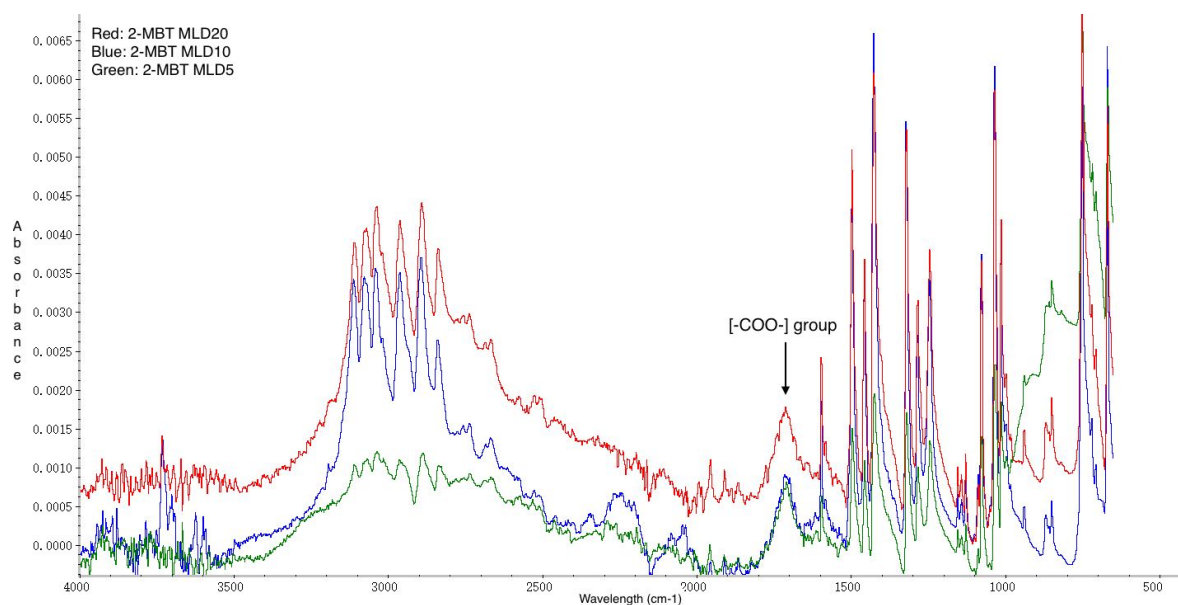


Figure 3-33: FTIR spectrum of 2-MBT after 5, 10 and 20 cycle' MLD coating.

Leaching test was performed on coated 2-MBT with 5, 10 and 20 cycles' MLD process by UV-vis spectrophotometer. Figure 3-34 shows the UV-vis spectra of the solution with 2-MBT MLD samples dissolved. It can be seen that 2-MBT was released in all the samples tested after several days dissolving, no matter how many cycles of MLD had been performed. This result seems to be as expected according to the results from the research of encapsulation of protein by Vasudevan[10], in which the same shell was made and the leaching in water was within a timescale of 1000s. The kinetic of the release is also suggested to be carried out for the MLD 2-MBT samples to study further about the effect of the organic coating by detecting the absorbency of light at different time to indicate concentration of 2-MBT at different time of the dissolution. From the absorption peaks in the spectrum, it is interesting to observe that the peaks of the 2-MBT in the alkali NaOH solution (pH 12) are shifted slightly towards a lower wavelength. This is because of the thion and thiol tautomeric forms of 2-MBT in equilibrium in the pH range 2-12 which show a marginal change in molar absorptivity with change in the pH of the solution[18]. According to literature, the thiol form can interact with OH⁻ and forms an anion in the alkaline solution[63]. The spectral changes are reversible depending on the pH of the solution. The absorptivities of thiol and thion species of 2-MBT are quoted in Table 3-12.

Table 3-12: Absorptivity of 2-MBT in acidic and alkaline medium.

Medium	λ_{max}
Acid medium pH 2 to 6	230 nm and 320 nm
Alkaline medium pH 8 to 12	235 nm and 315 nm

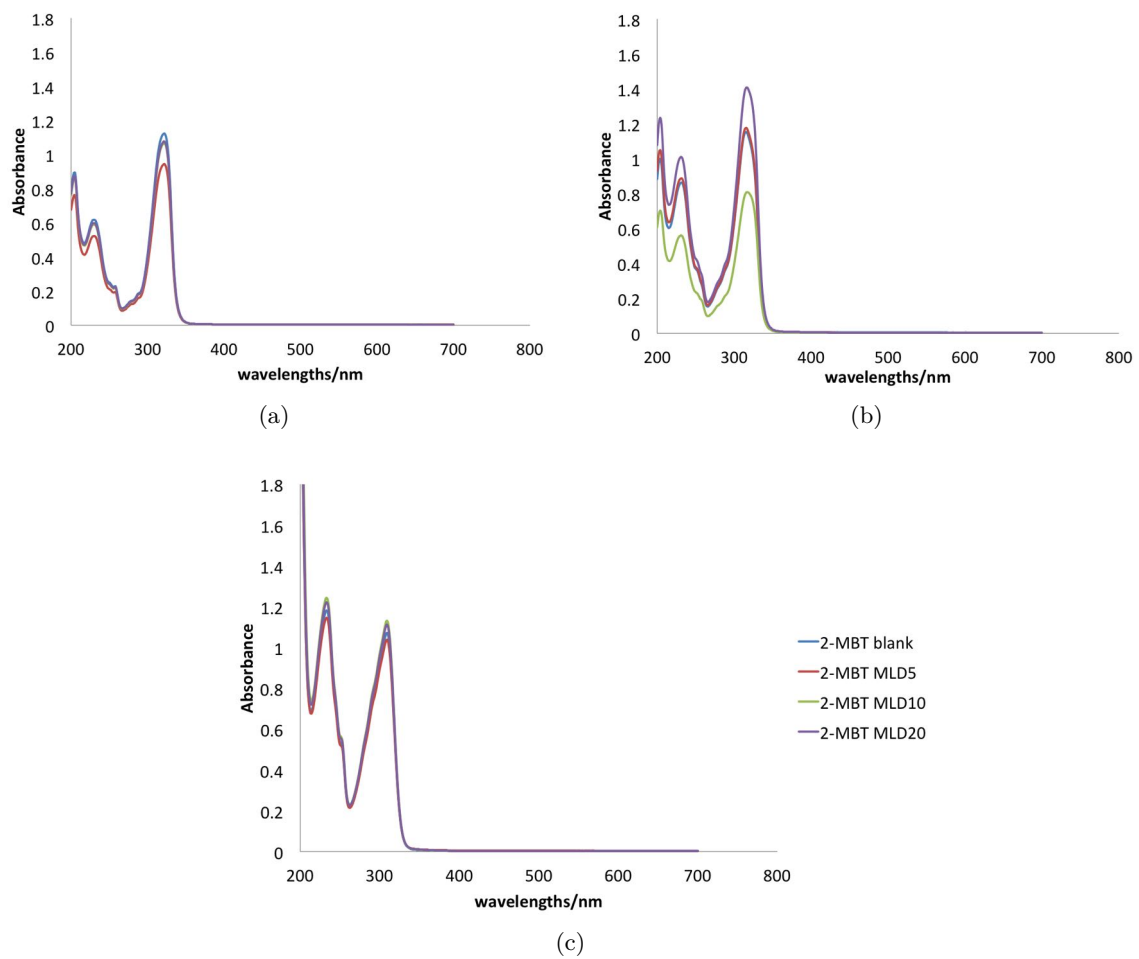


Figure 3-34: UV-vis absorption spectra of 2-MBT (a) in acid solution (b) in neutral solution and (c) in alkali solution.

3-2 Characterization of the anti-corrosion performance

After the characterization of encapsulation, the capsules were doped into epoxy coats and applied on AA2024-T3 sheet. EIS measurements were performed on the scratched samples prepared to test the corrosion inhibition performance. According to the results of the leaching test discussed above, only capsules with highest cycles of encapsulation were chosen to be doped. Therefore, 3 different type of samples were prepared, namely blank epoxy coating without inhibitor doped, blank inhibitor-doped coating and encapsulated inhibitor doped coating. As mentioned in Chapter 2, defective samples were scribed manually by a knife in order to study the smart release of inhibitor and inhibition efficiency. Impedance of bare metal was also measured as a reference.

3-2-1 EIS results of encapsulated lithium carbonate doped coating

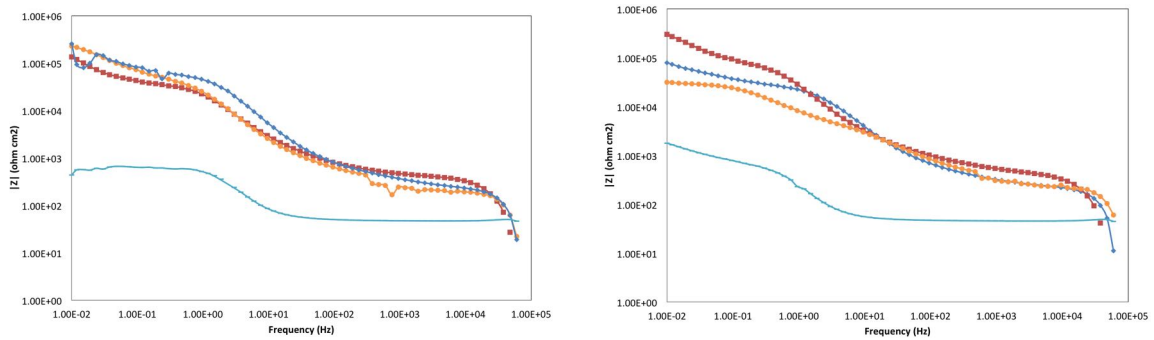
Figure 3-35 shows the scratched regions after 4 days immersion. In the blank coating sample, accumulation of corrosion product (white) can be clearly observed in the scribed region, while the scribed region looks still clean after 4 days' immersion in the Li_2CO_3 doped coating.

Figure 3-36 show the change of the impedance with time of immersion. The bare metal without any coating and the blank coating with scratch were tested for reference. It can be seen that all the coating, though with scratches, show a higher value of impedance, indicating the protection by the epoxy coating. For the bare metal (light blue), in the low frequency part, the changing from the plateau to linear line could be explained as the formation of corrosion product in the surface, which slows down the corrosion rate. For the blank coating (dark blue), the decrease of the impedance value and the transform from linear to flatter plateau in the low frequency part give indications about the corrosion activity in the scribed region. For the blank lithium carbonate doped coating (orange), the impedance first decrease about 1 order of magnitude from 3 hours to 1 day after immersion and than increase about half order of of magnitude in the fourth day. The decrease could be explained as the delay of the inhibition due to diffusion of the inhibitor from the coating to the defect as well as the time for the formation of protective layer. However, the impedance of the coating doped with blank lithium carbonate shows a increased value and a nearly linear part in the low frequency in the fourth day which is an indication of the inhibition. For the ALD lithium carbonate doped coating (red), from the continued growth of the impedance value, the inhibition and healing effect of the inhibitor can be proved. An interesting phenomenon is that the alumina coated inhibitor doped coating shows a quicker respond in healing of the defect. This could be due to the mechanism of inhibition by lithium salts. The inhibition is achieved by the formation of lithium-aluminum hydroxide-carbonatehydrate to reduce the corrosion current density. Although the leaching of core material from the shell may slow down the diffusion the inhibitor, the dissolved shell may increase the concentration of Al ion in the area of the defect, speeding up the protection process. After 4 days, the Li_2CO_3 ALD sample shows almost pure capacitive behavior at low frequencies demonstrating excellent protective properties even after long immersion time. A healing effect can be proved by this sample.



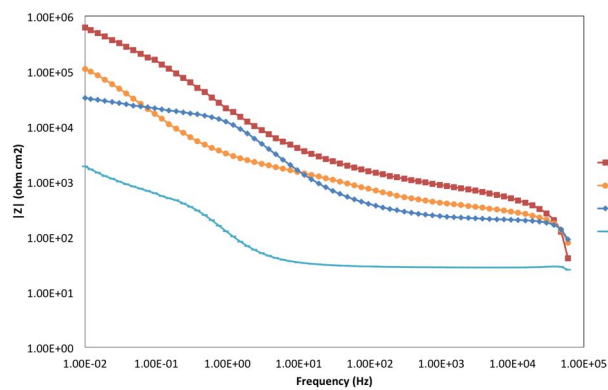
(a) ALD 10 Li_2CO_3 doped coating. (b) Blank Li_2CO_3 doped coating. (c) Blank coating without inhibitor.

Figure 3-35: Optical microscopy images of the scribed coating after 4 days' immersion in 0.05 M NaCl solution.



(a) Three hours after immersion.

(b) One day after immersion.



(c) Four days after immersion.

Figure 3-36: Bode plot from EIS measurement of the defect coated lithium carbonate system after (a) 3 hours (b) 1 day and (c) 4 days immersion.

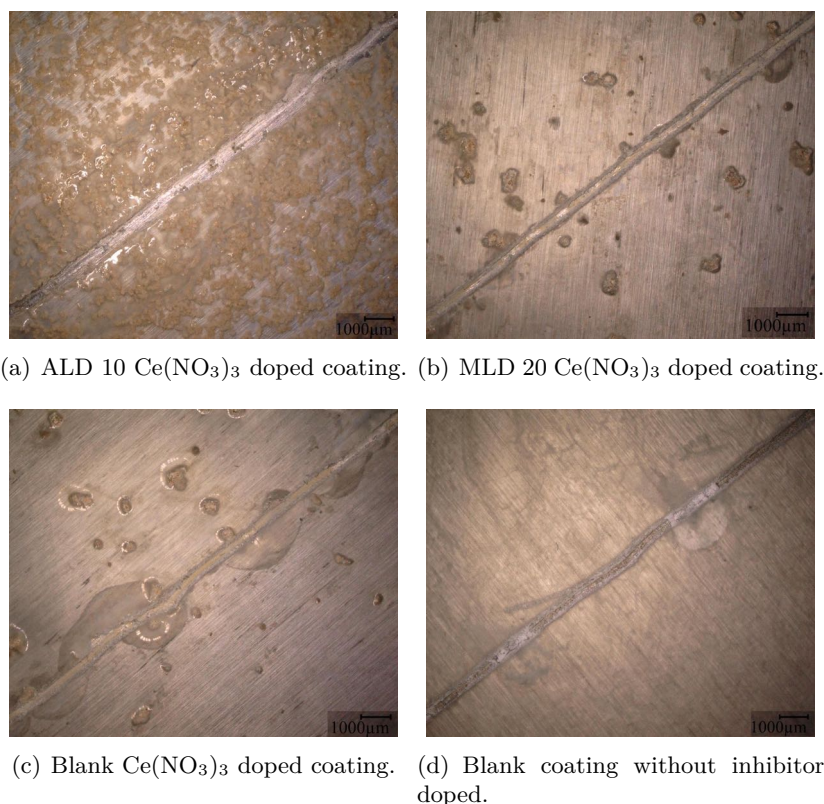


Figure 3-37: Optical microscopy images of the scribed coating after 4 days' immersion in 0.05 M NaCl solution.

3-2-2 EIS results of encapsulated cerium nitrate doped coating

Figure 3-37 shows the scratched regions after 4 days immersion. The scribed region of the inhibitor doped coatings appeared still clean after 4 days' immersion. The white corrosion product was not clearly observed.

Figure 3-38 shows the change of the impedance with time of immersion. All of the scribed coating show a higher impedance value than the bare metal, indicating the protection provided by the epoxy. However, the impedance of ALD cerium nitrate doped coating (red line) is much lower than the blank and MLD cerium nitrate doped sample, which means a worst protection after the scratch was made. This could also be blamed to the alumina inside the coating. The mixture of large amount of alumina particles decreased the adhesive property of the coating dramatically, leading to the peeling off the coating in surrounding when making the scratch. This can also be proved by the width of scratch in Figure3-37(a). The width of the scratch in ALD cerium nitrate doped sample, which was about $500 \mu\text{m}$, was much wider than the other sample(around $200 \mu\text{m}$), which was because of peeling off of the coating when making the scratch. However, slightly increase of the impedance can be observed, this may result from either the inhibition of the cerium nitrate in the coating or the corrosion production in the scratch. For the blank cerium nitrate (orange): the impedance first increased slightly in the first day and decreased about half an order of magnitude in the following 3 days. A slightly weak healing effect can be observed compare to the blank coating sample in the first day. But

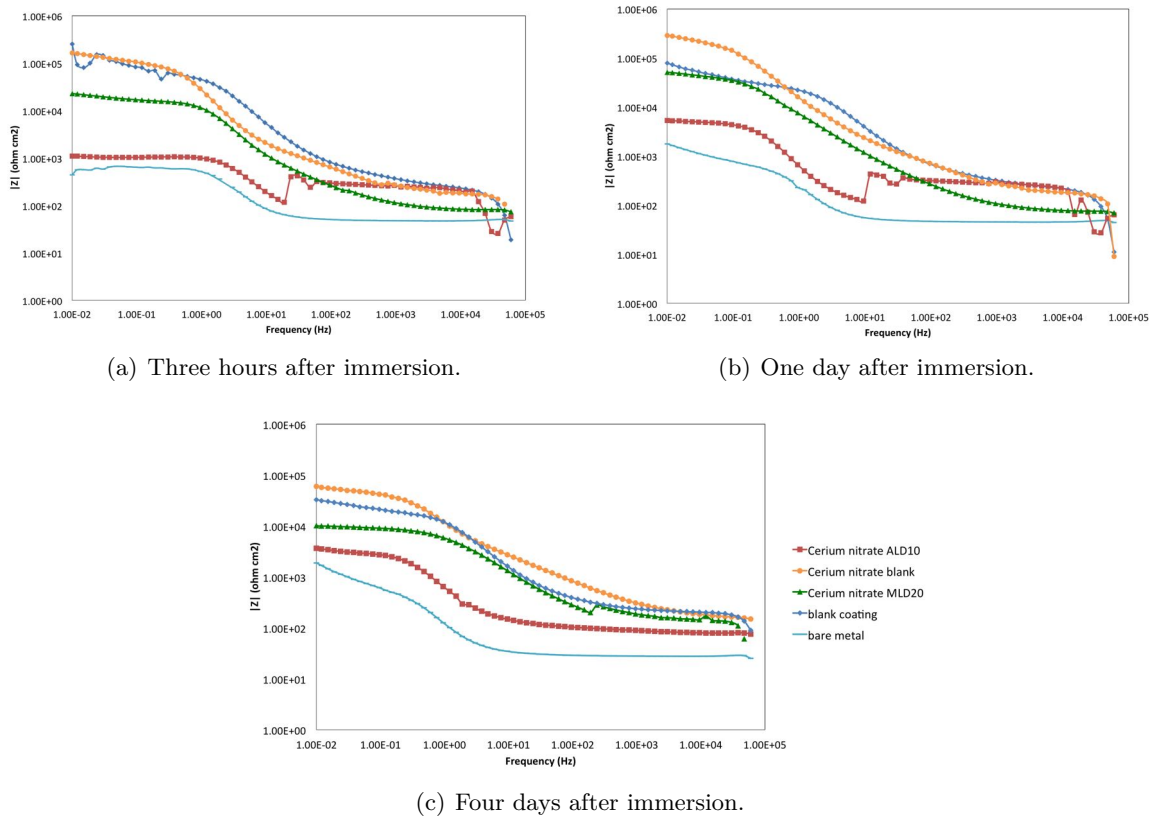
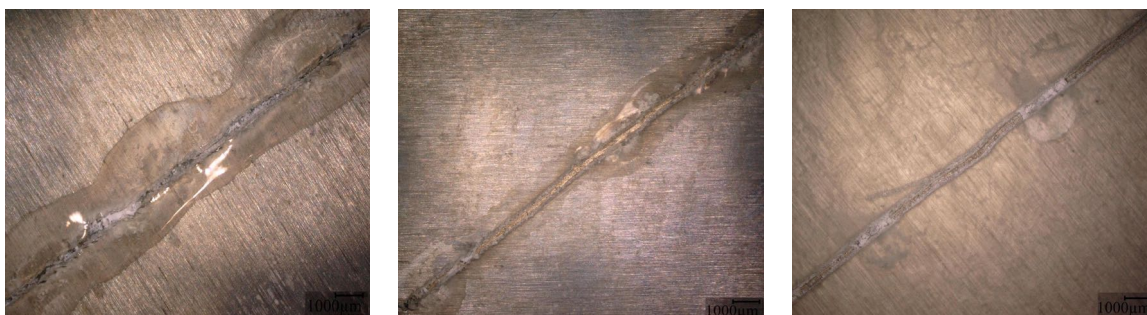


Figure 3-38: Bode plot from EIS measurement of the defect coated cerium nitrate system after (a) 3 hours (b) 1 day and (c) 4 days immersion.

the value of impedance is not much higher than the blank sample, which could be caused by decreasing of the effective thickness of the coating resulting from the large size of the particle doped. There is no obvious changing in the value of impedance of MLD cerium nitrate doped coating (green line). A slightly increase in the first day and more than half order of magnitude decrease in the following 3 days can be observed. The behavior seems exactly the same with the blank cerium nitrate. This can be explained as the fast lost of the MLD shell. But the impedance of MLD coated sample is even lower than the blank sample. It could be that the organic coating reacted with or dissolved in the polymer matrix, which could decrease the adhesive property of the coating to the substrate. The decreasing of the adhesive property make the coating peeled off in surround of the scratch. However, the plateau of impedance in the low frequency region always exist in all the cerium nitrate sample, which means the inhibitors doped in the coating do not provide the system a good protective inhibition.

3-2-3 EIS results of encapsulated 2-MBT doped coating

Figure 3-39 shows the scratched regions after 4 days immersion. As the figure shows, the scribed region of the MLD and blank 2-MBT doped coatings turn to a bit black. The nigrescence in the scribed region could be attribute to the mechanism of the inhibition of 2-MBT, during which sulfide is formed in the region where corrosion activity happens. Severe peeling

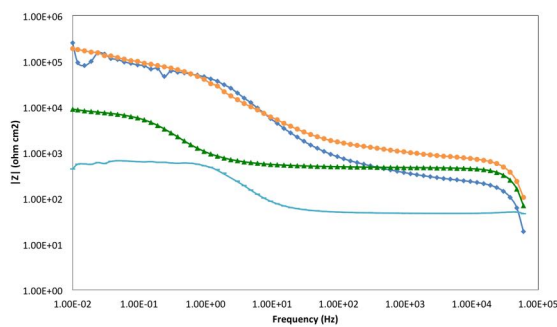


(a) MLD 20 2-MBT doped coating. (b) Blank 2-MBT doped coating. (c) Blank coating without inhibitor.

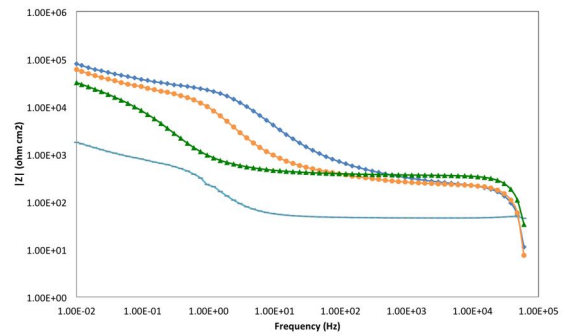
Figure 3-39: Optical microscopy images of the scribed coating after 4 days' immersion in 0.05 M NaCl solution.

off can also be observed in the MLD 2-MBT doped coating.

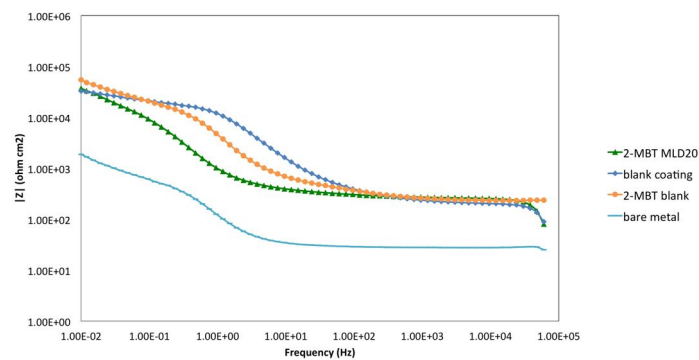
Figure 3-40 shows the change of the impedance with time of immersion. It can be seen that the 2-MBT doped in the coating do not show any inhibition effect, and the impedance of MLD 2-MBT doped coating is even lower than the blank coating. The impedance of MLD 2mbt sample (green line) starts in a quite low value (10^4 ohm cm^2), the same as the MLD cerium nitrate sample. The polymer shell may cause influence to the adhesive property of the coating to the AA2024 substrate. However, the impedance of MLD 2-MBT sample increased more than half an order of magnitude, and the plateau in the low frequency has the tendency to changing into linear, indicating the 2-MBT played a role of inhibition. The blank 2-MBT doped coating (orange line) does not show big difference to the blank coating sample, the reason behind still need to be studied. However, it can be seen from the literature that the corrosion inhibition of 2-MBT is good when kept in chloride solution or dope together with other inhibitors as a synergism effect. Studies of the inhibition behavior of 2-MBT doped in organic coating could be done in the future.



(a) Three hours after immersion.



(b) One day after immersion.



(c) Four days after immersion.

Figure 3-40: Bode plot from EIS measurement of the defect coated 2-MBT system after (a) 3 hours (b) 1 day and (c) 4 days immersion.

3-3 Overall discussion

Till here, the coverage of coating after ALD and MLD process, estimation of thickness of Al_2O_3 obtained through ALD process, leaching of the inhibitors from shell material and the anticorrosion performance of the inhibitor doped scratched coating have been discussed. This section will describe a overall picture of the results and discussions.

From the results of SEM and EDS, inhibitor of lithium carbonate encapsulated via ALD coating showed a good coverage according to the compositional change in the surface of the inhibitor particle. Cross-sectional images of layered structure of the coated sample are still needed to be done in the future work to verify the full coverage of the coating since layered structure was not observed with backscatter electron images due to the resolution of SEM and preparation of the sample embedding. The coated 2-MBT also showed a good coverage after MLD coating according to the compositional change in the surface and the appearance of [-COO-] bond which was not in the raw material. Cerium nitrate was coated via MLD coating but the Al_2O_3 produced in the ALD process did not make shells for the cerium nitrate particles but formed nano particles depositing on the surface according to the compositional information obtained by EDS. The encapsulation of cerium nitrate via ALD process still needs further study, in which ozone is suggested to be an alternative for water as one of the precursors in the reaction to reduce the water condensation.

From the results of ICP-OES by destructing the Al_2O_3 coated samples in the strong acid to estimate the thickness of Al_2O_3 , it can be seen that the growths of the Al_2O_3 in the ALD processes on both lithium carbonate and cerium nitrate were in a higher rate than expected, which was a result from the residual CVD component in ALD process. For the ALD coating on lithium carbonate, the growth per cycle was about 4 nm, while for the ALD process on cerium nitrate, the growth per cycle increased dramatically to around 100 nm. The large GPC in cerium nitrate ALD process could be explained as a result of water condensation from both crystal water inside the raw material, excess dosing of precursor as well as the moisture in the FBR since the reaction was carried out at 50°C. The thickness of alumina on lithium carbonate particles obtained via ICP-OES was thinner than the result of compositional results from EDS in cross-sectional SEM images, which could be due to the incomplete dissolution of coated particles in the acid before ICP-OES test.

In the results of leaching test, a reduced leaching of inhibitor in neutral solution was only observed in the case of encapsulated lithium nitrate but the effect was not as obvious as expected. Ideally, non-leaching or little leaching should be observed in ALD encapsulated inhibitor in neutral solution. Two possible explanation were given: this was because of the insufficient coverage of Al_2O_3 coating or the Al_2O_3 coating was not dense and thick enough to prevent water penetrating. Further work still need to be studied by estimating the number of active sites in the surface of inhibitor before ALD/MLD process, increasing the reactor temperature and number of cycles in the ALD/MLD process to possibly solve this problem. Although the cerium nitrate and 2-MBT were covered by organic coating after MLD process, reduced leaching was not observed. This was explained as the insufficient stability of the organic coating in solutions. Kinetic leaching tests by measuring concentration of inhibitors at different time of the dissolution were recommended to be carried out to further study the function of the organic coating. The leaching of cerium nitrate was not reduced after ALD coating. After the dissolution for several days, white precipitates could still be observed in the

bottom of the neutral solutions. The precipitates should be the alumina particles depositing in the surface of cerium nitrate particles and incomplete alumina shells produced in the ALD process, and this was in agreement with the SEM and EDS results mentioned above.

In the results of EIS, the scratched coating doped with ALD encapsulated lithium carbonate showed the best healing effect for the AA2024 substrate, which was in agreement with the result in the characterization of the coating and leaching. The Al_2O_3 in the lithium carbonate not only acted as a protective shell for the inhibitor but also favored the mechanism of inhibition. The encapsulated inhibitors via MLD process, namely MLD 2-MBT and MLD cerium nitrate showed even lower impedance than the blank coating without inhibitors which could be a result of the decrease of adhesion properties of the coating possibly generated by the reaction between the organic coating and the epoxy matrix. The scratched coating doped with encapsulated cerium nitrate via ALD process showed the lowest value of impedance among all the immersed scratched coating samples. The large amount of Al_2O_3 particles generated from ALD process decreased the adhesion property of the coating dramatically, causing the peeling off of the coating when making the scratch and blistering during the immersion. Scanning vibrating electrode technique (SVET) would be recommended to be performed to map and quantify the local electrochemical and corrosion processes as a function of time, with which local anodic and cathodic activities can be monitored to further monitor the healing effect. Optimization of the formulation of epoxy correspond to different kind of shells and bulk inhibitors could be recommended to be carried out to avoid reducing of adhesion and reactions between coating and the encapsulations.

Overall, the encapsulation method of ALD/MLD for corrosion inhibitor put forward in this thesis shows some potential especially in the case of encapsulation of lithium carbonate via ALD process, but the smart release effect triggered by pH was not significant as expected. Further work is worthy doing to improve the quality of the encapsulations and to further verify the feasibility of this novel encapsulation method of ALD/MLD for corrosion inhibitors.

Conclusions and recommendations

4-1 Conclusions

The goal of this thesis is to explore the feasibility of novel encapsulation methods to achieve a smart release of coated inhibitors. To this end, three chromate free inhibitors, namely lithium carbonate, cerium nitrate and 2-mercaptobenzothiazole were encapsulated with two chemical methods, namely atomic layer deposition and molecular layer deposition.

For the encapsulated lithium carbonate by ALD, the existence of the coating was proved by SEM and EDS analysis. However, since the trial of taking images of layered structure with backscatter electron in the cross section of coated particles did not succeed, the full coverage of the coating was not proved. Thickness of the coating was estimated with the mass fraction of Al in the coated sample. It was found that growth per cycle was about 4 nm, which was a result from the residual CVD component in ALD process. From the EDS results on the edge of cross sectional sample, the thickness could be even thicker than the estimation. In the leaching test, a slightly reduced release was found with the coated sample in neutral solution but the effect was not obvious. A healing effect can be observed in the EIS test with inhibitor doped scribed epoxy coating for both encapsulated and un-encapsulated inhibitor. The encapsulated lithium carbonated doped coating show a better anticorrosion property, indicating method of ALD being a feasible way of encapsulation.

For the encapsulation of cerium nitrate by ALD and MLD, the inhibitor was not well coated by ALD process according to the results of SEM and EDS analysis. The growth per cycle of Al_2O_3 was increased dramatically to around 100 nm in this case, which could be results of the water condensation from both crystal water inside the raw material and the precursor dosed since the reaction was carried out at 50°C. Inhibitors was coated with organic coating in MLD process due to the result of SEM and EDS analysis. In the leaching test, reduced release of the coated samples was not observed in both the case of MLD and ALD coated samples. A even worse anticorrosion property was found in the EIS test with coated inhibitor doped defective coating because of the reduced adhesion due to the addition of inhibitor.

For the encapsulation of 2-MBT, organic coating produced in the MLD process was proved by both EDS analysis and ATR-FTIR spectrum. It was found in the leaching test that the

organic coating was not stable enough to prevent/reduce the release of inhibitor even in the neutral solution. Inhibition effect was not observed in the EIS test with both encapsulated and non-encapsulated doped coating. Severe blistering and delamination can be observed after immersion for the encapsulated 2-MBT doped defective coating, indicating the negatively influences of the adhesion and barrier properties result from the organic coating.

To sum it all up, the application of novel encapsulation method of ALD/MLD for corrosion inhibitors shows potential to some extent. In this thesis, the encapsulation of lithium carbonate shows a good effect in coating, leaching and inhibition aspect. The encapsulation method of MLD for 2-MBT also shows a good coverage, but with a reduced adhesion property when doped into coating. Though neither ALD nor MLD encapsulation method shows good result in the case of cerium nitrate encapsulation, it could be improved by further study in which ozone can be used as one of the precursors instead of water. Future work is worth doing to further verify the feasibility of this novel encapsulation method of ALD/MLD for corrosion inhibitor.

4-2 Recommendations

For the continuation of research, following recommendations should be considered to have further development of ALD and MLD as encapsulation methods for corrosion inhibitors.

For the raw material, the inhibitor is suggested to be mechanically controlled in a uniform size to get a better fluidization behavior in the FBR and a more uniform coating after ALD and MLD process. Thermogravimetric analysis (TGA) is recommended to be performed to study dehydroxylation and to estimate the number of OH groups on the surface, as enough OH group, being the active site for the growth of coating, is the prerequisites for the full coverage of coating. Since the moisture is an important influential factor to the growth per cycle of the coating, temperature sensitive powder such as cerium nitrate should be avoided to be used for encapsulation with ALD process as the moisture control cannot be achieved by increasing the reaction temperature.

For the ALD and MLD process, more fluidization test is recommended to optimize the reaction temperature as well as determine the minimum fluidization velocity to a more accurate value. Higher reaction temperature and larger number of cycles are recommended to get a denser and thicker Al_2O_3 coating. For the salts which has the trend of deliquescence, precursor of ozone is suggested to be used instead of water.

For the characterization of the coating, cross-sectional transmission electron microscopy (TEM) is highly recommended to be performed since the observing of layered structure was not successful with SEM. However, attention should be paid in selecting the resin to be used to embed the particles, which need to be stable enough under the high resolution electron beam in TEM. Also, reactions between the resin and the coated particles should be avoided, since cerium nitrate reacted with the resin when preparing the cross-sectional sample in this project. The reason why the peaks of Al-O bond of the encapsulated inhibitors after ALD process did not appear in the FTIR spectrum should be figured out. Kinetic leaching test is also recommended for all the encapsulated inhibitors especially for the case of 2-MBT with organic coating to investigate if there is a delayed release in different pH of solution. More groups of ALD process with larger number of cycles combined with leaching tests are recommended to be carried out to optimize the aimed thickness of the coating with which non-leaching can be achieved in neutral solution.

For the characterization of anticorrosion test, epoxy formulation to be used could be optimized corresponding to different kind of shells and bulk inhibitors to avoid the reducing of adhesion. Impedance after a longer immersion time could also be tested to see if there is a long-term healing effect or not. Scanning vibrating electrode technique (SVET) would be recommended to be performed to map and quantify the local electrochemical and corrosion processes as a function of time, with which local anodic and cathodic activities can be monitored to further monitor the healing effect.

Appendix A

ALD and MLD process

A-1 Appendix I: Mass spectrum in MLD process

To make sure that 2 minutes dosing of malonyl chloride and 1,2 butanediol was not wasting too much precursors. Mass spectrum was performed to monitor that ions in the FBR to find the saturation point in the reaction. Figure A-1 shows the mass spectrum results with 20 cycles' of MLD process performed on 2-MBT. It can be seen from the spectrum that in the first half cycle, reaction with malonyl chloride can be monitored by the ion current of Cl^- , but there was no sign of the second half cycle in which butanediol was reacting with powder in the FBR. Figure A-1 shows the ion current of Cl^- , water and N_2 in one of the first half cycle, in which malonyl chloride was dosed into the FBR. It can be seen that the ion current first increased as the dosing of malonyl chloride. After about 1 minutes' dosing, the ion current of Cl^- reached a saturation, in which a plateau was formed. Therefore, the minimum dosing time for malonyl chloride should be more than 1 minute, thus 2 minutes' dosing should be a reasonable condition.

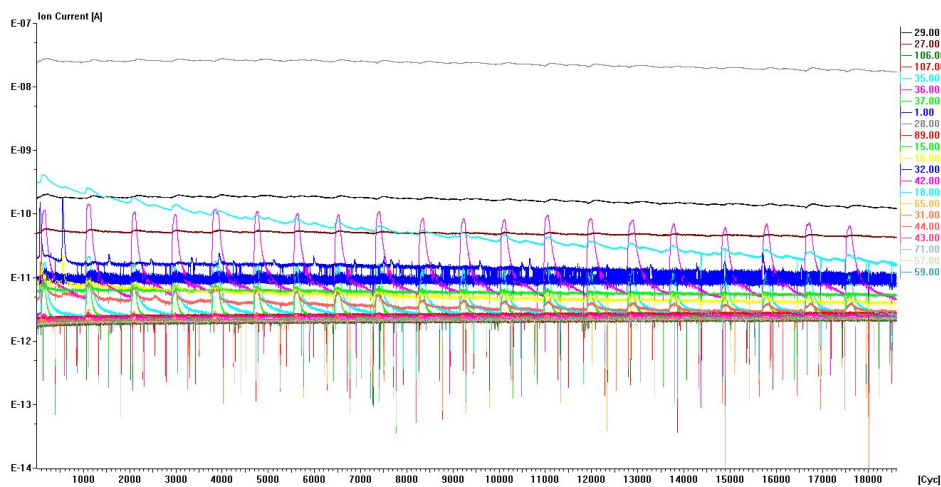


Figure A-1: Mass spectrum during 20 cycles' MLD process on 2-MBT.

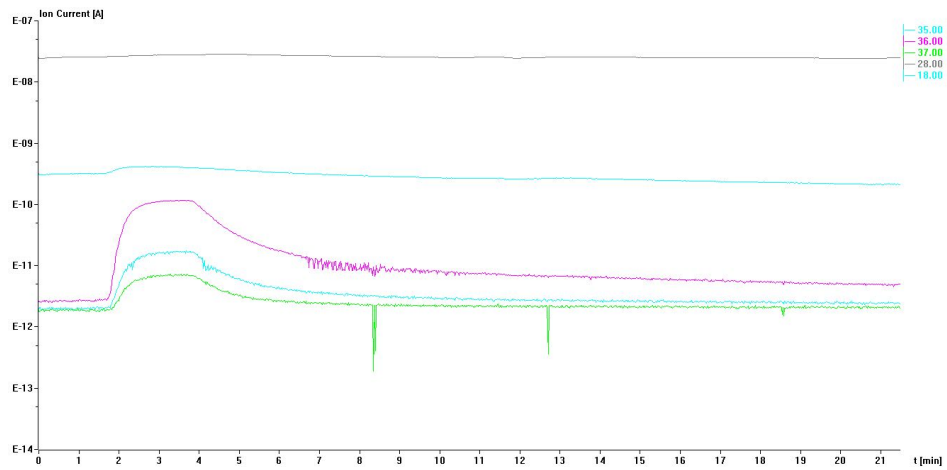


Figure A-2: Mass spectrum of one of the half cycle during 20 cycles' MLD process on 2-MBT.

A-2 Appendix II: Results of fluidization test

compound	fluidizing	drying	mass (g)	vibration (Hz)	reactor temperature (°C)	N ₂ flow rate (m ³ /s)	bed expansion (Δh/h ₀)	mode of fluidization	remark
2-MBT	X	X	10	33	RT	<0.031	no expansion	no fluidization	
2-MBT	X	X	10	33	RT	0.031	0.6	channeling	
2-MBT	X	X	10	33	80	0.025	0.32	no expansion	
2-MBT	X	X	10	33	100	0.025	0.24	no expansion	
2-MBT	X		10	32	80	0.019	0.24	no expansion	
2-MBT	X		10	32	80	0.025	0.4	no expansion	
2-MBT	X		10	32	80	0.031	0.44	no expansion	
2-MBT	X		10	32	100	0.019	0.24	no expansion	
2-MBT	X		10	32	100	0.025	0.4	no expansion	
2-MBT	X		10	32	100	0.031	0.48	no expansion	
2-MBT	X		10	32	120	/	/	no expansion	powder turns brown, sticks to the walls
2-MBT	V		10	32	50	0.025	0.2	no expansion	
2-MBT	V		10	32	50	0.031	0.32	no expansion	
2-MBT	V		10	32	80	0.019	0.32	no expansion	
2-MBT	V		10	32	80	0.025	0.44	no expansion	
2-MBT	V		10	32	100	0.019	0.24	no expansion	
2-MBT	V		10	32	100	0.025	0.32	no expansion	
2-MBT	V		5	50	100	0.019	0	no fluidization	needle shaped crystal formed in the wall
2-MBT	V		5	50	100	0.019	approximately 0.5	no fluidization	some of the powder turn brown
2-MBT	V		5	50	80	0.019	approximately 0.5	no fluidization	fluidization becomes turbulent
2-MBT	V		5	50	80	0.019	0.19	no expansion	
Ce (NO ₃) ₃	V	X	8	50	50	0.031	no expansion	agitation	
Ce (NO ₃) ₃	V	X	8	50	50	0.110	no expansion	splashing	
Ce (NO ₃) ₃	V	X	5	50	50	0.019	slight expansion	agitation	
Ce (NO ₃) ₃	V	FBR, purging N ₂ for 0.5h	5	50	50	0.019	slight expansion	agitation	become turbulent after purging for a longer time
Li ₂ CO ₃	V	X	5	50	120	0.019	slight expansion	channeling	
Li ₂ CO ₃	V	X	5	50	120	0.013	slight expansion	channeling	after dosing TMA, fluid bed expand dramatically. Δh/h ₀ was about 1.

Figure A-3: Results of fluidization test.

Appendix B

Database of EDS and ICP-OES

B-1 Appendix III: EDS data

EDS data for blank lithium carbonate

Table B-1 shows the results of EDS analysis on blank lithium carbonate. The peak of carbon was not cut off because the sample was not coated with carbon via sputtering in this case. The measured point are indicated in Figure B-1

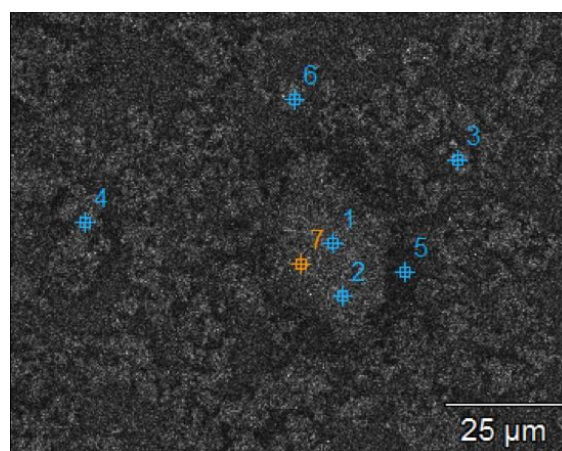


Figure B-1: Image with measurement points indicated on blank lithium carbonate.

Table B-1: EDS elemental concentration measurements results of blank lithium carbonate.

Point	C atom%	O atom%
1	11.72	1.07
2	10.52	3.74
3	15.15	1.12
4	12.11	2.98
5	31.19	68.81
6	8.93	91.07
7	11.92	88.08

EDS data for lithium carbonate with ALD coating

Table B-2 and Table B-3 shows the results of EDS analysis on ALD10 lithium carbonate. The peak of carbon was not cut off in Table B-2 because the sample was not coated with carbon via sputtering in this case, while peak of carbon was cut off in the data from Table B-3. The measured point are indicated in Figure B-2 and Figure B-3 respectively.

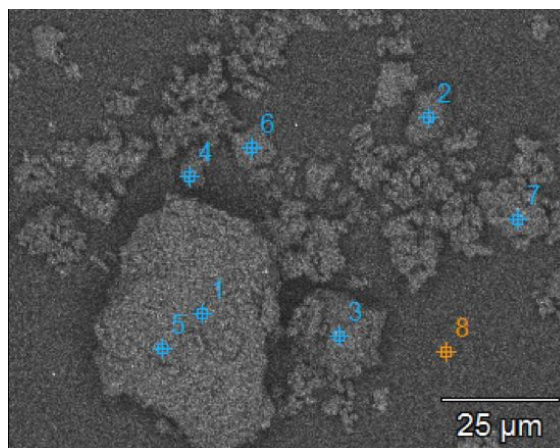
**Figure B-2:** Image with measurement points indicated on ALD 10 lithium carbonate.

Table B-2: EDS elemental concentration measurements results of lithium carbonate after 10 cycles' ALD correspond to the points in Figure B-2.

Point	C atom%	O atom%	Na atom%	Al atom%
1	28.31	69.09		2.59
2	11.71	87.65		0.65
3	9.21	88.59		2.20
4	9.26	90.01		0.73
5	10.89	87.09		2.02
6	16.39	80.91		2.70
7	14.57	78.35		7.08
8	79.10	19.88	1.02	

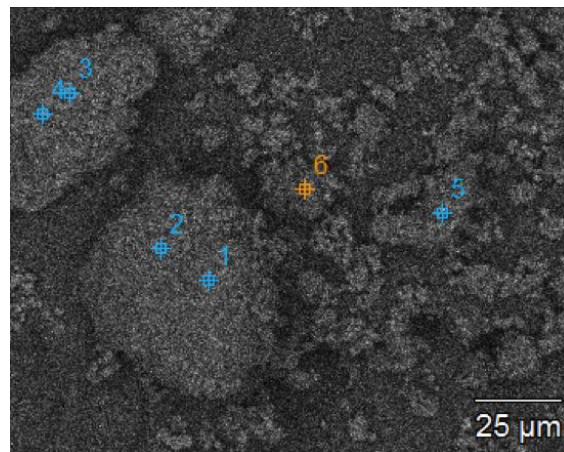


Figure B-3: Image with measurement points indicated on ALD 10 lithium carbonate.

Table B-3: EDS elemental concentration measurements results of lithium carbonate after 10 cycles' ALD correspond to the points in Figure B-3

Point	O atom%	Al atom%
1	97.21	2.79
2	97.98	2.02
3	95.84	4.16
4	96.83	3.17
5	97.53	2.47
6	99.13	0.87

EDS data for cerium nitrate with MLD coating

Table B-4, Table B-5 and Table B-6 show the results of EDS analysis on MLD20 cerium nitrate. The peak of carbon was cut off because all the samples were coated with carbon via sputtering to reduce charging. The measured points are indicated in Figure B-4, Figure B-5 and Figure B-6 respectively.

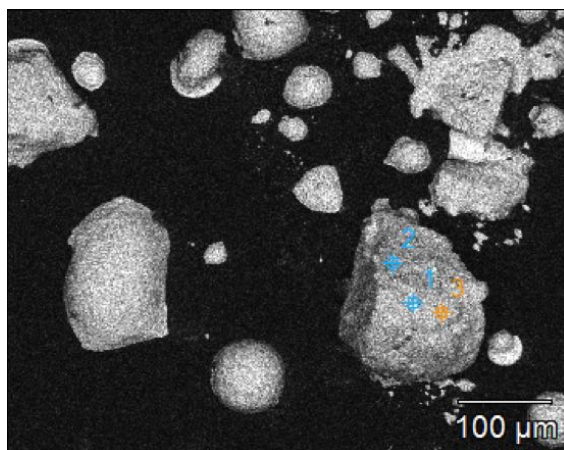


Figure B-4: Image with measurement points indicated on MLD 20 cerium nitrate.

Table B-4: EDS elemental concentration measurements results of cerium nitrate after 20 cycles' MLD correspond to the points in Figure B-4

Point	N atom%	O atom%	Ce atom%
1	35.17	55.35	9.48
2	27.86	66.01	6.13
3	26.86	59.93	13.21

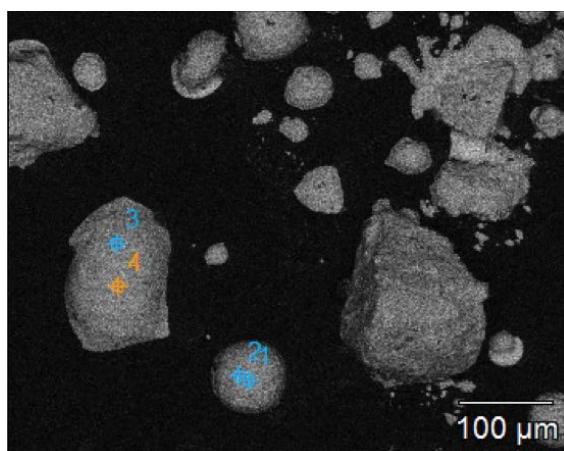


Figure B-5: Image with measurement points indicated on MLD 20 cerium nitrate.

Table B-5: EDS elemental concentration measurements results of cerium nitrate after 20 cycles' MLD correspond to the points in Figure B-5

Point	N atom%	O atom%	Ce atom%
1	29.73	58.86	11.4
2	34.28	58.00	7.72
3	32.79	61.24	5.96
4	37.91	52.53	9.56

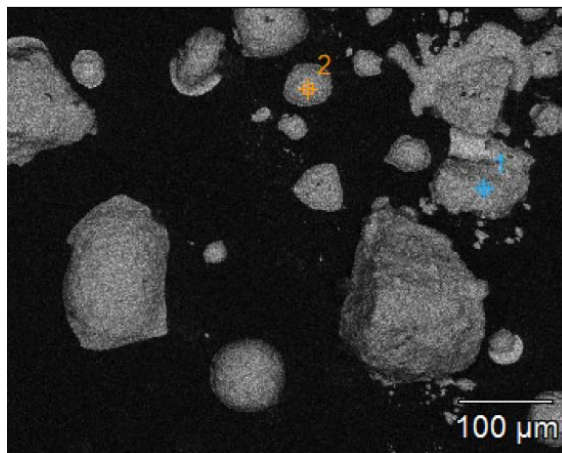


Figure B-6: Image with measurement points indicated on MLD 20 cerium nitrate.

Table B-6: EDS elemental concentration measurements results of cerium nitrate after 20 cycles' MLD correspond to the points in Figure B-6

Point	N atom%	O atom%	Ce atom%
1	35.84	50.42	13.74
2	36.17	55.41	8.43

EDS data for cerium nitrate with ALD coating

Table B-7 and Table B-8 show the results of EDS analysis on ALD10 cerium nitrate. The peak of carbon was cut off in Table B-7, while not in Table B-8. The points measured are indicated in Figure B-7 and Figure B-8 respectively.

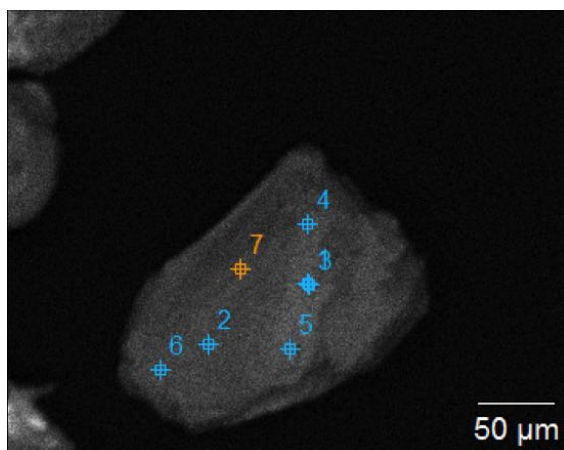


Figure B-7: Image with measurement points indicated on ALD 10 cerium nitrate.

Table B-7: EDS elemental concentration measurements results of cerium nitrate after 10 cycles' ALD correspond to the points in Figure B-7

Point	C atom%	N atom%	O atom%	Al atom%	Ce atom%
1		14.48	82.53		2.99
2			88.64	0.51	10.84
3		13.91	81.48	0.40	4.21
4		15.10	77.68		7.22
5	3.41	15.46	79.72		1.41
6		15.14	75.30	0.93	8.63
7		15.22	77.65		7.14

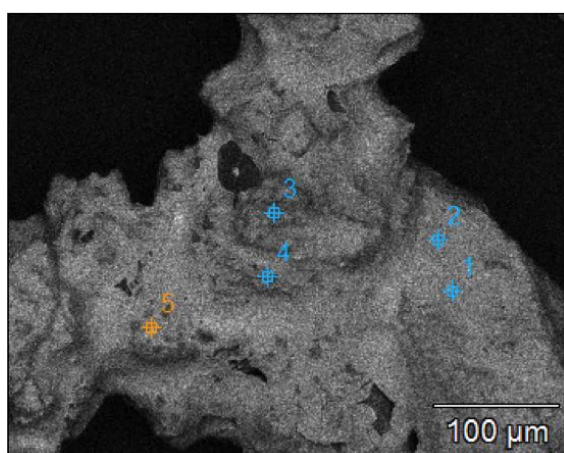


Figure B-8: Image with measurement points indicated on ALD 10 cerium nitrate.

Table B-8: EDS elemental concentration measurements results of cerium nitrate after 10 cycles' ALD correspond to the points in Figure B-8

Point	O atom%	Al atom%	Ce atom%
1	83.89	3.79	12.32
2	86.67	1.02	12.31
3	71.92	20.93	7.16
4	40.48	23.51	36.01
5	85.92		14.08

EDS data for blank 2-MBT without coating

Table B-9 show the results of EDS analysis on blank 2-MBT sample without coating. The peak of carbon was not cut off in this case. The points measured are indicated in Figure B-9.

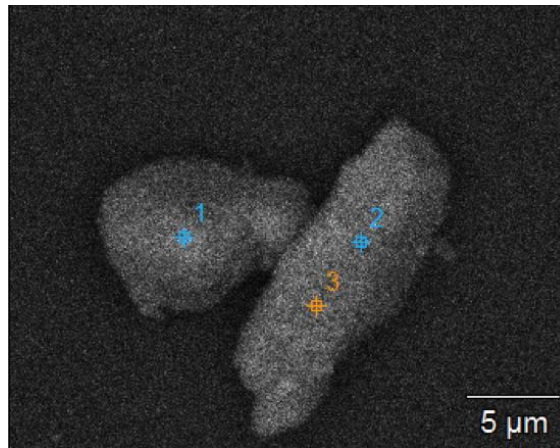


Figure B-9: Image with measurement points indicated on blank 2-MBT without coating.

Table B-9: EDS elemental concentration measurements results of blank 2-MBT correspond to the points in Figure B-9

Point	C atom%	N atom%
1	56.46	43.53
2	30.60	69.40
3	31.31	68.69

EDS data for 2-MBT with MLD coating

Table B-10 and Table B-11 show the results of EDS analysis on 2-MBT MLD20 sample. The peak of carbon was cut off in this case. The points measured are indicated in Figure B-10 and Figure B-11 respectively.

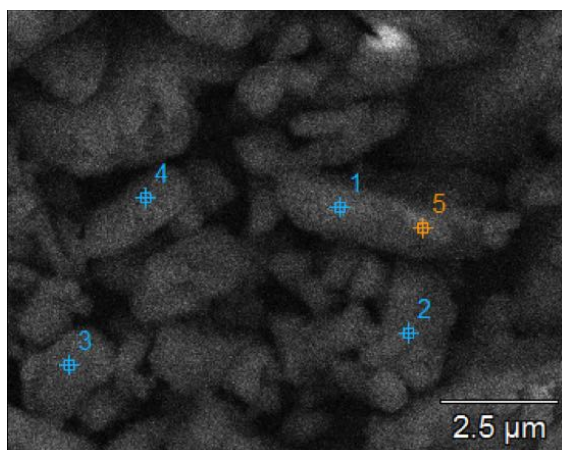


Figure B-10: Image with measurement points indicated on MLD 20 2-MBT.

Table B-10: EDS elemental concentration measurements results of 2-MBT after 20 cycles' MLD correspond to the points in Figure B-10

Point	N atom%	O atom%	S atom%
1	56.23	7.55	36.22
2	56.09	7.24	36.67
3		9.37	90.63
4		10.34	89.66
5		3.61	96.39

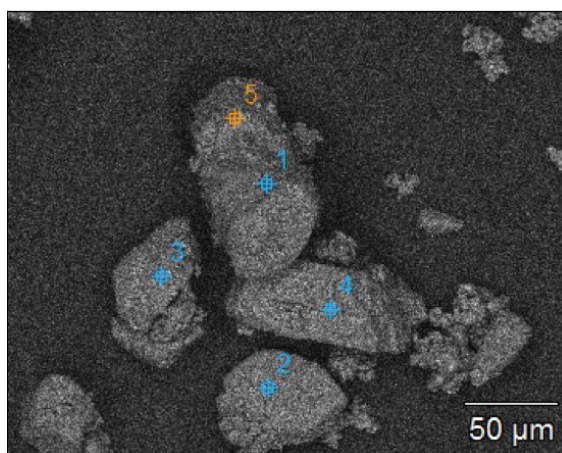


Figure B-11: Image with measurement points indicated on MLD 20 2-MBT.

Table B-11: EDS elemental concentration measurements results of 2-MBT after 20 cycles' MLD correspond to the points in Figure B-11

Point	N atom%	O atom%	S atom%
1	56.27	11.92	31.81
2	46.32	12.52	41.17
3	45.22	13.31	41.47
4		24.71	75.29
5	48.64	11.07	40.29

B-2 Appendix IV: ICP-OES results

Table B-12 and Table B-13 shows the calculated estimation value of the thickness of coating produce via ALD and MALD process according to the ICP-OES results.

Table B-12: ICP-OES results and calculated thickness of alumina layer on lithium carbonate.

sample	x_{Al} wt%	δ (nm)
ALD4	0.28	20
ALD7	0.52	36.7
ALD10	0.62	44.3
MALD4	0.16	11.7
MALD7	0.33	23.1
MALD10	0.57	40.5

Table B-13: ICP-OES results and calculated thickness of alumina layer on cerium nitrate.

sample	x_{Al} wt%	δ (nm)
ALD4	0.79	392
ALD7	1.285	643
ALD10	2.07	1043
MALD4	1.07	543
MALD7	1.325	663.5
MALD10	2.40	1210
Blank	0.14	69.9

Bibliography

- [1] M. Zheludkevich, R. Serra, M. Montemor, K. Yasakau, I. M. Salvado, and M. Ferreira, “Nanostructured sol–gel coatings doped with cerium nitrate as pre-treatments for aa2024-t3: corrosion protection performance,” *Electrochimica Acta*, vol. 51, no. 2, pp. 208–217, 2005.
- [2] G. Decher, J. Hong, and J. Schmitt, “Buildup of ultrathin multilayer films by a self-assembly process: Iii. consecutively alternating adsorption of anionic and cationic polyelectrolytes on charged surfaces,” *Thin solid films*, vol. 210, pp. 831–835, 1992.
- [3] D. G. Shchukin and H. Möhwald, “Surface-engineered nanocontainers for entrapment of corrosion inhibitors,” *Advanced Functional Materials*, vol. 17, no. 9, pp. 1451–1458, 2007.
- [4] D. G. Shchukin, M. Zheludkevich, K. Yasakau, S. Lamaka, M. G. Ferreira, and H. Möhwald, “Layer-by-layer assembled nanocontainers for self-healing corrosion protection,” *Advanced Materials*, vol. 18, no. 13, pp. 1672–1678, 2006.
- [5] R. L. Puurunen, “Surface chemistry of atomic layer deposition: A case study for the trimethylaluminum/water process,” *Journal of applied physics*, vol. 97, no. 12, p. 121301, 2005.
- [6] T. Yoshimura, S. Tatsuura, and W. Sotoyama, “Polymer films formed with monolayer growth steps by molecular layer deposition,” *Applied physics letters*, vol. 59, no. 4, pp. 482–484, 1991.
- [7] J. R. Wank, S. M. George, and A. W. Weimer, “Vibro-fluidization of fine boron nitride powder at low pressure,” *Powder Technology*, vol. 121, no. 2, pp. 195–204, 2001.
- [8] D. Valdesueiro, G. M. Meesters, M. T. Kreutzer, and J. R. van Ommen, “Gas-phase deposition of ultrathin aluminium oxide films on nanoparticles at ambient conditions,” *Materials*, vol. 8, no. 3, pp. 1249–1263, 2015.
- [9] M. Groner, F. Fabreguette, J. Elam, and S. George, “Low-temperature al₂o₃ atomic layer deposition,” *Chemistry of Materials*, vol. 16, no. 4, pp. 639–645, 2004.

- [10] S. A. Vasudevan, Y. Xu, S. Karwal, H. G. van Ostaay, G. M. Meesters, M. Talebi, E. J. Sudhölter, and J. R. van Ommen, "Controlled release from protein particles encapsulated by molecular layer deposition," *Chemical Communications*, vol. 51, no. 63, pp. 12540–12543, 2015.
- [11] S. M. George, B. Yoon, and A. A. Dameron, "Surface chemistry for molecular layer deposition of organic and hybrid organic-inorganic polymers," *Accounts of chemical research*, vol. 42, no. 4, pp. 498–508, 2009.
- [12] D. A. Jones, *Principles and prevention of corrosion*. Macmillan, 1992.
- [13] S. Garcia, H. Fischer, and S. van Der Zwaag, "A critical appraisal of the potential of self healing polymeric coatings," *Progress in Organic Coatings*, vol. 72, no. 3, pp. 211–221, 2011.
- [14] A. Hughes, A. Boag, A. Glenn, D. McCulloch, T. Muster, C. Ryan, C. Luo, X. Zhou, and G. Thompson, "Corrosion of aa2024-t3 part ii: Co-operative corrosion," *Corrosion Science*, vol. 53, no. 1, pp. 27–39, 2011.
- [15] M. Zheludkevich, K. Yasakau, S. Poznyak, and M. Ferreira, "Triazole and thiazole derivatives as corrosion inhibitors for aa2024 aluminium alloy," *Corrosion Science*, vol. 47, no. 12, pp. 3368–3383, 2005.
- [16] A. Khramov, N. Voevodin, V. Balbyshev, and M. Donley, "Hybrid organo-ceramic corrosion protection coatings with encapsulated organic corrosion inhibitors," *Thin solid films*, vol. 447, pp. 549–557, 2004.
- [17] A. C. Balaskas, M. Curioni, and G. E. Thompson, "Effectiveness of 2-mercaptobenzothiazole, 8-hydroxyquinoline and benzotriazole as corrosion inhibitors on aa 2024-t3 assessed by electrochemical methods," *Surface and Interface Analysis*, vol. 47, no. 11, pp. 1029–1039, 2015.
- [18] A. K. Rai, R. Singh, K. Singh, and V. Singh, "Ftir, raman spectra and ab initio calculations of 2-mercaptobenzothiazole," *Spectrochimica Acta Part A: Molecular and Biomolecular Spectroscopy*, vol. 63, no. 2, pp. 483–490, 2006.
- [19] D. Chadwick and T. Hashemi, "Electron spectroscopy of corrosion inhibitors: surface films formed by 2-mercaptobenzothiazole and 2-mercaptobenzimidazole on copper," *Surface Science*, vol. 89, no. 1, pp. 649–659, 1979.
- [20] B. Trachli, M. Keddami, H. Takenouti, and A. Srhiri, "Protective effect of electropolymerized 2-mercaptobenzimidazole upon copper corrosion," *Progress in organic coatings*, vol. 44, no. 1, pp. 17–23, 2002.
- [21] V. Palanivel, Y. Huang, and W. J. van Ooij, "Effects of addition of corrosion inhibitors to silane films on the performance of aa2024-t3 in a 0.5 m nacl solution," *Progress in Organic Coatings*, vol. 53, no. 2, pp. 153–168, 2005.
- [22] K. A. Yasakau, M. L. Zheludkevich, S. V. Lamaka, and M. G. Ferreira, "Mechanism of corrosion inhibition of aa2024 by rare-earth compounds," *The Journal of Physical Chemistry B*, vol. 110, no. 11, pp. 5515–5528, 2006.

- [23] M. Machkova, E. Matter, S. Kozhukharov, and V. Kozhukharov, "Effect of the anionic part of various ce (iii) salts on the corrosion inhibition efficiency of aa2024 aluminium alloy," *Corrosion Science*, vol. 69, pp. 396–405, 2013.
- [24] P. Visser, Y. Liu, H. Terryn, and J. Mol, "Lithium salts as leachable corrosion inhibitors and potential replacement for hexavalent chromium in organic coatings for the protection of aluminum alloys," *Journal of Coatings Technology and Research*, pp. 1–10, 2016.
- [25] R. G. Buchheit, M. Bode, and G. Stoner, "Corrosion-resistant, chromate-free talc coatings for aluminum," *Corrosion*, vol. 50, no. 3, pp. 205–214, 1994.
- [26] Y. Liu, P. Visser, X. Zhou, S. B. Lyon, T. Hashimoto, M. Curioni, A. Gholinia, G. E. Thompson, G. Smyth, S. R. Gibbon, *et al.*, "Protective film formation on aa2024-t3 aluminum alloy by leaching of lithium carbonate from an organic coating," *Journal of The Electrochemical Society*, vol. 163, no. 3, pp. C45–C53, 2016.
- [27] P. Visser and S. A. Hayes, "Anti-corrosive coating composition," Jan. 14 2014. US Patent 8,628,689.
- [28] P. Visser, Y. Liu, X. Zhou, T. Hashimoto, G. E. Thompson, S. B. Lyon, L. G. van der Ven, A. J. Mol, and H. A. Terryn, "The corrosion protection of aa2024-t3 aluminium alloy by leaching of lithium-containing salts from organic coatings," *Faraday discussions*, vol. 180, pp. 511–526, 2015.
- [29] R. Trask, H. Williams, and I. Bond, "Self-healing polymer composites: mimicking nature to enhance performance," *Bioinspiration & Biomimetics*, vol. 2, no. 1, p. P1, 2007.
- [30] M. AbdolahZadeh, S. van der Zwaag, and S. Garcia, "Self-healing corrosion-protective sol-gel coatings based on extrinsic and intrinsic healing approaches," 2016.
- [31] M. Jakab and J. Scully, "On-demand release of corrosion-inhibiting ions from amorphous al-co-ce alloys," *Nature materials*, vol. 4, no. 9, pp. 667–670, 2005.
- [32] M. Jakab, F. Presuel-Moreno, and J. Scully, "Critical concentrations associated with cobalt, cerium, and molybdenum inhibition of aa2024-t3 corrosion: delivery from al-co-ce (-mo) alloys," *Corrosion*, vol. 61, no. 3, pp. 246–263, 2005.
- [33] M. Kendig and P. Kinlen, "Demonstration of galvanically stimulated release of a corrosion inhibitor basis for smart corrosion inhibiting materials," *Journal of the Electrochemical Society*, vol. 154, no. 4, pp. C195–C201, 2007.
- [34] L. Mascia, L. Prezzi, G. D. Wilcox, and M. Lavorgna, "Molybdate doping of networks in epoxy-silica hybrids: Domain structuring and corrosion inhibition," *Progress in organic coatings*, vol. 56, no. 1, pp. 13–22, 2006.
- [35] M. Garcia-Heras, A. Jimenez-Morales, B. Casal, J. Galvan, S. Radzki, and M. Villegas, "Preparation and electrochemical study of cerium-silica sol-gel thin films," *Journal of Alloys and Compounds*, vol. 380, no. 1, pp. 219–224, 2004.
- [36] D. G. Shchukin, M. Zheludkevich, and H. Möhwald, "Feedback active coatings based on incorporated nanocontainers," *Journal of Materials Chemistry*, vol. 16, no. 47, pp. 4561–4566, 2006.

- [37] D. G. Shchukin and H. Möhwald, "Self-repairing coatings containing active nanoreservoirs," *small*, vol. 3, no. 6, pp. 926–943, 2007.
- [38] A. Khramov, N. Voevodin, V. Balbyshev, and R. Mantz, "Sol-gel-derived corrosion-protective coatings with controllable release of incorporated organic corrosion inhibitors," *Thin Solid Films*, vol. 483, no. 1, pp. 191–196, 2005.
- [39] M. V. Rekharsky and Y. Inoue, "Complexation thermodynamics of cyclodextrins," *Chemical reviews*, vol. 98, no. 5, pp. 1875–1918, 1998.
- [40] C. Schmidt, "Anti-corrosive coating including a filler with a hollow cellular structure," May 7 2002. US Patent 6,383,271.
- [41] D. A. Pippard, "Corrosion inhibitors, method of producing them and protective coatings containing them," Sept. 20 1983. US Patent 4,405,493.
- [42] R. Buchheit, S. Mamidipally, P. Schmutz, and H. Guan, "Active corrosion protection in ce-modified hydrotalcite conversion coatings," *Corrosion*, vol. 58, no. 1, pp. 3–14, 2002.
- [43] H. Yang and W. J. van Ooij, "Plasma-treated triazole as a novel organic slow-release paint pigment for corrosion control of aa2024-t3," *Progress in organic coatings*, vol. 50, no. 3, pp. 149–161, 2004.
- [44] A. Kumar, L. Stephenson, and J. Murray, "Self-healing coatings for steel," *Progress in Organic Coatings*, vol. 55, no. 3, pp. 244–253, 2006.
- [45] D. S. Kommireddy, S. M. Sriram, Y. M. Lvov, and D. K. Mills, "Stem cell attachment to layer-by-layer assembled tio 2 nanoparticle thin films," *Biomaterials*, vol. 27, no. 24, pp. 4296–4303, 2006.
- [46] D. G. Shchukin, S. Lamaka, K. Yasakau, M. Zheludkevich, M. Ferreira, and H. Möhwald, "Active anticorrosion coatings with halloysite nanocontainers," *The Journal of Physical Chemistry C*, vol. 112, no. 4, pp. 958–964, 2008.
- [47] S. M. George, "Atomic layer deposition: an overview," *Chemical reviews*, vol. 110, no. 1, pp. 111–131, 2009.
- [48] D. Longrie, D. Deduytsche, and C. Detavernier, "Reactor concepts for atomic layer deposition on agitated particles: A review," *Journal of Vacuum Science & Technology A*, vol. 32, no. 1, p. 010802, 2014.
- [49] A. Goulas and J. R. van Ommen, "Scalable production of nanostructured particles using atomic layer deposition," *KONA Powder and Particle Journal*, vol. 31, no. 0, pp. 234–246, 2014.
- [50] P. Garcia-Trinanes, D. Valdesueiro, J. Seville, G. Meesters, M. Kreutzer, J. van Ommen, and J. Gargiuli, "Enhancing the activation of silicon carbide particles with gas-phase coating of aluminum oxide,"
- [51] S. Sarkar, J. H. Culp, J. T. Whyland, M. Garvan, and V. Misra, "Encapsulation of organic solar cells with ultrathin barrier layers deposited by ozone-based atomic layer deposition," *Organic Electronics*, vol. 11, no. 12, pp. 1896–1900, 2010.

- [52] A. A. Dameron, D. Seghete, B. Burton, S. Davidson, A. Cavanagh, J. Bertrand, and S. George, "Molecular layer deposition of alucone polymer films using trimethylaluminum and ethylene glycol," *Chemistry of Materials*, vol. 20, no. 10, pp. 3315–3326, 2008.
- [53] M. Serdechnova, V. L. Ivanov, M. R. M. Domingues, D. V. Evtuguin, M. G. Ferreira, and M. L. Zheludkevich, "Photodegradation of 2-mercaptobenzothiazole and 1, 2, 3-benzotriazole corrosion inhibitors in aqueous solutions and organic solvents," *Physical Chemistry Chemical Physics*, vol. 16, no. 45, pp. 25152–25160, 2014.
- [54] M. J. Rhodes, *Introduction to particle technology*. John Wiley & Sons, 2008.
- [55] D. N. Goldstein, J. A. McCormick, and S. M. George, "Al₂O₃ atomic layer deposition with trimethylaluminum and ozone studied by in situ transmission ftir spectroscopy and quadrupole mass spectrometry," *The Journal of Physical Chemistry C*, vol. 112, no. 49, pp. 19530–19539, 2008.
- [56] G. Dorsey, "The characterization of anodic aluminas i. composition of films from acidic anodizing electrolytes," *Journal of The Electrochemical Society*, vol. 113, no. 2, pp. 169–172, 1966.
- [57] G. V. Zhuang, G. Chen, J. Shim, X. Song, P. N. Ross, and T. J. Richardson, "Li₂Co₃ in lini 0.8 co 0.15 al 0.05 o 2 cathodes and its effects on capacity and power," *Journal of power sources*, vol. 134, no. 2, pp. 293–297, 2004.
- [58] M. Omar and A. H. Ahmad, "Electrical impedance spectroscopy and fourier transform infrared studies of new binary li₂co₃-lii solid electrolyte," in *Materials Science Forum*, vol. 846, pp. 517–522, Trans Tech Publ, 2016.
- [59] Y. Hamlaoui, F. Pedraza, C. Remazeilles, S. Cohendoz, C. Rébéré, L. Tifouti, and J. Creus, "Cathodic electrodeposition of cerium-based oxides on carbon steel from concentrated cerium nitrate solutions: Part i. electrochemical and analytical characterisation," *Materials Chemistry and Physics*, vol. 113, no. 2, pp. 650–657, 2009.
- [60] J. Carneiro, J. Tedim, S. Fernandes, C. Freire, A. Silvestre, A. Gandini, M. Ferreira, and M. Zheludkevich, "Chitosan-based self-healing protective coatings doped with cerium nitrate for corrosion protection of aluminum alloy 2024," *Progress in Organic Coatings*, vol. 75, no. 1, pp. 8–13, 2012.
- [61] H. Böhlig, M. Ackermann, F. Billes, and M. Kudra, "Vibrational analysis of benzothiazoline-2-thione," *Spectrochimica Acta Part A: Molecular and Biomolecular Spectroscopy*, vol. 55, no. 13, pp. 2635–2646, 1999.
- [62] J. Fen, W.-q. Qin, R.-z. Liu, and X.-j. Wang, "Adsorption mechanism of 2-mercaptobenzothiazole on chalcopyrite and sphalerite surfaces: Ab initio and spectroscopy studies," *Transactions of Nonferrous Metals Society of China*, vol. 25, no. 7, pp. 2388–2397, 2015.
- [63] C. Hansson and G. Agrup, "Stability of the mercaptobenzothiazole compounds," *Contact Dermatitis*, vol. 28, no. 1, pp. 29–34, 1993.

Glossary

List of Acronyms

ALD	Atomic Layer Deposition
MLD	Molecular Layer Deposition
TMA	Trimethylaluminium
2-MBT	2-mercaptobenzothiazole
SVET	Scanning Vibrating Electrode Technique
EIS	Electrochemical Impedance Spectroscopy
FBR	Fluidized Bed Reactor
SEM	Scanning Electron Microscope
TEM	transmission electron microscopy
EDS	Energy-Dispersive X-ray Spectroscopy
FTIR	Fourier Transform Infrared Spectroscopy
ATR	Attenuated Total Reflection
ICP-OES	Inductively Coupled Plasma-Optical Emission Spectroscopy
GPC	Growth Per Cycle
TGA	Thermogravimetric Analysis
UV-vis	Ultraviolet-Visible spectroscopy

